Faculty of Physics and Astronomy
University of Heidelberg

Diploma thesis
in Physics

submitted by
Andre Niklas Wenz
born in Stuttgart
2008

Few-Body Physics in a Three-Component Fermi Gas

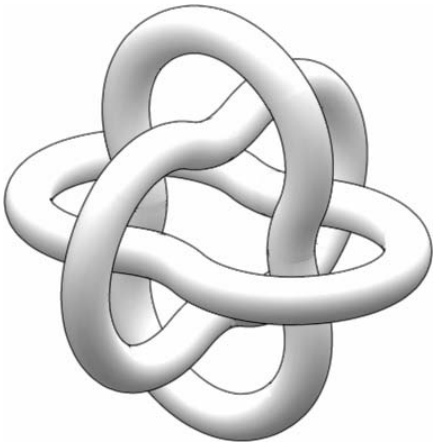

This diploma thesis has been carried out by

Andre Niklas Wenz at the

Max-Planck-Institute for Nuclear Physics

under the supervision of

Juniorprofessor Dr. Selim Jochim

Abstract:
This thesis reports on the first production of a degenerate three-component Fermi gas in equilibrium. The sample consists of ^{6}Li atoms in the three lowest Zeeman sublevels. Its production is enabled through the control of interactions by means of Feshbach resonances. For weak interactions the three-state mixture exhibits a remarkable stability with lifetimes exceeding 30 seconds. This represents an excellent starting point for future experiments.

In the course of this thesis, we analyzed the collisional stability of such a three-component sample as a function of the magnetic field and thus also as a function of the interaction strength. In the region below 600 Gauss we observed a strongly varying three-body loss and found two loss resonances at about 127 Gauss and at 500 Gauss. The observed three-body loss coefficient varies over almost three orders of magnitude. We were able to explain this behavior with a model utilizing the universality of systems with large scattering lengths. In this model, the loss resonances are due to a universal three-body bound state that crosses the three-atom continuum twice. Additionally, further measurements could be performed in the region of unitary two-body interactions near the Feshbach resonances.

Zusammenfassung:
Diese Arbeit behandelt die erste Realisierung eines entarteten dreikomponentigen Fermigases in einem Gleichgewichtszustand. Das Gas besteht aus ^{6}Li Atomen in den drei niedrigsten Zeemanzuständen. Die Herstellung dieses Gases wird ermöglicht durch die Kontrolle der Wechselwirkung durch Feshbach-Resonanzen. Für schwache Wechselwirkungen weist die dreikomponentige Mischung eine bemerkenswerte Stabilität auf (Lebensdauer >30 Sekunden). Dies stellt eine hervorragende Ausgangssituation für zukünftige Experimente dar.

Im Verlauf dieser Arbeit untersuchten wir die Stabilität gegen Zerfall durch Stöße als Funktion des Magnetfelds und daher ebenso als Funktion der Wechselwirkungsstärke. Für Magnetfelder kleiner als 600 Gauss konnten wir einen stark variierenner Dreikörperverlust und zwei Verlustresonanzen beobachten, eine bei etwa 127 Gauss die andere bei ca. 500 Gauss. Der beobachtete Dreikörperverlustkoeffizient variiert im untersuchten Bereich um nahezu drei Größenordnungen und es war uns möglich diesen Verlauf mit einem Modell zu erklären, welches sich die Universalität von Systemen mit großer Streulänge zunutze macht. In diesem Modell werden die Verlustresonanzen durch einen universellen Trimerzustand hervorgerufen, welcher das Kontinuum zweimal kreuzt. Darüber hinaus konnten im Rahmen dieser dieser Arbeit weitere Messungen im Bereich starker Wechselwirkung nahe den Zweikörper-Feshbach-Resonanzen durchgeführt werden.

Contents

Chapter 1

Introduction

The history of science has always been characterized by classifications and abstraction. Soon after the discovery of a novel, nonclassical spin degree of freedom in electrons and atoms, in the beginning of the 20th century, particles were classified into two distinct categories. The integer spin particles are called bosons, named after the Indian physicist S. Bose who, together with A. Einstein, developed the statistics describing their behavior (Bose-Einstein-statistics). On the other hand, the half-integer spin particles, called fermions, obey the Fermi-Dirac statistics and were named after E. Fermi and P. Dirac. These two particle groups differ fundamentally in their symmetry and behavior. Since bosons have a totally symmetric wavefunction, they can and favor to occupy the same quantum state at the same position. Fermions, on the other hand, cannot be at the same place if they are in the same quantum state, because of their totally antisymmetric wavefunction. This fermionic property is called Pauli exclusion principle and has fundamental influence on our everyday lives since almost all matter is built from fermionic building blocks (e.g. electrons, protons, neutrons).

Especially in the quantum degenerate regime, where the wavefunctions start to overlap, the fundamental differences between fermions and bosons take effect. This regime can be reached by either drastically cooling the system to extremely low temperatures or by dramatically increasing the system's density.

The first theoretical studies on degenerate quantum ensembles reach back to the beginnings of quantum theory. A. Einstein predicted that if bosons would obey the statistic developed by Bose, they would "condense" into the first quantum state (the state without kinetic energy) when the density is increased by an isothermal compression [Ein25]. This macroscopic occupation of the ground state is therefore referred to as Bose-Einstein condensation (BEC). For many years, this region seemed to be unreachable in experiments. But with novel techniques like laser cooling and evaporative cooling, a pure Bose-Einstein condensate could finally be produced by cooling dilute gas vapors to ultracold temperatures [And95, Dav95].

In the years to follow, this new state of matter and its physics turned out to be extremely exciting. Theoretical predictions and ideas that had already been developed decades before could be proven in a series of beautiful experiments. This proves that the diluteness and the controllability make ultracold gases an unique quantum system.

Soon after the first production of Bose-Einstein condensates with ultracold atomic vapors, efforts were made to enter the quantum degenerate regime for fermionic ultracold gases as well. But some obstacles had to be overcome first. In contrast to bosons, identical fermions stop interacting if they are cooled to ultralow temperatures. Thus in order to perform evaporative cooling one has to use a second component (in most cases one simply uses an additional spin state). In constrast to the bosonic case where a BEC is formed even for a noninteracting sample, the fermions need interactions for a phase transition to occur. With an attractive interaction between the two components, they form so-called Cooper pairs. These pairs behave like bosons and "condense" into a superfluid state if the temperature is sufficiently low. This phase transition is well known from solid state physics, where the two-component (spin up and spin down) electron gas in certain metals forms a superfluid for low temperatures. This frictionless flow of electron Cooper-pairs leads to the phenomenon called superconductivity. A similar state can also be observed in liquid ^{3}He.

The occurrence of so-called Feshbach resonances makes the ultracold fermionic gases an excellent system to study these superfluids and their pairing mechanisms. These scattering resonances allow us to tune the only interaction parameter of the system, the s-wave scattering length a, to arbitrary values simply by applying a homogeneous magnetic field. For large positive values of the scattering length, bosonic molecules can be formed which are able to form a BEC of molecules [Joc03b, Gre03, Zwi03b]. If the scattering length is further increased it diverges and changes sign. In this strongly interacting regime, the bosonic molecules can be continuously transformed into Cooper pairs without destroying the superfluidity of the system [Reg04, Bar04, Bou04, Zwi05]. This so-called BEC-BCS crossover is still an experimentally and theoretically investigated system especially because for diverging scattering length the system behaves completely independent of its short range behavior [Car03, Hei01, Ho04]. Thus results obtained from such an ultracold fermionic gas can be used to predict properties of diverse systems like neutron stars or high-T_c-superconductors [Che05].

The addition of a third state to such a tunable fermionic system raises several new questions. This three-component Fermi gas, which cannot be achieved in solid state physics or in liquid ^{3}He, paves the way for new and so far unobserved phenomena. Its SU(3) symmetry, together with the possibility of tuning the interactions by means of Feshbach resonances, offers an intriguing generic system for the study of physics related to high-energy physics and quark matter [Wil07].

There are theoretical predictions that such a system should form a superfluid state comparable to a color superfluid where two components pair to Cooper pairs and the third one remains a spectator [Rap07]. This system should then undergo a quantum phase transition if the interactions are increased and form three-body bound states. This formation of bound states would then be the analogy to the formation of Baryons consiting of three quarks.

Furthermore, this ternary mixture provides fascinating insight into few-body physics and this thesis is a careful scrutiny of these phenomena and their implication for fermionic systems. There are evidences that universal three-body bound states are formed in such a gas [Ott08, Bra08, Nai08, Sch08a]. These states are most likely related to phenomena described and theoretically developed by V. Efimov in the early 1970s [Efi71, Efi70, Efi79]. Thus once again, ultracold gases are used to prove and support theoretical predictions and paradigms developed several years ago.

Outline

This diploma thesis begins with a summary of the relevant properties of ultracold fermionic gases and their interactions in chapter 2. In chapter 3, we apply three-body theory to obtain qualitative insights into the few-body phenomena in a three-component Fermi gas. We then use the universality of systems with large scattering lengths to deduce analytic predictions for the three-body loss in such ternary samples. These relations are able to describe the later performed experiments on the stability of three-component Fermi gases.

After these theoretical considerations, we describe the experimental setup in chapter 4. In this description, we focus on parts of the setup that were added in the course of this thesis, like the radio frequency setup and the high resolution imaging. Chapter 5 deals with the techniques used for the production and analysis of a three-component Fermi gas. Additionally, this chapter contains theoretical predictions for such a three-state mixture and the problems we faced during its production.

Chapter 6 presents the first experiments with three-component Fermi gases and their results. We were able to measure the three-body loss as a function of the interaction strength. The analysis of those experiments is also performed in this chapter and implies that universal effects occur in this system. The last chapter (chapter 7) summarizes all results obtained during this diploma thesis and gives an outlook on future plans and experiments.

Chapter 2

Ultracold Fermi Gases

Since the primary focus of this thesis is on ultracold fermions, the aim of this chapter is to provide a brief introduction on their properties and behavior. To fully understand the production procedure of ultracold Fermi gases and the experiments performed with such a sample, it is necessary to discuss the main properties of their interactions. Since the theory of ultracold Fermi gases has been discussed in detail in several review articles [Gio08, Ket08] and text books [Pit03, Pet02], we will only give a brief overview on the interaction properties of ultracold fermionic gases and then analyze the density and momentum distribution of a degenerate Fermi gas.

2.1 Interactions and Universality

Interactions in an ultracold Fermi gas are essential for the preparation and all possible experiments. Sufficient elastic scattering is the prerequisite for evaporative cooling. On the other hand too strong inelastic collisions lead to fast loss of atoms from the trap and thus prevent the preparation of an ultracold Fermi gas.

One particular feature of ultracold gases is that their interactions can be desribed in a simple model. The s-wave scattering length a is the only parameter that determines all relevant interaction properties. By utilizing so-called Feshbach resonances, this interaction parameter can be tuned to arbitrary values reaching from $-\infty$ to $+\infty$. Thus we are able to access the full range of attractive, repulsive and non-interacting samples by applying a homogeneous magnetic field. As we will see later, we use all those regimes, but especially the regions of very strong interactions (attractive and repulsive) offer interesting phenomena.

2.1.1 Scattering in Ultracold Fermi Gases

Using fundamental quantum mechanics, the scattering process between two atoms can be described by the stationary Schrödinger equation for the relative motion (if relativistic and spin effects are neglected):

$$\left(-\frac{\hbar^2}{2\,m^*}\,\Delta + V(\boldsymbol{r}) - E\right)\,\psi(\boldsymbol{r}) = 0. \tag{2.1}$$

Here, $E > 0$ is the energy, $V(\boldsymbol{r})$ is the interaction potential, $\boldsymbol{r}$ is the atoms' relative coordinate ($\boldsymbol{r}_1 - \boldsymbol{r}_2$) and $m^* = (m_1\,m_2)/(m_1 + m_2)$ is their reduced mass. In a spherically symmetric potential and with the wave number k defined by

$$E = \frac{\hbar^2\,k^2}{2\,m^*}, \tag{2.2}$$

one obtains the following solution for the asymptotic region where $r = |\boldsymbol{r}|$ is significantly larger than the range of the interaction potential:

$$\psi(\boldsymbol{r}) \propto e^{ikz} + f(\theta)\,\frac{e^{ikr}}{r}. \tag{2.3}$$

Here, θ is the angle between the z-axis and $\boldsymbol{r}$. The function $f(\theta)$ is called scattering amplitude. One can show that the scattering amplitude is connected to the differential cross section by ($0 < \theta < \pi$):

$$\frac{d\sigma}{d\Omega} = |f(\theta)|^2\,. \tag{2.4}$$

This result is slightly altered for identical particles, due to the symmetrization and antisymmetrization of the wavefunction for bosons and fermions, respectively:

$$\left(\frac{d\sigma}{d\Omega}\right)_{identical} = |f(\theta) \pm f(\pi - \theta)|^2\,, \tag{2.5}$$

here $0 < \theta < \pi/2$. For identical bosons (fermions) the wavefunction has to be totally symmetric (antisymmetric) and hence one has to consider the $+(-)$ sign.

Scattering length and low-energy limit

The scattering length can be defined as the isotropic low-energy ($E \to 0$) limit of the scattering amplitude:

$$f(\theta) \to -a \quad \text{for E} \to 0. \tag{2.6}$$

Thus for vanishing energy, the cross section becomes isotropic and independent of the energy and reaches a constant value. Taking into account the symmetry of the wavefunction for bosons and fermions, we obtain the following total cross sections in the low-energy limit:

$$\sigma_{id.bosons} = 8\,\pi\,a^2, \tag{2.7}$$
$$\sigma_{nonid.fermions} = 4\,\pi\,a^2, \tag{2.8}$$
$$\sigma_{id.fermions} = 0. \tag{2.9}$$

Partial wave expansion

For the calculation of the scattering amplitude in a rotationally symmetric interaction potential, it is helpful to expand the wavefunction into partial waves (i.e. for different values of the angular momentum l). One can then simplify equation 2.1 and obtains a radial equation for each angular momentum state $\chi_{k,l}$:

$$\left(\frac{d^2}{dr^2} - \frac{2\,m^*}{\hbar^2}\left(V(r) + \frac{\hbar^2 l(l+1)}{2\,m^*\,r^2}\right) + k^2\right)\,\chi_{k,l}(r) = 0. \tag{2.10}$$

One sees that the spherical part of the Laplace operator in 2.1 leads to a centrifugal barrier $E_c = \hbar^2 l(l+1)/(2\,m^*\,r^2)$. For scattering energies tending to 0, this barrier prevents the states with $l > 0$ from scattering. In the case of ^{6}Li $E_c \approx k_B\,7\,mK$ (from [Jul92]) thus for temperatures significantly lower than 7 mK isotropic s-wave scattering is the only possible scattering process.

Furthermore, it can be shown that different partial waves obtain different phase shifts δ_l. Since we examine elastic scattering processes, these phase shifts determine the complete scattering process. For non-identical particles the contribution to the total cross section for each partial wave can be written as:

$$\sigma_l(k) = \frac{4\pi}{k^2}\,(2l+1)\,\sin^2\delta_l. \tag{2.11}$$

The s-wave phase shift δ_0 can be used to define the scattering length in the low-energy limit:

$$a = -\lim_{k\to 0}\frac{\tan\delta_0(k)}{k}. \tag{2.12}$$

Low energy behavior of the cross section

A more careful analysis shows that the low-energy cross section deduced above is only true if $ka \ll 1$. If the scattering length diverges, the given cross section will also diverge. This is unphysical, because the cross section cannot exceed the size of the wave packet, given by the deBroglie wavelength $\lambda_{dB} = 2\pi/k$. For

diverging scattering lengths the interparticle spacing ($\propto 1/k$) is the only relevant length scale of the system and thus the cross section should scale with $1/k^2$ for $a \to \pm\infty$. Assuming a point-like interaction the resulting total cross section for non identical particles can be written as

$$\sigma(k) = \frac{4\pi\, a^2}{1 + k^2\, a^2}. \tag{2.13}$$

This model is a good approximation if the range of the interaction potential is significantly smaller than the scattering length and the deBroglie wavelength, which is true in most of our cases.

This means that for non-diverging scattering lengths one obtains the relation given above ($\sigma = 4\,\pi a^2$ for $ka \ll 1$) in the low-energy limit. However, if the scattering length diverges, the result is the so-called unitary limit $\sigma_u(k) = 4\,\pi/k^2$, which is the maximal possible cross section for a s-wave collision and occurs if $\sin^2\delta_0 = 1$ in equation 2.11.

2.1.2 Hyperfine States of Lithium-6

Before we can examine the interactions in a gas of ^{6}Li, we have to examine its hyperfine states to determine the states participating in scattering events.

Fermionic ^{6}Li has a total nuclear spin of $I = 1$ and a total electron spin of $S = 1/2$. It follows that at low magnetic fields they couple to a total spin of $F = 3/2$ or $1/2$. Hence in the case of zero magnetic field, the electronic ground state splits into a quadruplet ($F = 3/2$) and a doublet ($F = 1/2$) of states (see figure 2.1), which are separated by 228.2 MHz.

For higher magnetic fields ($\gg 30$ Gauss) one enters the Paschen-Back regime. Here, the electron and nuclear spin decouple into two branches due to the two possibilities of the electron spin. The energy of one of them is lowered for higher magnetic fields so that these states are high-field seeking (the other three states are low-field seekers). Each branch consists of three states, due to the nuclear spin triplet. For the sake of simplicity, the states are labeled from $|1\rangle$ to $|6\rangle$ in order of increasing energy in the magnetic field.

In equation 2.8, we see that the cross section for identical fermions vanishes at low energies. Thus one has to use a mixture of at least two states to study an interacting Fermi gas. The states $|1\rangle$ and $|2\rangle$ are well-suited for this purpose, because they are the lowest hyperfine states and thus stable against inelastic spin changing collisions. In the following section we will see that by using a broad Feshbach resonance in ^{6}Li, one is able to tune the scattering length in a $|1\rangle - |2\rangle$ mixture to high values. Thus one can perform very fast and efficient evaporation in an optical dipole trap. Furthermore, this mixture is relatively easy to produce in the transfer from the magneto-optical trap (MOT) into the dipole trap. Since

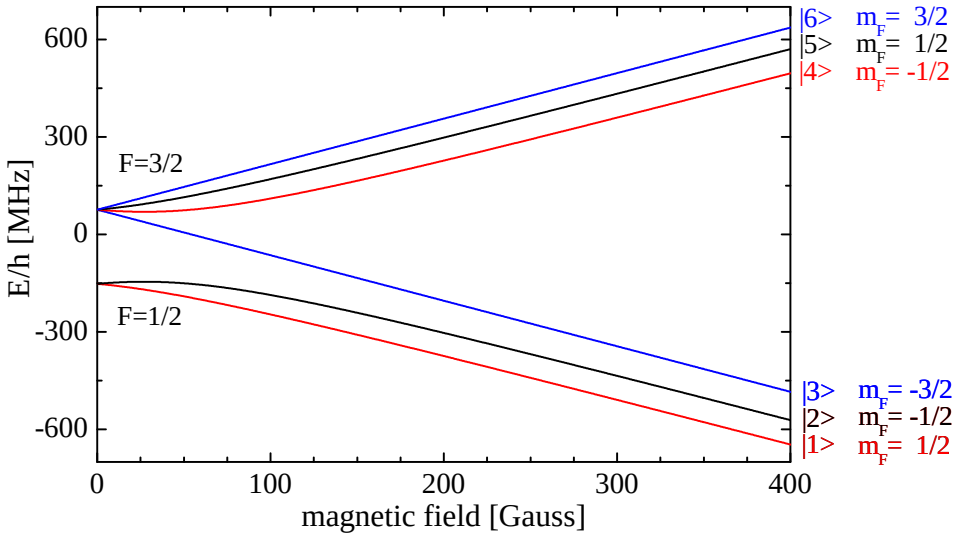

Figure 2.1: Zeeman hyperfine levels of the ^{6}Li electronic ground state.

the cooling transition of ^{6}Li in the MOT goes from the $S_{1/2}(F = 3/2)$ to the $^2P_{3/2}$ states, one has to additionally use a repumper driving the $S_{1/2}(F = 1/2)$ to $^2P_{3/2}$ transition (see [Ser07]). In order to pump the atoms into the $F = 1/2$, the repumper is switched off before the cooler during the transfer to the dipole trap and thus one automatically produces a mixture consisting of atoms in states $|1\rangle$ and $|2\rangle$ (if a homogeneous magnetic field is applied).

The states $|1\rangle$ and $|2\rangle$ are high-field seeking. They are thus not magnetically trappable (as it is not possible to produce local magnetic field maxima in those traps). Hence there is no stable and magnetically trappable two-component mixture of ^{6}Li which means that one has to utilize a bosonic cooling agent (e.g. ^{23}Na or ^{7}Li) if one insists on the use of magnetic traps.

For the reasons given above, we will use an optical dipole trap and hence the "all-optical" approach explained in [Gra02] or [Gri07].

2.1.3 Feshbach Resonances

From low-energy scattering theory, we know that if a bound state of the interaction potential is close to the continuum, the scattering length and the interaction strength are resonantly enhanced. For a bound state situated slightly below the continuum this leads to a large positive scattering length (see for example [Lan81]), which diverges to $+\infty$ if the bound states reaches the continuum. The scattering length then changes sign, becoming negative and large in magnitude, if the bound state is right above the zero-energy threshold.

Since atoms can normally scatter in various spin channels, there are other channels beside the scattering channel, which is also called open channel. As the continuum of the other channels is higher in energy, they appear as closed channels for the scattering states (see figure 2.2). If these channels have a different magnetic moment, they are tunable with respect to each other by applying a homogeneous magnetic field. If one now tunes a bound state of the close channel to the continuum of the open (scattering) channel and if there is a coupling between those channels, the scattering length also becomes resonantly enhanced.

Such scattering resonances between two channels are called Feshbach resonances, named after H. Feshbach who studied this concept in the field of nuclear reactions [Fes58]. These resonances allow to tune the scattering length to arbitrary positive and negative values. In our case, the hyperfine coupling connects the open and closed channel with different magnetic momenta. Thus in a descriptive picture the scattering atoms approach each other and change into the closed channel for a certain time. Then they return to the open channel and separate again. During this second order process, the accumulated phase shift changes so that the scattering length diverges and then changes sign. A more thorough analysis, as done for example in [Moe95], shows that the scattering length behaves like (shown in figure 2.2 (b))

$$a = a_{bg}\left(1 + \frac{\Delta}{B - B_0}\right), \tag{2.14}$$

where a_{bg} is the background scattering length, Δ is the width of the resonance and B_0 is the magnetic field where the resonance occurs.

The coupling of the different channels leads to an avoided crossing between the molecular state and the scattering state. It is then possible to adiabatically enter the molecular state by performing sufficiently slow magnetic field ramps over the resonance. For large positive values of the scattering length, the bound molecular state has a binding energy $E_B = \hbar^2/(ma^2)$, where m is the mass of a ^{6}Li atom (see 7.1).

Feshbach resonances in ^{6}Li

For the three lowest hyperfine states of ^{6}Li we have three different scattering lengths for the respective channels, namely a_{12}, a_{13} and a_{23}. All of them exhibit at least one broad Feshbach resonance for magnetic fields below 1000 Gauss. A molecular state in the highest vibrational excitation level ($\nu = 38$) of the singlet potential is responsible for them. The bound state splits into several hyperfine states due to the addition of two nuclear spin $I = 1$ atoms. Their resulting quantum numbers are $F = 0$, $m_F = 0$ and $F = 2$, $m_F = \pm 2, \pm 1, 0$ and they cause broad Feshbach resonances (width about 300 Gauss) in each scattering channel

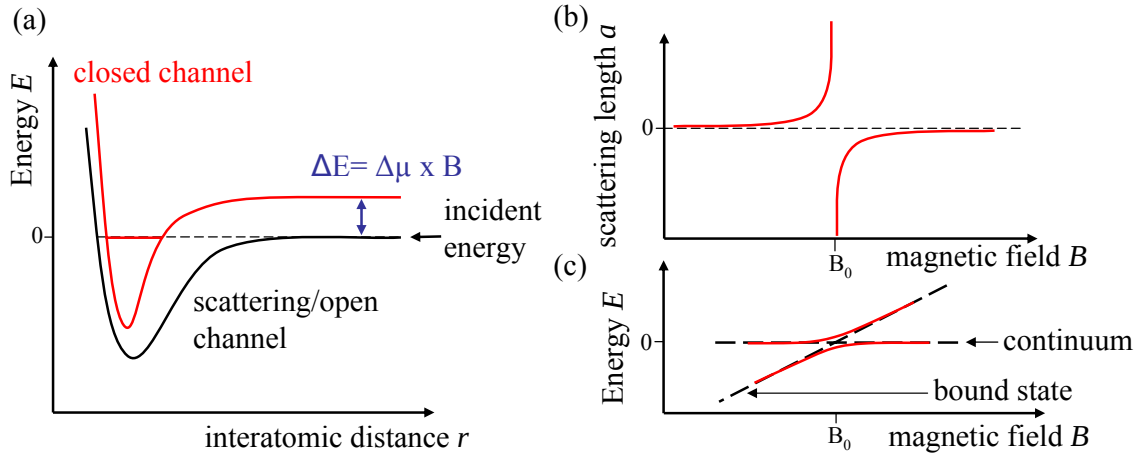

Figure 2.2: A magnetic Feshbach resonance occurs when a bound state of the closed channel coincides with the continuum of the scattering/open channel (a). This leads to a resonant enhancement of the scattering length (b). The coupling between the open and the closed channel results in an avoided crossing, which adiabatically connects the scattering state with the bound molecular state (c).

and an additional narrow resonance in the $|1\rangle|2\rangle$ channel at 543 Gauss (see table 2.1).

Scattering channel	Molecular state	Position
$\|1\rangle\|2\rangle$	$\nu = 38,\ F = 0,\ m_F = 0$	834 Gauss
$\|1\rangle\|3\rangle$	$\nu = 38,\ F = 2,\ m_F = -1$	691 Gauss
$\|2\rangle\|3\rangle$	$\nu = 38,\ F = 2,\ m_F = -2$	811 Gauss
$\|1\rangle\|2\rangle$	$\nu = 38,\ F = 2,\ m_F = 0$	543 Gauss

Table 2.1: S-wave Feshbach resonances in the three lowest hyperfine states of ^{6}Li, with the responsible bound state and the position of the corresponding resonance. The lowest resonance shown is the narrow one (width of about 100 mGauss), the others have widths of about 300 Gauss.

To obtain the complete scattering length in all channels, one also needs to include the background scattering length. For our system, the scattering (open) channels change from a superposition state in the Zeeman regime (e.g. triplet and singlet for $|1\rangle|2\rangle$ channel) to an almost pure triplet state in the Paschen-Back regime. Thus the background scattering length varies from small positive values at zero magnetic fields to the large negative triplet scattering length of about $-2000\,a_0$

for large fields ($\gtrsim 600$ Gauss). A careful calculation, for example in the coupled channels model, results in the scattering lengths shown in figure 2.3.

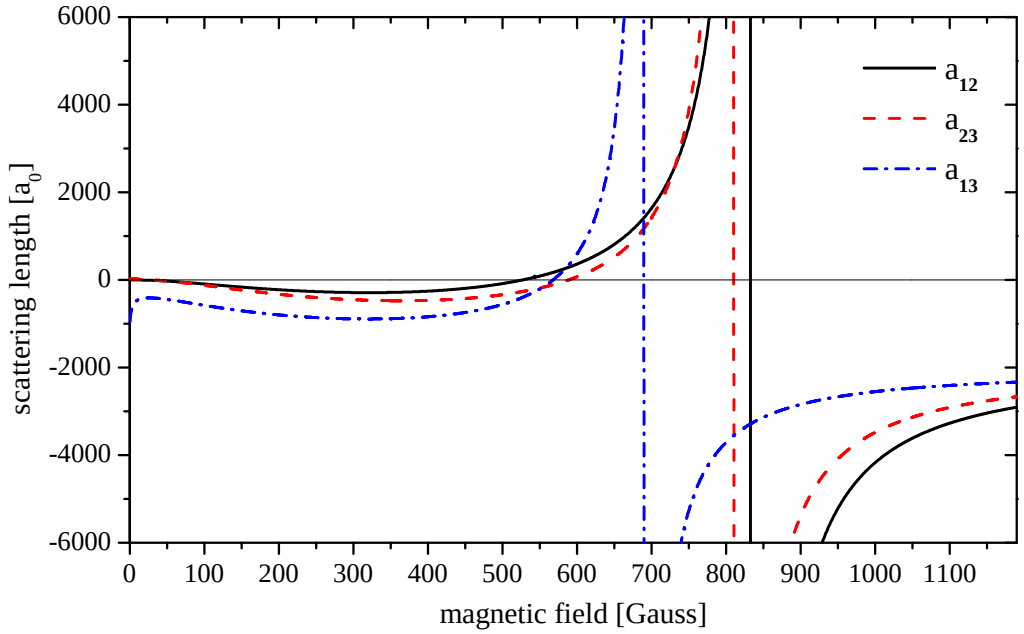

Figure 2.3: Scattering lengths in Bohr radii as a function of the magnetic field between the three lowest hyperfine states of ^{6}Li (from [Jul]).

2.1.4 Universality and Unitarity in Ultracold Gases

Universality and unitarity are two fundamental concepts in the theoretical treatment of ultracold gases. These terms and their implications will be frequently used in the course of this thesis. Therefore, it is essential to give a definition of these concepts.

Universality implies that physical systems behave identical in certain limits at long distances, regardless whether they differ substancially at short distances. In the low-energy limit systems with large scattering lengths (always compared to the short range length scale of the problem) are insensible to the details of the interatomic potentials, which are significantly smaller than the scattering length a.

The short range length scale of our problem (denoted by r_0), is given by the size of the interatomic potential. Neutral atoms interact through a van der Waals potential, thus the short range length scale of our system is the van der Waals length $r_0 = l_{vdW}$. This effective range can be obtained from the attractive part of

the van der Waals potenial $V = -\frac{C_6}{r^6}$ and is defined as

$$l_{vdW} = \left(\frac{m\,C_6}{\hbar^2}\right)^{1/4}. \tag{2.15}$$

For ^{6}Li this range is given by $l_{vdW} = 62.5\,a_0$ [Joc04, Bra08].

We noted that universal effects occur for large scattering lengths $a \gg l_{vdW}$. The corrections to that behavior scale with powers of $l_{vdW}/\,|a|$. Hence there are two limits where the universal predictions become exact:

1. the scaling limit: a is fixed and $r_0 \to 0$,

2. the unitary (or resonant) limit: r_0 is fixed a, but $a \to \pm\infty$.

In the unitary limit the scattering length is so large that it can no longer be used to describe the observables of the system. For low energies, ka diverges in the unitary limit. Then the cross section defined in equation 2.13 becomes independent of the scattering length and depends only on the inverse of the wave number. Thus when we later use the term "unitary interactions" or "unitary regime", we mean a region where the scattering length diverges (for example due to a Feshbach resonance) and the only remaining length scale is the interparticle spacing ($n^{-1/3}$). In this limit, universality is applicable and even exact. For a degenerate Fermi gas the interparticle spacing is proportional to the inverse of the Fermi momentum $1/k_F$ (with $k_F = \sqrt{2mE_F/\hbar^2}$). From this it follows that, for instance, the Fermi energy of an unitary interacting Fermi gas is rescaled by a universal constant β [Car03, Hei01, Ho04] with respect to the Fermi energy (E_F) of an ideal gas:

$$E_{F,unitary} = (1+\beta)E_F. \tag{2.16}$$

However, in the scaling limit which is the limit we will consider in our experiments, universal effects can also occur. For the two-body sector, the universal predictions for the scaling limit are relatively simple. They state that the two-body observables in the low-energy limit can only depend on a single parameter (namely the scattering length a), which has the dimension of length. Examples for such universal observables are the two-body cross section (given in equation 2.13) or the two-body bound state that exists for $a > 0$ with a binding energy of $E_B = \hbar^2/(m\,a^2)$ [Bra06]. This manifestation of universality occurs due to a continuous scaling symmetry, which means that in the scaling limit the system is invariant if one rescales all relevant parameters (scattering length, coordinate $\boldsymbol{r}$ and time t) by appropriate powers of a number λ>0:

$$a \to \lambda a, \quad \boldsymbol{r} \to \lambda \boldsymbol{r}, t \to \lambda^2 t. \tag{2.17}$$

This symmetry under scaling of the system is a consequence of the fact that a is the only length scale of the system. The corrections to these universal behaviors come from the s-wave effective range and scale with $l_{vdW}/\left|a\right|$. Thus effects of universality can be observable even if the scattering length is only several times larger than the effective range l_{vdW}.

For the three-body sector the universal predictions in the scaling limit are more complex: one obtains a discrete scaling symmetry for three-body observables. This discrete symmetry implies that the system is invariant not for arbitrary λ but for all powers of a certain fixed number λ_0. One can calculate λ_0 to be $e^{\pi/s_0} \approx 22.7$, with $s_0 = 1.00624$. Thus the discrete scaling symmetry can be written as

$$\kappa_* \to \kappa_*, \quad a \to \lambda_0^n a, \quad \boldsymbol{r} \to \lambda_0^n \boldsymbol{r}, \quad t \to \lambda_0^{2n} t, \tag{2.18}$$

where κ_* is a possible choice for the three-body parameter (sometimes called Efimov parameter), which sets an additional scale for the three-body sector. It can be thought of as the three-body analog to the scattering length in the two-body case. It effectively summarizes the effects for the long-range behavior of the three-body system stemming from the short-range characteristics of the three-body interaction potential.

The universal observables for the three-body case can only depend on the scattering length and the three-body parameter (e.g. κ_*). A thorough analysis shows that universality predicts an infinite number of three-body bound states (called "Efimov" states or trimers) for $a \to \pm\infty$ and in this limit their energy spectrum has the following form:

$$E_{trimer}^{(n)} = \left(e^{-2\pi/s_0}\right)^{n-n_*} \frac{\hbar^2 \kappa_*^2}{m}. \tag{2.19}$$

The corrections to this behavior scales logarithmically ($\sim \ln(\left|a\right|/l)$) and thus they cannot be treated as perturbations for $\left|a\right|/l_{vdW} \to \infty$.

To sum up, we can state that for large but not-diverging scattering lengths, the scaling limit is a reasonable approximation and universality is applicable. Therefore the scattering length and the three-body parameter are the only relevant parameters in all physical observables of the system. For the unitary limit ($a \to \pm\infty$), the scattering length does not provide a length scale, but the behavior is still universal. Thus when we speak of the universal regime, we mean a region where the scattering length a is significantly larger than l_{vdW}. It turns out that for most experiments $a > 5l_{vdW}$ [Web03b, Kra06b, Ott08] is already sufficient to observe universal effects, but for those values there are definitively some corrections to the universal behavior.

2.2 Ultracold Fermi Gases in Traps

The density distribution of an ultracold gas in a trap is one of the parameters which is directly accessible in experiments, e.g. by absorption imaging. From this parameter one deduces the temperature, shape and atom number of the sample. The spatial and momentum distributions are normally Gaussian, but as soon as one enters the quantum degenerate regime the distributions are altered. For bosonic gases, a phase transition occurs and a Bose-Einstein condensate is formed. The case is somewhat different for fermions. Here the influence of quantum degeneracy smoothly increases for temperatures lower than the Fermi temperature T_F. For attractively interacting Fermi gases, Bardeen, Cooper and Schrieffer (BCS) [Bar57] showed that below a critical temperature, which is smaller than T_F, so-called Cooper pairs are formed. These pairs then "Bose"-condense and form a BCS superfluid. This phase transition occurs at $T \sim 0.2\,T_F$ for strongly interacting fermions. The temperatures so far achievable in our three-component Fermi gases are still about a factor of two larger than this value. Thus we will not deal with fermionic superfluidity in this theoretical consideration. Since the treatment of interacting Fermi gases inside traps is theoretically very elaborate (and in fact for most cases only perturbatively possible, if at all), we will focus on the case of non-interacting Fermions. As we produce our three-state samples near the zero-crossings of all possible scattering lengths (near 550 Gauss, see figure 2.3) and since we perform our thermometry also in that region, neglecting the effects of interaction should be a good approximation.

Since we mostly deal with relatively large particle numbers (> 50 000) and the level spacing inside our harmonic traps is significantly smaller than the thermal energy of the sample, we can neglect the quantization in the trapping potential and use formulas deduced in the thermodynamical limit for a continuous density of states.

The trapping potential of our cigar-shaped harmonic trap can be written as $V(\boldsymbol{r}) = \frac{1}{2}m\omega_r^2(x^2 + y^2 + \lambda^2\, z^2)$, where ω_r is the radial and $\omega_a = \lambda\,\omega_r$ is the axial trapping frequency. One can thus define the mean trap frequency $\bar{\omega} = \left(\omega_r\,\omega_r\,\omega_a\right)^{1/3}$. In most cases it will be sufficient to consider a spherically symmetric trap with the mean trap frequency $\bar{\omega}$.

Since this problem has been discussed in several publications [But97, Joc09], we will focus on a short derivation of all relevant quantities.

In the limits described above and with the Hamiltonian $H(\boldsymbol{r},\boldsymbol{k}) = \hbar^2\,\boldsymbol{k}^2/2m + V(\boldsymbol{r})$, the Fermi distribution function takes the form

$$f(\boldsymbol{r},\boldsymbol{k}) = \frac{1}{\exp\left(\left(H-\mu\right)/k_B T\right)+1}. \tag{2.20}$$

With a density of states of $1/(2\,\pi\,\hbar)^3$ per unit volume in the six-dimensional phase

space ($\boldsymbol{r}, \boldsymbol{k}$), one can implicitely define the chemical potential by the following normalization condition on the particle number N:

$$N = \frac{1}{(2\,\pi\,\hbar)^3} \int f(\boldsymbol{r}, \boldsymbol{k})\, d\boldsymbol{r}\, d\boldsymbol{k}. \tag{2.21}$$

Assuming the harmonic potential described above and by variable substitution, one can simplify this to

$$N = \frac{1}{2\,(\hbar\bar{\omega})^3} \int_0^\infty \frac{E^2}{\exp\left((E-\mu)/k_B T\right)+1} dE. \tag{2.22}$$

For $T = 0$, the Fermi distribution function $f(\boldsymbol{r}, \boldsymbol{k})$ is unity for $E < E_F \equiv \mu(T = 0, N)$ and zero above, thus the integration of equation 2.22 gives

$$\mu(T = 0, N) = E_F = (6\,N)^{1/3}\ \hbar\bar{\omega}, \tag{2.23}$$

which can be used to define the Fermi energy, the Fermi temperature ($k_B\,T_F = E_F$) and the Fermi wave number $\hbar^2 k_F^2/2m = E_F$. With this chemical potential, we can calculate the density and momentum distribution for $T = 0$, by integrating $\frac{1}{(2\,\pi\,\hbar)^3}\, f(\boldsymbol{r}, \boldsymbol{k})$ over $\boldsymbol{k}$ or $\boldsymbol{r}$ respectively. Thus the resulting density distributions for zero temperature are:

$$\begin{aligned} n(\boldsymbol{r}, T = 0) &= \frac{1}{\pi^2\hbar^3}(2m(E_F - V(\boldsymbol{r})))^{3/2}, \\ &= \frac{8\,N}{\pi^2 x_F y_F z_F}\left(1 - \frac{x^2}{x_F^2} - \frac{y^2}{y_F^2} - \frac{z^2}{z_F^2}\right)^{3/2}, \end{aligned} \tag{2.24}$$

$$n(\hbar\boldsymbol{k} = \boldsymbol{p}, T = 0) = \frac{8\,N}{\pi^2 p_F^3}\left(1 - \frac{\boldsymbol{p}^2}{\boldsymbol{p}_F^2}\right)^{3/2}, \tag{2.25}$$

where we use the Fermi momentum and radii defined by

$$E_F = \frac{p_F^2}{2\,m} = \frac{1}{2} m\omega_x x_F = \frac{1}{2} m\omega_y y_F = \frac{1}{2} m\omega_z z_F. \tag{2.26}$$

The equations 2.24 and 2.25 are only defined for $n > 0$; densities are zero beside that regions. This means that for zero temperature, the "Fermi sea" fills the trap up to the corresponding Fermi radius or momentum.

2.2.1 Fermi Distribution for Non-Zero Temperature

The density distribution of a Fermi gas inside a trap is more complex for non-zero temperatures. Here, the chemical potential cannot be calculated analytically as it

is the case for $T = 0$. Nevertheless, to simplify the results, it is useful to define the Fermi-Dirac integral function [Rho50, Goa93, Goa95] [1]

$$f_\nu(z) = \frac{1}{\Gamma(\nu)} \int_0^\infty \frac{t^{\nu-1}}{\frac{1}{z}\exp(t)+1} dt. \tag{2.27}$$

Sometimes the polylogarithm is also used to describe the Fermi-Dirac integral function[2]. They are connected via the following relation:

$$-\mathrm{Li}_\nu(-\mathrm{z}) = \frac{1}{\Gamma(\nu)} \int_0^\infty \frac{\mathrm{t}^{\nu-1}}{\frac{1}{\mathrm{z}}\exp(\mathrm{t})+1} \mathrm{dt} = \mathrm{f}_\nu(\mathrm{z}). \tag{2.28}$$

For $|z| < 1$, these functions can be written as a power series:

$$f_\nu(z) = -\mathrm{Li}_\nu(-\mathrm{z}) = \sum_{\mathrm{k}=1}^{\infty} \frac{(-1)^{\mathrm{k}+1}\,\mathrm{z}^{\mathrm{k}}}{\mathrm{k}^\nu}. \tag{2.29}$$

In this representation it is easy to see that with $z = e^x$ the Fermi-Dirac integral satisfies

$$\frac{d}{dx} f_\nu(x) = f_{\nu-1}(x). \tag{2.30}$$

In [Rho50, Goa93] it was shown that this relation is actually true for all real x and ν. Thus 2.30 can later be used to integrate $f_\nu(e^x)$, for instance, to obtain the doubly-integrated one-dimensional axial density distribution $n(z)$.

With those definitions, the density and momentum distribution take the form

$$n(\boldsymbol{r}, T) = \left(\frac{m k_B T}{2\pi\hbar^2}\right)^{3/2} f_{3/2}\left(\exp\left(\frac{\mu - V(\boldsymbol{r})}{k_B\, T}\right)\right), \tag{2.31}$$

$$n(\boldsymbol{p}, T) = \frac{1}{\hbar\omega_x\omega_y\omega_z}\left(\frac{k_B T}{2\pi}\right)^{3/2} f_{3/2}\left(\exp\left(\frac{\mu - p^2/2m}{k_B\, T}\right)\right). \tag{2.32}$$

The normalization of the atom number is now given by

$$N = \left(\frac{k_B T}{\hbar\bar{\omega}}\right)^3 f_3\left(\exp\left(\frac{\mu}{k_B T}\right)\right). \tag{2.33}$$

and thus by using equation 2.23, one can obtain a relation, which implicitely defines the chemical potential as a function T/T_F

$$f_3\left(\exp\left(\frac{\mu}{k_B T}\right)\right) = \frac{1}{6(T/T_F)^3}. \tag{2.34}$$

[1] Note that they define the Fermi-Dirac integral slighty different: $f_\nu(z = exp(x)) = F_{\nu-1}(x)$.

[2] The polylogarithm $Li_\nu(z)$ describes the Bose-Einstein distribution function and thus one has to use $-Li_\nu(-z)$ for Fermions.

This equation is only numerically solvable for arbitrary T/T_F (see figure 2.4), but for small temperatures ($T/T_F \ll 1$), the chemical potential can be described by the Sommerfeld approximation (see e.g. [But97]), which states

$$\mu(T) = E_F \left(1 - \frac{\pi^2}{3} \left(\frac{T}{T_F}\right)^2\right). \tag{2.35}$$

For high temperatures ($T/T_F > 1$) the chemical potential can be approximated by the classical value

$$\mu(T) = -k_B T \ln\left(6 \left(\frac{T}{T_F}\right)^3\right). \tag{2.36}$$

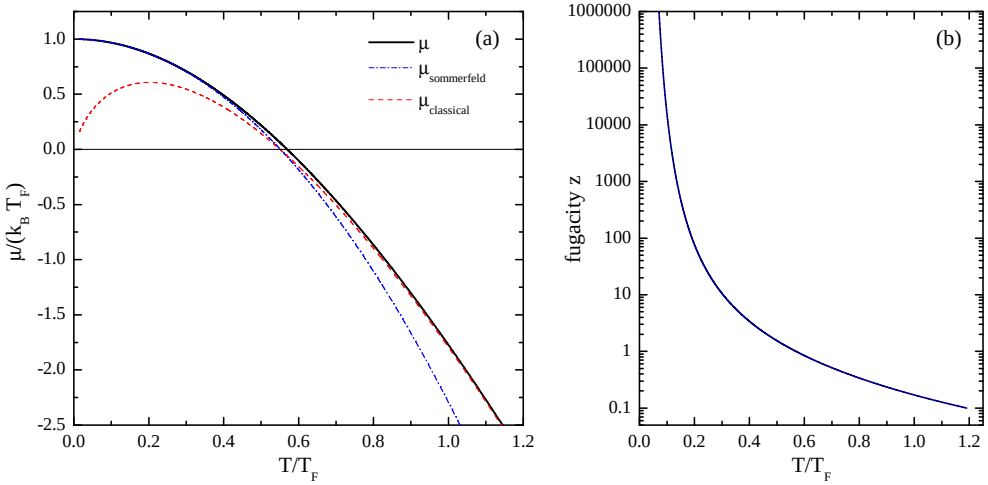

Figure 2.4: Chemical potential μ (see (a)) and fugacity $z = \exp\left(\frac{\mu}{k_B T}\right)$ (in (b)) of a non-interacting Fermi gas in a harmonic trap as a function of temperature. These values were obtained by solving equation 2.34 numerically. In (a), the dash-dotted line shows the Sommerfeld approximation and the dashed line shows the classically calculated chemical potential. The fugacity diverges for $T/T_F \to 0$, which makes the evaluation of $f_\nu(z)$ difficult, since the series expansion given in equation 2.29 cannot be used to calculate the Fermi-Dirac integral function.

With the chemical potential given above, one can now calculate the density distribution as a function of the temperature in a harmonic trap (see figure 2.5). One clearly sees that for low temperatures ($T/T_F \lesssim 0.3$) the change of the density distribution due to temperature is only minor and occurs mostly at the edge of the distribution. This makes it very difficult to extract the accurate temperature from experimentally determined density distributions. For more details on our thermometry, see section 5.5.

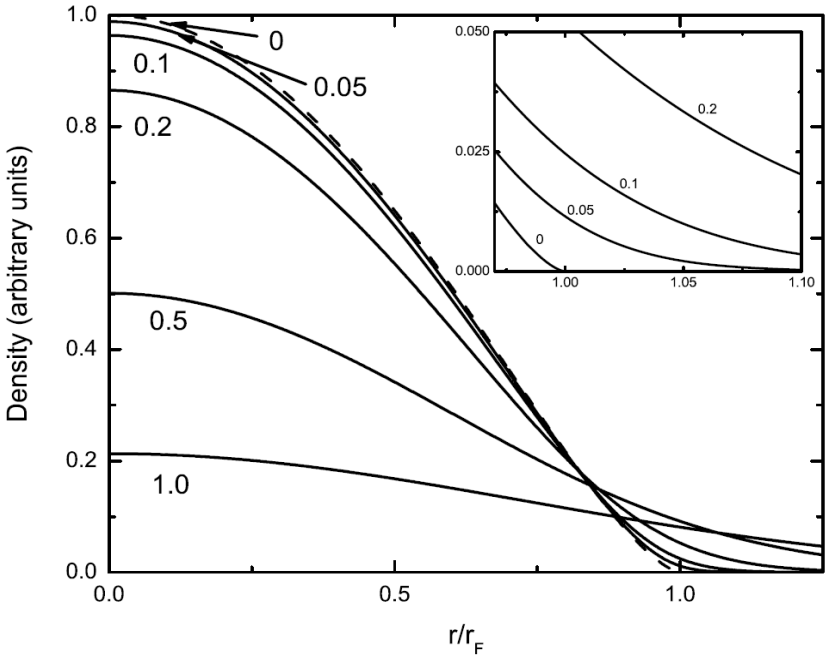

Figure 2.5: Density distribution of a non-interacting Fermi gas inside a harmonic trap for different temperatures T/T_F. r_F is the Fermi radius in a spherically symmetric trap and is defined in equation 2.26. The inset in particular shows that only minor changes occur in the density profile for low temperatures. Figure taken from [Joc09].

Chapter 3

Universal Three-Body Physics in a Three-Component Fermi Gas

In order to later describe the physical processes occuring in a three-component Fermi gas, we have to first give a brief overview on the three-body problem and the influence of universality on a three-body system. Universality predicts a sequence of three-body bound states, named after V. Efimov who first predicted their occurence in the 1970s [Efi71, Efi70]. These "Efimov"states are a universal generalization of the trimer state L. H. Thomas predicted 35 years earlier in a system of two neutrons and a proton [Tho35]. In our discussion, we will follow parts of the review article by E. Braaten and H.W. Hammer [Bra06], which explains these concepts in detail and also shows their influence on cold atoms.

In the previous chapter, we saw that the implications of universality on ultracold two- and three-body systems are manifold. To explain the universal behavior of a three-body system, we introduce the hyperspherical formalism, a set of spherical coordinates, which facilitate qualitative insight to the three-body problem. Afterwards, we use the Faddeev equations describing the three-particle scattering (especially for pairwise interaction) to derive the hyperspherical potential. With those results we are able to qualitatively understand Efimov's scenario. We then derive an analytic expression for the three-body loss coefficient K_3, using Efimov's radial law [Efi79]. The universal three-body bound states (Efimov trimers) lead to a resonant enhancement of K_3 for certain interaction strengths, commonly called Efimov resonances. With the formulas derived here, we will later be able to explain and interpret our experimental data (see Chapter 6).

Most of the concepts described in this chapter were initially developed for three identical bosons. But since the three different hyperfine states are distinguishable fermions, they do not experience the Pauli exclusion principle. Thus by changing certain numerical prefactors, the bosonic theory can be directly applied to our case. In principle, interaction in a three fermion system can be asymmetric (three

different two-body scattering lengths a_{12}, a_{13} and a_{23}). But as we will later show, one can combine them to a mean effective scattering length (see section 6.3.1). Thus we will now ignore the different two-body interaction strengths and consider only one scattering length a. In our case, the three different states are different Zeeman sublevels of the same ^{6}Li atom, consequently they all have the same mass m and we will use the terms "trimer" for three-body bound states and "dimer" for two-body bound states.

3.1 Theoretical Considerations on the Three-body Problem

The three-body problem is one of the oldest physical problems around. In the 17th century, Newton already considered a system consisting of three mass points attracted to each other by gravity. While the two-body problem is integrable and, for most cases, well understood, the three-body problem can become arbitrarily complex and is far from being fully understood. Similar to the classical problem, the quantum mechanical three-particle problem has been a subject of thorough research since the dawn of quantum mechanics. It was L. D. Faddeev who introduced a set of equations [Fad61], which significantly simplified the problem in case of pairwise interactions.

In most cases, the three-body problem is considered in a hyperspherical framework, which we will introduce in the following section. This will already give qualitative insight to the consequences of universality for the three-body problem.

3.1.1 The Hyperspherical Formalism

Let us consider the stationary Schrödinger equation for three atoms (with mass n) at positions $\boldsymbol{r}_1$, $\boldsymbol{r}_2$ and $\boldsymbol{r}_3$ and interacting through a potential V:

$$\left(-\frac{\hbar^2}{2\,m}\sum_{i=1,2,3}\Delta_i + V(\boldsymbol{r}_1,\boldsymbol{r}_2,\boldsymbol{r}_3)\right)\,\Psi(\boldsymbol{r}_1,\boldsymbol{r}_2,\boldsymbol{r}_3) = E\,\Psi(\boldsymbol{r}_1,\boldsymbol{r}_2,\boldsymbol{r}_3), \qquad (3.1)$$

where $\Psi(\boldsymbol{r}_1,\boldsymbol{r}_2,\boldsymbol{r}_3)$ is the three-atom wavefunction. If the interaction potential is translationally invariant, it can be described by only six independent coordinates. The same is also true for the wavefunction Ψ.

We choose a hyperspherical respresentation to facilitate the treatment of the three-body problem. A comprehensive review on this formalism is given in [Nie01]. The relative coordinates of two atoms are defined by $\boldsymbol{r}_{ij} = \boldsymbol{r}_i - \boldsymbol{r}_j$ and the separation of the third atom from the center-of-mass of the other two is given by

$\boldsymbol{r}_{i,jk} = \boldsymbol{r}_i - \frac{1}{2}\left(\boldsymbol{r}_j + \boldsymbol{r}_k\right)$ (see figure 3.1). Using these relations, we can define the hyperradius R

$$R^2 = \frac{1}{3}\left(\boldsymbol{r}_{12}^2 + \boldsymbol{r}_{13}^2 + \boldsymbol{r}_{23}^2\right), \tag{3.2}$$

which represents the radial coordinate in the hyperspherical representation. The other parameters are called hyperangular variables (summarized by Ω) and a possible choice for them is one of the hyperangles α_k (defined by $\alpha_k = \arctan\left(\frac{\sqrt{3}r_{ij}}{2\,r_{k,ij}}\right)$) and the unit vectors $\boldsymbol{e}_{ij}$ and $\boldsymbol{e}_{k,ij}$.

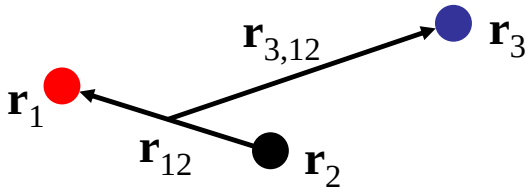

Figure 3.1: Example of a relative coordinate of two atoms $\boldsymbol{r}_{ij}$ and the separation of the third atom from their center-of-mass $\boldsymbol{r}_{k,ij}$.

In this coordinate system, the Schrödinger equation for the center-of-mass wavefunction can be written as

$$\left(T_R + T_{\alpha_k} + \frac{\Lambda_{k,ij}^2}{2\,m\,R^2} + V(R,\Omega) - E\right)\Psi(R,\Omega) = 0, \tag{3.3}$$

where T_R is the hyperradial kinetic energy, T_{α_k} is the kinetic energy term resulting from the hyperangle α_k and $\Lambda_{k,ij}$ is the generalized angular momentum. In principle, one could now solve this equation but it is advisable to first apply several simplifications and thus use the Faddeev equations.

3.1.2 The Faddeev Equations

The Faddeev equations are a set of equations that describe the quantum mechanical three-body problem for short range interactions [1] and additionally make use of the simplifications occuring in the case of a two-body cluster and a well separated atom. These equations can be deduced to be [Fad61]:

$$\left(T_R + T_{\alpha_1} + \frac{\Lambda_{1,23}^2}{2\,m\,R^2}\right)\psi^{(1)} + V(r_{23})\left(\psi^{(1)} + \psi^{(2)} + \psi^{(3)}\right) = E\psi^{(1)}, \tag{3.4}$$

[1] With short range interactions we mean that one can use universality for the two-body problem. Thus one can neglect all corrections $\propto r_0/a$ and the two-body scattering lengths is the only length scale of the system (in our experiments $r_0 = l_{vdW}$).

with all cyclic permuations of $(1,2,3)$. If the functions $\psi^{(1)}$, $\psi^{(2)}$ and $\psi^{(3)}$ solve this equation, their sum

$$\Psi(\boldsymbol{r}_1,\boldsymbol{r}_2,\boldsymbol{r}_3) = \psi^{(1)}(\boldsymbol{r}_{23},\boldsymbol{r}_{1,23}) + \psi^{(2)}(\boldsymbol{r}_{31},\boldsymbol{r}_{2,13}) + \psi^{(3)}(\boldsymbol{r}_{12},\boldsymbol{r}_{3,12}) \tag{3.5}$$

solves the Schrödinger equation 3.3. If we now neglect all total and subsystem angular momenta[2], this simplyfies the wavefunction for three identical particles to

$$\Psi(\boldsymbol{r}_1,\boldsymbol{r}_2,\boldsymbol{r}_3) = \psi(R,\alpha_1) + \psi(R,\alpha_2) + \psi(R,\alpha_3). \tag{3.6}$$

The three Faddeev equations can be reduced to one by integrating the angular variables. The result is an integro-differential equation for $\psi(R,\alpha)$ called the low-energy Faddeev equation

$$\begin{aligned} &(T_R + T_\alpha - E)\,\psi(R,\alpha) = -V(\sqrt{2}R\sin\alpha) \\ \times\quad &\left(\psi(R,\alpha) + \frac{4}{\sqrt{3}}\int_{|\pi/3-\alpha|}^{\pi/2-|\pi/6-\alpha|} \frac{\sin(2\alpha')}{\sin(2\alpha)}\psi(R,\alpha')d\alpha'\right). \end{aligned} \tag{3.7}$$

To solve this equation, one uses a hyperspherical expansion, which expands the wavefunction $\Psi(R,\alpha)$ for each value of R into a complete set of functions $\Phi_n(R,\alpha)$, which depend on the hyperradius and one hyperangle α

$$\psi(R,\alpha) = \frac{1}{R^{5/2}\sin(2\,\alpha)}\sum_n f_n(R)\,\Phi_n(R,\alpha). \tag{3.8}$$

The $\Phi_n(R,\alpha)$ are chosen such that they satisfy the integro-differential eigenvalue equation for the α dependent part of equation 3.7:

$$\begin{aligned} -\quad &\frac{\partial^2}{\partial\alpha^2}\,\phi_n(R,\alpha) + \frac{2mR^2}{\hbar^2}V(\sqrt{2}\,R\sin\alpha) \\ \times\quad &\left(\phi_n(R\alpha) + \frac{4}{\sqrt{3}}\int_{|\pi/3-\alpha|}^{\pi/2-|\pi/6-\alpha|} d\alpha'\phi_n(R,\alpha')\right) = \lambda_n(R)\,\phi_N(R,\alpha) \end{aligned} \tag{3.9}$$

where $\lambda_n(R)$ are the corresponding eigenvalues. The expansion with respect to $f_n(R)\phi_n(R,\alpha)$ converges fast and thus $f_0(R,\alpha)\phi_0(R,\alpha)$ already gives a reasonable approximation for the wavefunction $\psi(R,\alpha)$.

One can now substitute the wavefunction in the low-energy Faddeev equation by its expansion and project the whole equation onto $\phi_n^*(R,\alpha)$. This simplifies equation 3.7 to a set of coupled differential equations for the hyperradial functions $f_n(R)$. If the channel eigenvalues vary sufficiently slow with R, several terms can

[2]This assumption can be justified by the suppression of angular momenta in the low-energy limit.

be neglected and the eigenvalue equations decouple. With further approximations (details in [Bra06]) the equations can be reduced to a radial Schrödinger equation for each hyperspherical potential:

$$\left[\frac{\hbar^2}{2m}\left(-\frac{\partial^2}{\partial R^2}+\frac{15}{4R^2}\right)+V_n(R)\right]\approx E f_n(R). \tag{3.10}$$

It is now possible to calculate the hyperradial potentials $V_n(R)$ and one obtains

$$V_n(R)=(\lambda_n(R)-4)\,\frac{\hbar^2}{2m\,R^2}, \tag{3.11}$$

where λ_n are eigenvalues of the integro-differential equation 3.9 and can be calculated numerically.

3.1.3 The Hyperspherical Potentials

An exact transcendental relation can be found for the channel eigenvalues $\lambda_n(R)$, so that the hyperspherical potentials can be determined. The numerical results for these calculations are shown in figure 3.2 (calculated in [Bra06]).

In the limit of zero range ($r_0 \to 0$) the potential scales with $1/R^2$ from 0 to $\sim |a|$. In general, the effective range is not zero, but $\ll |a|$. Thus the hyperspherical potential has to be cut off at the size of the short range length scale (in our case $r_0 = l_{vdw}$). For the region with $R < r_0$ this theory cannot make any predictions, but the effects for the long range behavior from short distances can be taken into account by imposing a boundary condition for the connection between short- and long-range behavior ($R \approx r_0$). This means that the hyperradial wavefunctions for $R < r_0$ have to be continuously connected to the wavefunctions with $R > r_0$. This can be done by only one additional parameter. This three-body parameter does the same as the scattering length for the two-body case: it unites all effects of the short-range characteristics of the interaction potential to a boundary condition for the long-range behavior.

The lowest hyperspherical potential is the only attractive one and thus the only one that supports bound states. These universal three-body bound states are called Efimov trimers. Since the potential scales with $1/R^2$, it actually supports an infinite number of states in the limit $|a| \to \infty$, with an accumulation point for zero binding energies. Thus the attractive long-range potential gives rise to the Efimov effect.

One can now define a scalar s_0 such that the lowest eigenvalue $\lambda_0 = -s_0^2$ for $R/a \to 0$. From numerical calculations one obtains $s_0 = 1.00624$. Additionally, one can define a wave number κ, which is related to the trimer binding energy

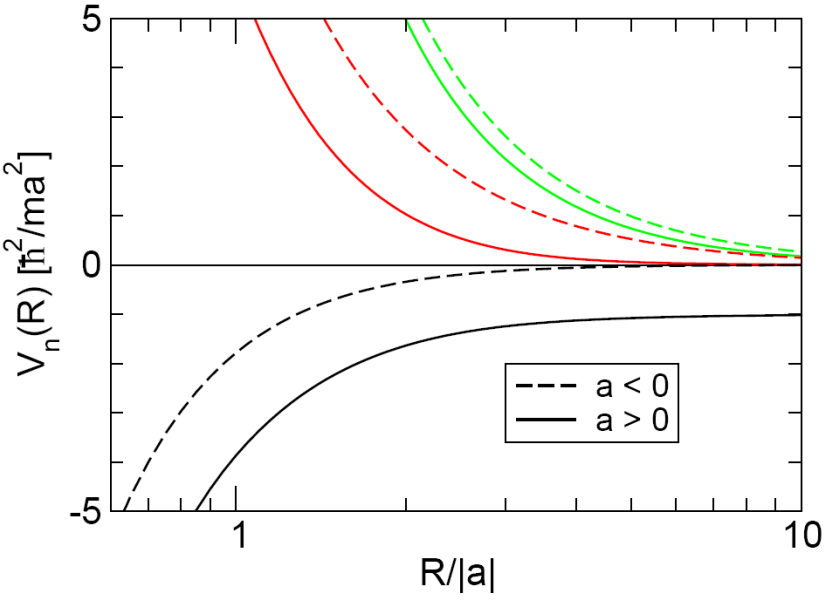

Figure 3.2: The three lowest hyperspherical potentials for $a > 0$ (solid lines) and $a < 0$ (dashed lines). The lowest potential is attractive and scales with $1/R^2$, all others are repulsive. In the limit of large hyperradius, the lowest potential for $a < 0$ approaches the free atoms threshold ($E = 0$), for $a > 0$ the potential reaches $-\frac{\hbar^2}{m\,a^2}$, which is the binding energy of the universal dimer. Figure taken from [Bra06].

$E_T = \frac{\hbar^2\kappa^2}{m}$ in the limit $|a| \to \infty$. Using these relations, one can solve the hyperradial equation 3.10 and it follows in the limit of $\kappa R \ll 1$:

$$f_0(R) \propto -\sqrt{\frac{\pi}{s_0 \sinh(\pi s_0)}}\, R^{1/2} \sin\left(s_0 \ln(\kappa R) + \alpha_0\right), \tag{3.12}$$

where α_0 is an universal phase.

Imposing the boundary condition for the connection between short- and long-range region, one obtains the following binding energies for the nth trimer state in the resonant limit $|a| \to \infty$:

$$E_T^{(n)} = \left(e^{-2\pi/s_0}\right)^{n-n_*} \frac{\hbar^2\kappa_*}{m}, \tag{3.13}$$

where κ_* is the wave number associated with the Efimov level $n = n_*$. Note that adjacent states are separated by a factor of $e^{2\pi/s_0} \approx 515.03$.

Using these results, we can qualitatively discuss the wavefunctions in the hyperspherical potential: There is a lowest universal bound state whose wavefunction

does not exhibit a node in the potential (for $R > r_0$). This respresents a lower bound of the Efimov spectrum. The wavefunctions of the next weaker bound state have one additional half-period and the binding energies are always separated by a factor of $e^{2\pi/s_0} \approx 515$ (see figure 3.3). The scattering length imposes an upper limit to the number of Efimov states. For a diverging, there is an infinite number of states. These states appear one after the other if the scattering length is increased. Thus one can estimate the number of possible Efimov states for a given scattering length by counting the nodes in the wavefunctions (see figure 3.3): $N_{states} \approx s_0/\pi \ln(|a|/r_0)$.

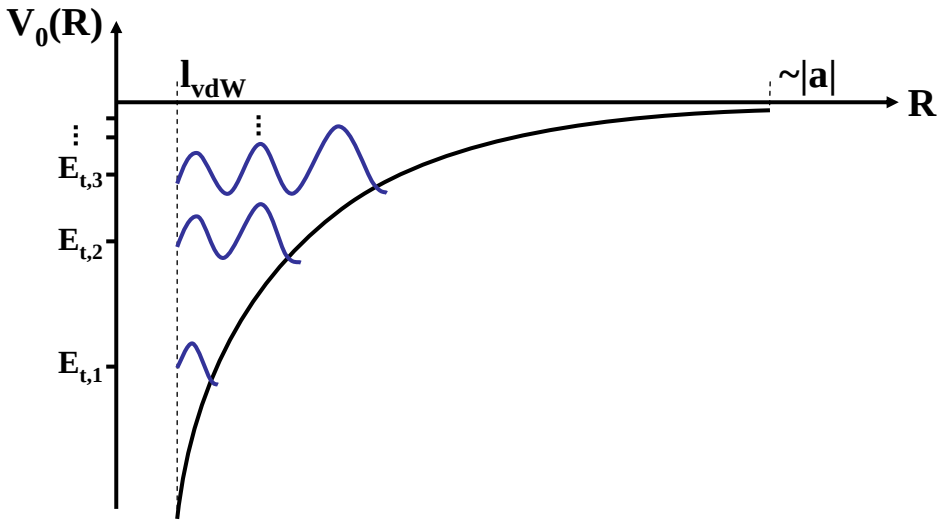

Figure 3.3: Sketch of the lowest hyperspherical potential with its short-range cut-off at $R \approx l_{vdW}$ and the long-range end at approximately $|a|$. The blue lines depict the radial probability distributions of possible bound states in this attractive long range potential. It shows that there is an infinite number of bound states with an accumulation point for zero binding energy for $|a| \to \infty$. To facilitate the visibility, the scaling factor $e^{2\pi/s_0}$ was chosen to be ~ 2 (not 515.3).

3.2 Efimov's Scenario

The essence of Efimov's predictions for the three-body sector can be best visualized in a graph, which plots the wave vector $K \propto \sqrt{E}$ versus the inverse of the scattering length (see figure 3.4). On the right-hand side of the figure the scattering length is positive, thus there exists an universal dimer state with a binding energy $E_B \propto 1/a^2$. On the left-hand side the interactions are attractive (a<0) and consequently no shallow two-body bound state exists. In the resonant region ($1/a \approx 0$), an infinite number of Efimov trimers exist.

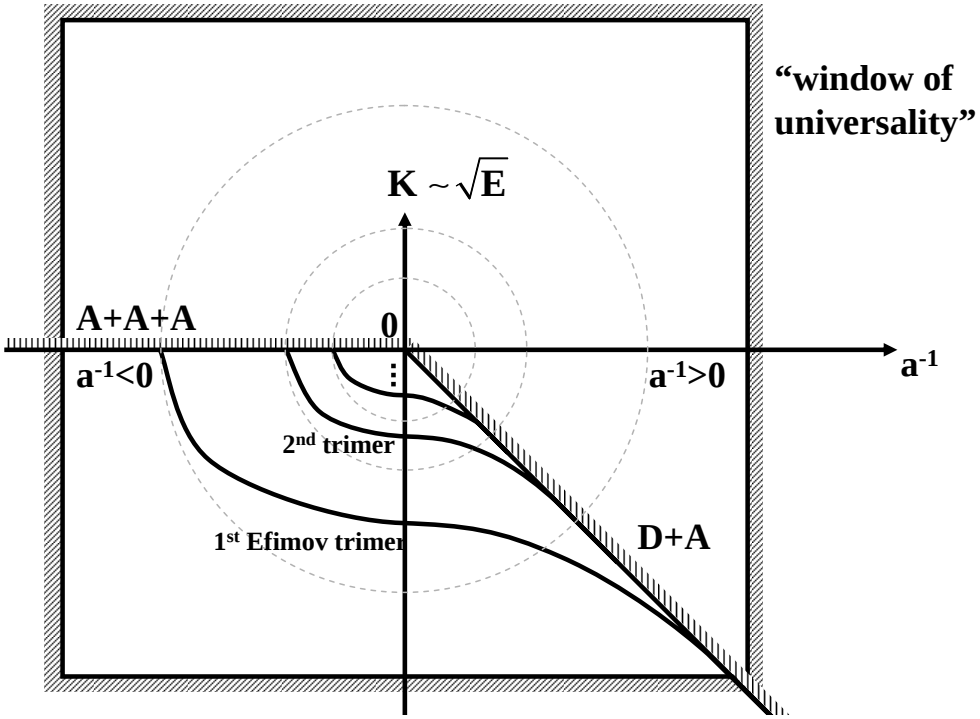

Figure 3.4: Sketch of the Efimov scenario as a function of the inverse of the scattering length. The infinite tower of Efimov trimer states is shown. These states exhibit an accumulation point at the zero-energy threshold for diverging scattering length ($1/a = 0$). Additionally, the universal dimer state plus free atom continuum (D+A) and the three atom threshold (A+A+A) are shown, both are depicted by vertically hatched regions. The "window of universality" gives the limit of the universal region and is defined by $\sqrt{K^2 + 1/a^2} \approx 1/r_0$ (illustrated by diagonally hatched region). On the (gray) dashed circles the three-body observables (scattering cross sections, binding energies etc.) differ only by a discrete scale transformation (scaling factor is ~ 2 to for clarity).

The absolute value of the binding energies of the Efimov trimers is governed by

the short range characteristics of the interaction potential. But once one of those energies is fixed (done by determining the three-body parameter, e.g. κ_*), all other trimer states are known because of the universal scaling behavior. On each dashed circle in figure 3.4, the observables, e.g. the scattering cross sections and the binding energies, differ only by the earlier calculated scaling factor $e^{2\pi/s_0}$ (and appropriate powers of $e^{2\pi/s_0}$) [Efi71, Efi70, Efi79]. Hence, they are connected by the discrete scaling transformation shown in section 2.1.4. For large scattering lengths these trimers connect the three atom continuum to the atom-dimer threshold.

At a certain interaction strength a trimer state can be formed, when starting at weak attractive interactions and moving towards the resonance on the three-atoms continuum. For a scattering length which is a factor of $e^{\pi/s_0} = 22.7$ larger the next trimer can be formed. Their binding energy on resonance is separated by a factor of about $e^{\pi/s_0} = 515$ (in figure 3.4 we changed the scaling factor to about 2 to improve clearness). The scaling factor changes outside the resonant region $1/a \approx 0$ because nonuniversal corrections cannot be neglected anylonger. Outside the universal regime, no predictions can be made with the methods described in the present chapter. The boundaries of the universal regime are depicted by the so-called "window of universality", which is defined by $\sqrt{K^2 + a^{-2}} \approx r_0^{-1}$. It is not clear what happens to trimer states outside this region.

3.2.1 Efimov Physics in Experiments

There are several atomic and nuclear systems, for which Efimov states were predicted, for example in a system of three ^{3}He nuclei (for more examples in nuclear physics see [Jen04]). In a system consisting of ^{4}He atoms, a nonuniversal Thomas trimer was found [Sch94] and there are predictions for an excited trimer state, which would be an Efimov trimer.

Until now, the only strong evidence for Efimov physics was observed in experiments performed at Innsbruck with an ultracold bosonic gas consisting of ^{133}Cs atoms [Kra06b]. The ability to tune the scattering length by means of Feshbach resonances seems to make ultracold gases the ideal system to study the effects predicted by Efimov. In those ultracold gases the formation of a trimer state can be observed as a resonant enhancement of three-body loss processes in the scattering of three free atoms. Since deeply bound dimer states exist in the case of ultracold atoms, the Efimov trimer opens an additional loss channel to a deeply bound dimer and a free atom. This process is called three-body recombination and will be described in more detail in chapter 6.2. The binding energy released in such a process is very large compared to the depth of the trapping potential and thus all particles involved leave the trap. The influence of universal trimer states on this three-body recombination into deep dimers plus free atom was cal-

culated by E. Braaten and H.W. Hammer [Bra06]. In the next section we will show how the three-body recombination rate is resonantly enhanced at certain interaction strengths for which a universal trimer hits the three atom threshold. These loss resonances are commonly reffered to as Efimov resonances. The crossing between an Efimov trimer and the atom-dimer threshold also leads to resonantly enhanced loss in a mixture consisting of atoms and dimers. Recently, there has been strong evidence for such a crossing in ^{133}Cs [Kno08].

There is an ongoing debate whether the lowest possible trimer should be an Efimov or a Thomas trimer [Lee07]. There are predictions that this particular trimer state never reaches the atom dimer continuum for positive scattering lengths because the state leaves the universal regime and then tunes parallel to the continuum. To avoid misconceptions and to clearly specify our statements, we call a trimer Efimov-like if the trimer is in the universal regime (a significantly larger than r_0). As a result, an Efimov resonance occurs if such a trimer crosses the continuum and enhances three-body loss. The trimer states (universal or not) are also referred to as Borromean states. Since the trimer state exists in a region where no two-body bound state is supported by the interatomic potential (at least for negative scattering lengths). Accordingly, if one of the atoms is removed from the trimer, the other two cannot remain bound in a dimer.

3.3 Analytic Results for Ultracold Three-Body Recombination

In this section, we will show how the crossing of a universal trimer state gives rise to a resonant enhancement of the three-body loss. For these considerations, we will use Efimov's radial law [Efi79] and proceed as done in [Bra06].

Three-body loss is normally described by the three-body recombination rate α, which provides the number of recombination events per second. It is connected to the three-body loss coefficient[3] K_3 by a numerical constant that counts the number of lost atoms per event (in our case 3). It could be shown in [Esr99, D'I04] that the three-body loss coefficient can be written as

$$K_3 = \sum_{i,f} \frac{C_* \hbar}{m K^4} \left| S_{f,i} \right|^2 , \tag{3.14}$$

where C_* is a numerical constant, K is the wave number ($\propto \sqrt{E}$) and $S_{f,i}$ is the S-matrix element of the reaction responsible for the loss (f and i correspond

[3]The three-body loss coefficient is defined by $\dot{n} = -K_3 n$, where n is the atomic number density.

to the final and initial state, respectively). To deduce the scaling of K_3 with the scattering length and the three-body parameters, we will have to examine the S-matrix element which describes the processes leading to three-body loss.

3.3.1 Efimov's Radial Law

Efimov's radial law [Efi79] uses the conservation of probability in elastic three-body processes to make universal predictions for the S-matrix dependence on the scattering length and the three-body parameter. Therefore, it is useful to define two new parameters H and ξ. They are the polar coordinates in figure 3.4: H is the radial coordinate that measures the distance from the origin and ξ is the angle measured with respect to the positive $1/a$ axis. Every point of the plane $(K, 1/a)$ can be expressed by (H, ξ) with this definition. The atom dimer threshold, for example, can be described by $(H, \xi = -\pi/4)$.

To derive how the S-matrix scales with the scattering length and the three-body parameter (or alternatively with H and ξ), it is useful to define the following regions for the hyperradius:

- asymptotic region: for $R \gg |a|$,
- long-distance region: for $R \sim |a|$,
- scale-invariant region: for $|a| \gg R \gg r_0$,
- short-distance region: for $R \sim r_0$.

In most of these regions at least approximate results can be found for the wavefunctions. If one neglects the effects of deeply bound dimer states (only for now), the only possible states in the asymptotic region are the three-atom scattering state (AAA) or the shallow dimer plus a free atom scattering state (AD), the latter state only exists for $a > 0$. The probability of the incoming states to evolve into outgoing states is governed by the square of the S-matrix $|S_{f,i}|^2$. Thus if one neglects deeply bound dimers, no inelastic processes occur and by imposing conservation of probability the hyperradial flux flowing to short distances (small R) has to eventually flow back to the asymptotic region either in the three-atom scattering state or in the atom-dimer scattering state.

The explicit wavefunction of the asymptotic AAA state with total energy $E = \hbar^2\kappa^2/2m$ can be expressed in terms of Bessel functions:

$$\psi_{AAA} \to 1/R^2 \left(F J_2(\kappa R) + G J_{-2}(\kappa R)\right), \tag{3.15}$$

with F and G numerical constants. An analogous expression can be found for the ψ_{AD}, with an outgoing and an incoming part described by constants C and D,

respectively. In the scale-invariant region $|a| \gg R \gg r_0$, the wavefunction in the low-energy limit can be calculated from the following hyperradial equation

$$\frac{\hbar^2}{2m}\left(-\frac{\partial^2}{\partial R^2}-\frac{s_0^2+1/4}{R^2}\right) f_0(R) \approx 0. \tag{3.16}$$

The most general solution to this can be written as a hyperradial wave (as of now denoted by $|hw\rangle$) with an incoming and an outgoing part described by numerical constants A and B.

If one normalizes all these states and defines the "in" direction for waves flowing into the long-distance region $R \sim |a|$ and "out" for waves flowing out of the long-distance region, we can denote all possible wavefunctions in the scale-invariant and asymptotic region by:

$$|hw\rangle = A|1,in\rangle + B|1,out\rangle, \tag{3.17}$$
$$|AD\rangle = C|2,out\rangle + D|2,in\rangle, \tag{3.18}$$
$$|AAA\rangle = F|3,out\rangle + G|3,in\rangle. \tag{3.19}$$

In the long-distance region $R \sim |a|$, the wavefunction can become very complicated and thus we are not able to give an expression for that. But since the hyperradial flux is conserved, this region can be summarized by an unitarity transformation $\hat{U}$ with a certain probability of reflection and transmission. Hence the S-matrix which describes an incoming asymptotic state passing through the long-distance region to the scale-invariant region is a unitary and symmetric (because of time reversal invariance) 3×3 matrix with the elements

$$s_{ij} = \langle i,out|\hat{U}|j,in\rangle. \tag{3.20}$$

In the short-distance region, the wavefunction becomes again very complicated. However, since the hyperradial flux is conserved (if there are no inelastic channels), the hyperradial wave has to be completely reflected at $R \sim r_0$. Consequently, the amplitudes of in- and outgoing hyperradial waves can only differ by a phase, which is accumulated during the reflection at short distances. Therefore, we can define $A = -e^{2i\theta_*}\, B$, with some angle θ_*.

Taking all this into account, we are now able to determine the S-matrix for low-energy atom-dimer and three-atom scattering

$$S_{AD,AD} = s_{22} + s_{21}e^{2i\theta_*}\frac{1}{1-e^{2i\theta_*}s_{11}}s_{12}, \tag{3.21}$$
$$S_{AD,AAA} = s_{23} + s_{21}e^{2i\theta_*}\frac{1}{1-e^{2i\theta_*}s_{11}}s_{13}, \tag{3.22}$$
$$S_{AAA,AAA} = s_{33} + s_{31}e^{2i\theta_*}\frac{1}{1-e^{2i\theta_*}s_{11}}s_{13}. \tag{3.23}$$

Note that not all states are possible for all points in the (H, ξ) plane. For instance, AAA only exists for $0 < \xi < \pi$. For all other regions AAA is kinematically forbidden. Similar constraints hold for AD (kinematically only allowed for $-\pi/4 < \xi < \pi/2$).

If the respective states are kinematically allowed, one can use the S-matrix elements to graphically explain what happens to the hyperradial flux during an interaction event (see figure 3.5). We particularly examine $S_{AAA,AAA}$ since this is the element we will later consider, but the other matrix elements can be explained in the same manner.

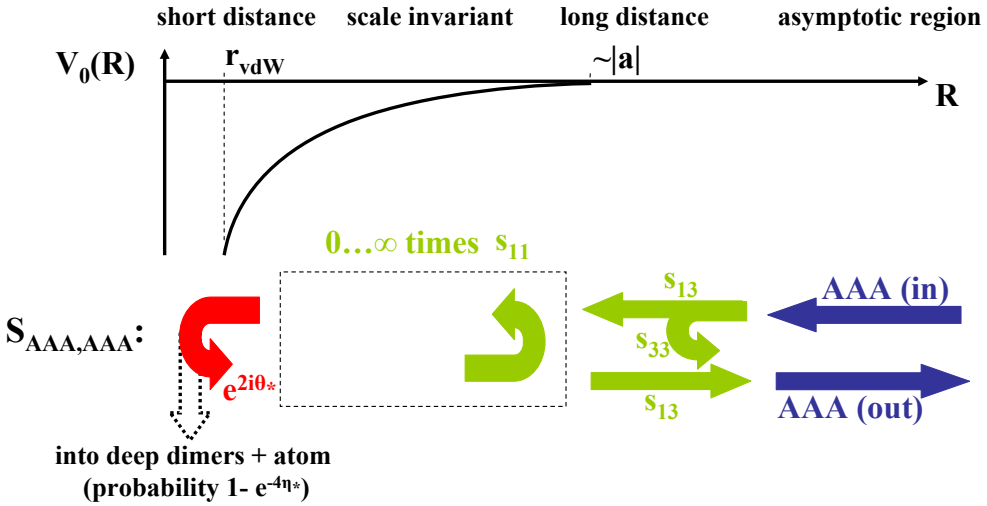

Figure 3.5: Graphic representation of the $S_{AAA,AAA}$ matrix element for elastic three-atom scattering for low energies in the hyperspherical potential. The behavior of the hyperradial amplitude flux for the scattering process described by $S_{AAA,AAA}$ is explained in the text. As we will later see (section 3.3.2) there is a probability to enter a deeply bound dimer states at short distances. This process can be described by a single parameter η_*.

In the asymptotic region, a three-atom scattering state approaches the long-distance region, a fraction of the incident hyperradial wave is directly reflected (s_{33}), the residual part passes this region and enters the scale-invariant regime, where it experiences the $1/R^2$ hyperspherical potential. There, the hyperradial flux flows to short distances and is completely reflected, because of the conservation of flux. In this process, it accumulates a phase shift $e^{2i\theta_*}$. Now the wave moves in outward direction until it reaches the long-distance region where a fraction is transmitted and reaches the asymptotic region in the AAA state. The rest is reflected from the long-distance region and flows again to short distances. This reflection at the long-distance region and the subsequent reflection at the short-distance region can

occur infinitely many times. The sum over all of these amplitude $\sum_n \left(e^{2i\theta_*} s_{11}\right)^n$ can be written as a geometric series, hence the result is $1/\left(1 - e^{2i\theta_*} s_{11}\right)$. The same considerations can be made for all other S-matrix elements by substituting the corresponding s_{ij}.

With the S-matrix elements as given above, the physical observables are strongly restricted. One can show that the radial variable H only enters the S-matrix through θ_* and ξ can only enter as an argument of the s_{ij}. From this, Efimov was able to show that, for example, the atom-dimer cross section depends log-periodically on the dimensionless factor $a\kappa_*$ and some universal constants describing the transmission and reflection from the long-distance region [Efi79]. The binding energies of the Efimov trimers can also be calculated from the relation given for the S-matrix, only by imposing $e^{2i\theta_*} = 1$, which means that the hyperradial flux enters the scale-invariant region and then remains "bound" there. Thus by using the conservation of the hyperradial flux we are able to give strong constraints on physical observables of this universal three-body system.

3.3.2 Effects of Deeply Bound Dimers

So far, we assumed that there are no deeply bound states which implies that all the hyperradial flux flowing to short distances has to be completely reflected. However, in the interaction potential of alkali atoms deeply bound states do exist (e.g. lower vibrational levels). This leads to a loss of a fraction of the flux to those states, because they form a deeply bound dimer and a free atom at short distances. The binding energies of those nonuniversal dimer states has to be larger than $E = \hbar^2/(mr_0^2)$ since they are not part of the scale-invariant regime and thus their size has to be smaller than r_0. The binding energy released in such a process is very large compared to all other energies of the system. So that the deeply bound atom and the free atom fly apart in a "high-energy" atom-dimer state.

To form a deeply bound state, the three atoms have to approximate each other to distances comparable to or smaller than r_0. In the low-energy limit, this is only possible in the lowest hyperspherical potential, which is proportional to $1/R^2$. Thus the entire flux emerging in the high-energy atom-dimer channel has to flow through this potential. As a result, the effect of all possible deeply bound state can be described by only one parameter η_*, which we will call the inelasticity parameter. This parameter can be added to the phase shift obtained during a reflection at the short-distance region ($e^{2i\theta_*}$) and the boundary condition on the amplitudes of the hyperradial waves at short distances is then:

$$A = -e^{-2\eta_* + 2i\theta_*} B. \tag{3.24}$$

This means that every time the hyperradial wave is reflected at the short-distance region, the probability to enter a deeply bound state is $\propto e^{-2\eta_*}$. One can now

rewrite Efimov's radial laws (equations 3.21, 3.22 and 3.23) including these deeply bound states by simply replacing the factor $e^{2i\theta_*}$ by $e^{-2\eta_*+2i\theta_*}$. Thus in the scaling limit all low-energy three-body observables are functions of just three parameters: the scattering length a, the three-body parameter κ_* and the inelasticity parameter η_*.

We can now generalize Efimov's radial law to transitions from normal scattering states (e.g. AAA) to high-energy atom-dimer scattering states (the kinetic energy may be large, but the total energy is still small), which we will denote by X. Although the wavefunction in the short-distance region is still very complicated we are again able to use the conservation of the total hyperradial flux. The sole difference is that we have to add an asymptotic high energy atom-dimer state X that is accessed through the hyperradial wave ($|hw\rangle$) in the short-distance region. The transition amplitude for this process is given by a t-matrix, which is defined analogous to s_{ij} in equation 3.20:

$$t_{ij} = \langle i, out|\hat{U}|j, in\rangle, \tag{3.25}$$

where $\hat{U}$ is an operator describing the evolution through the short-distance region. By defintion, the amplitude of a hyperradial wave to change from an incoming to an outgoing hyperradial wave is given by $t_{11} = e^{-2\eta_*+2i\theta_*}$. Thus the total probability for an incoming hyperradial wave to enter all possible high-energy states X is given by

$$\sum_X |t_{X1}|^2 = 1 - e^{-4\eta_*}. \tag{3.26}$$

From this we can obtain the S-matrix element for transitions between AD or AAA scattering states and the high-energy atom-dimer state X. Since we only need the case of negative scattering lengths in the later analysis of our experimental data, we will from now on focus on states without an universal dimer state and thus neglect the AD state. The relations in this case can be derived analogous to the case for negative scattering lengths and the results can be found in [Bra06].

The relevant S-matrix element for our later analysis is:

$$S_{X,AAA} = t_{X1}s_{13} + t_{X1}\, s_{11}e^{-2\eta_*+2i\theta_*}\frac{1}{1 - e^{-2\eta_*+2i\theta_*}s_{11}}s_{13}. \tag{3.27}$$

This S-matrix element describes the amplitude of a three-atom scattering state to evolve to a deeply bound dimer states and a free atom X. The first term in this equation is due to a three-atom scattering state, which passes the long-distance region to the scale-invariant one and afterwards directly enters the deep dimer plus free atom state X. The second term describes a transmission through the long-distance region and subsequently arbitrary reflections at the short-distance region and the long-distance region before accessing the high-energy scattering

state X. Both paths are graphically explained in figure 3.5 if one replaces θ_* by $\theta_* + i\eta_*$ and follows the dashed arrow downwards after the nth reflection from the short- and long-distance region.

The three-body recombination rate is proportional to the square of the respective S-matrix element, which can be calculated using relation 3.26:

$$\sum_x |S_{X,AAA}|^2 = (1 - e^{-4\eta_*}) \, |s_{13}|^2 \, \frac{1}{|1 - e^{-2\eta_* + 2i\theta_*} s_{11}|^2}. \tag{3.28}$$

Now we only need to know how s_{13} and s_{11} scale for low energies ($K \to 0$). The leading dependence of s_{13} on K can be obtained from threshold laws for three-body reactions (given in [Del60]) and the zero-energy value s_{11} was determined for example in [Mac05]:

$$s_{11} = e^{-2\pi s_0} e^{-2i\delta_0}, \tag{3.29}$$

$$s_{13} = -c_1 e^{-i\gamma_0} a^2 K^2 \, (1 + \dots), \tag{3.30}$$

where δ_0 is the s-wave phase shift, c_1 is a positive real constant and γ_0 is a real numerical constant.

With these relations, we are capable of calculating the three-body recombination rate and the three-body loss coefficient K_3 for negative scattering lengths in the low-energy limit. In a similar manner, we could also determine the elastic three-atom to atom-dimer cross section or the cross section from an atom-dimer scattering state to a high-energy atom-dimer state X. With the latter, one can deduce the dimer relaxation rate, which describes the number of processes from AD to X, which has been experimentally measured in Innsbruck [Kno08] recently.

As predicted by the concept of universality, all observables just mentioned only depend on three parameters (beside numerical constants): the scattering length, a three-body parameter and the inelasticity parameter, which is sometimes referred to as complex part of the three-body parameter.

3.3.3 Three-Body Recombination into Deeply Bound Dimers

The level-crossing between an Efimov trimer and the three-atom continuum leads to a resonant enhancement of the three-body loss, because the trimer state facilitates the formation of a deeply bound dimer and a free atom in a "high-energy" scattering state X. We calculated the S-matrix element for such a transition $AAA \to X$ as a function of the transition amplitudes s_{ij}. Using the relations 3.29 and 3.30 and with trigonometric relations, one obtains

$$\sum_x |S_{X,AAA}|^2 = C_0 a^4 K^4 \, \frac{\sinh(2\eta_*)}{\sin^2(\theta_* + \gamma) + \sinh(\eta_*)} \quad \text{for K} \to 0, \tag{3.31}$$

where C_0 and γ are appropriate numerical constants.

One can now define θ_* in terms of a different three-body parameter. To describe experiments, it is useful to use a_*, which is the value of the scattering length ($a_* < 0$) for which the trimer state hits the three-atom threshold. This three-body parameter can be analytically related to κ_* or other choices of a three-body parameter (see [Bra06]).

Accordinlgy, with equation 3.14 one can obtain for the three-body loss coefficient K_3 for negative scattering lengths ($a < 0$) in the low-energy limit:

$$K_3 = \frac{c \sinh(2\eta_*)}{\sin^2(s_0 \ln(a/a_*)) + \sinh(\eta_*)} \frac{\hbar\, a^4}{m}, \tag{3.32}$$

where c is a numerical constant, which can be calculated for example with an effective field theory approach [Bra08]. In figure 3.6 we plotted $(K_3)^{1/4}$ with the formula derived above, the scaling factor s_0 was chosen to be 2 instead of 1.00624 in order to increase visibility. The possibility to decay into a deeply bound dimer and a free atom at short hyperradial distances results in a finite lifetime of the Efimov trimers and thus in a finite width of the loss resonance. For $\eta_* \to 0$, the loss resonances becomes arbitrarily narrow and diverge to infinity.

In principle, an infinite number of Efimov resonances should occur if the scattering length tends to $-\infty$. In experiments, however, the number of observable resonances is limited to a few, owing to the unitary limitation of the inelastic process leading to loss. In our formula the S-matrix element which describes the loss process can diverge to infinity. This is unphysical since at a certain magnitude every collision leads to a three-body recombination event and the probability to enter the high-energy atom-dimer state cannot exceed unity. Additionally, for finite temperatures the low-energy limit is also only an approximation, that breaks down if the temperature becomes to high.

In 2004, J. D'Incao et al. were able to show in [D'I04] how these limitations affect experiments. They concluded that temperature effects start to wash-out the resonances as soon as the three-body loss coefficient becomes of the order of the unitary limit. In section 6.3.2 we will analyze these limitations more thoroughly and in the context of our experimental data.

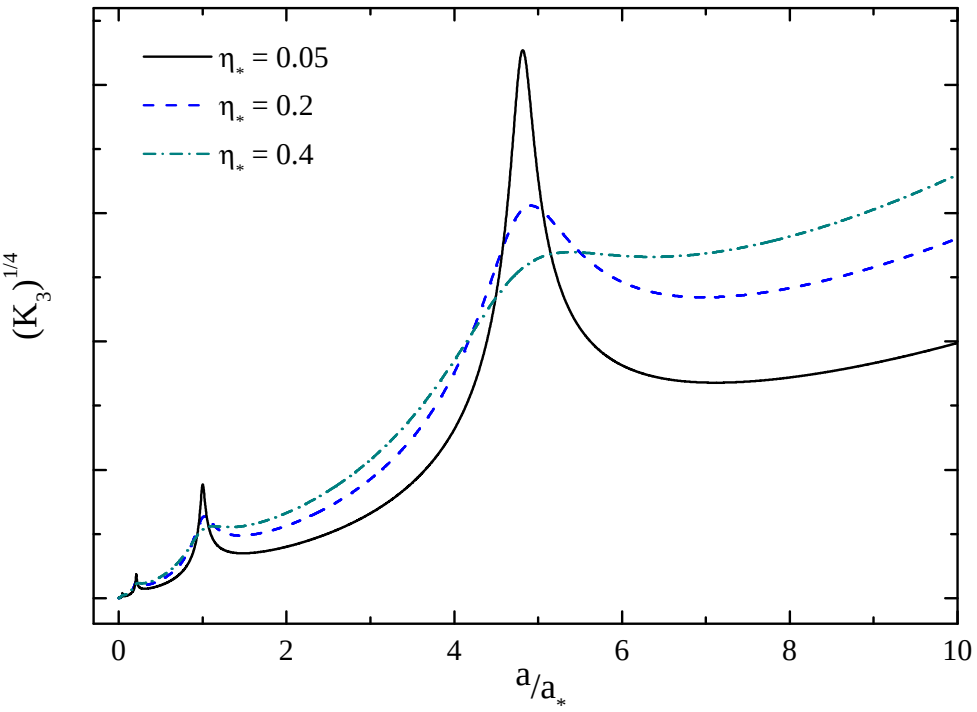

Figure 3.6: Calculated three-body loss coefficient K_3 as a function of $\frac{a}{a_*}$ for different inelasticity parameters η_* (a_* is the position of a loss resonance). The inelasticity parameter describes the finite lifetime of the trimer states and thus leads to a finite width of the loss resonance. One can observe the log-periodic behavior of K_3, which exhibits loss resonances for every scattering length $a = a_* \left(e^{\pi/s_0}\right)^n$. We used $s_0 = 2$ for the plot to increase visibility. In experiments, this behavior is cut-off at small scattering lengths by the range of the interaction potential r_0. For large interactions limitation due to temperature effects and the unitary limit occur (see section 6.3.2).

Chapter 4

The Experimental Setup

The main goal of the experimental apparatus is to enable a fast and efficient production of an ultracold degenerate Fermi gas of ^{6}Li atoms. In a first step a slowed atomic beam is captured and precooled in a magneto-optical trap (MOT). Afterwards the sample is transferred to an optical dipole trap where its temperature is further decreased by evaporative cooling and for sufficient low temperature the quantum degenerate regime can be reached. With these ultracold fermionic samples, experiments can be performed. The preparation and the the experiments are performed in an ultra high vacuum environment (UHV) with pressure on the order of 10^{-12} mbar to ensure sufficient lifetimes for our purposes. The experimental setup has already been extensively discussed and analyzed in several diploma thesis [Ser07, Lom08, Koh08]. Therefore, the aim of this chapter is to provide a brief overview of the setup and focus on the parts that were recently added, like the radio frequency (RF) setup and the high-resolution imaging setup in vertical direction.

4.1 Vacuum Chamber and MOT

Since the last diploma thesis was carried out in our group [Koh08], the vacuum setup (see figure 4.1) was not significantly changed. The UHV is maintained by two ion and two titanium sublimation pumps. One of each located in the oven section. The Zeeman slower tube between the oven section and the main chamber serves as a differential pumping stage. The second ion pump and titanium sublimator are placed right after the experimental chamber (see figure 4.1). To further improve the vacuum at the place of the experiments, the main chamber is coated with a special Non Evaporable Getter (NEG) coating developed at Cern [NEG]. Another special feature of the vacuum setup is the gate valve attached to the main chamber. It enables to add parts in the octagon or to attach for example a glass

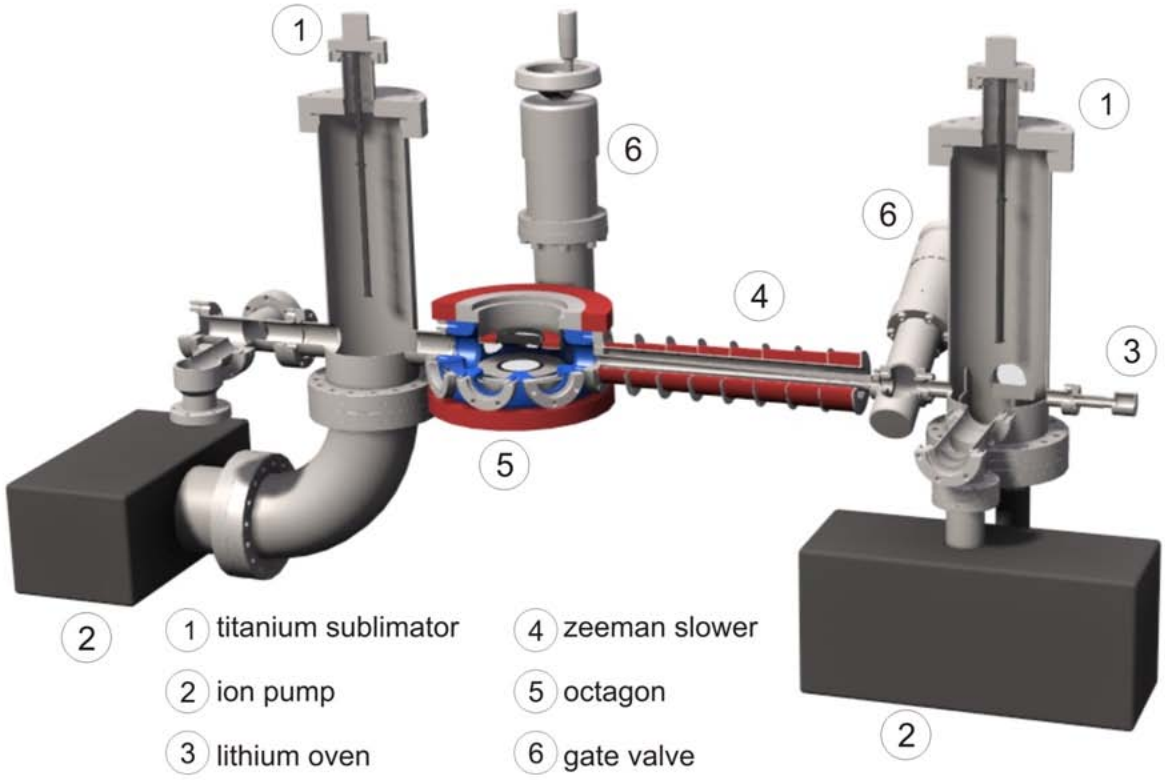

Figure 4.1: Overview of the vacuum chamber with pumps, oven, Zeeman slower and main experimental chamber. The magnetic field coils for the magneto-optical trap, the Feshbach coils and the coils of the Zeeman slower are shown in red. The main experimental chamber (octagon) is displayed in blue.

cell without breaking the vacuum.

The oven is normally operated at a temperature of $360\,^{\circ}\mathrm{C}$, this leads to sufficient atom flux in direction of the main chamber. After leaving the oven section, the atoms in the beam are decelerated in a Zeeman slower and subsequently captured in the MOT inside the main experimental chamber (5 in figure 4.1). For the MOT and the Zeeman slower we use a tapered amplifier system (TA100 from Toptica) with an output power of about 400 mW. The tapered amplifier (TA) is locked by a beat offset lock [Sch99] with respect to the spectroscopy laser (see [Lom08]). The spectroscopy laser is stabilized to the $2^2S_{1/2}\,(F = 3/2) \rightarrow 2^2P_{3/2}\,(F = 5/2)$ line with a Doppler-free saturation spectroscopy [Ser07]. After dividing the TA beam into cooler and repumper, the frequency is adjusted by acousto optical modulators (AOMs).

Both branches are subdivided at several beam splitters, coupled into optical fibers and transferred to the experimental table. After all manipulations and the transfer

to the experimental table, the remaining power in all beams (3 retro reflected MOT beams and one Zeeman slower beam) is about 150 mW. A detailed analysis of the MOT performance and parameters can be found in [Ser07], a complete scheme of the 671 nm laser system in [Lom08].

To monitor the MOT loading efficiency we use a diagnostic sequence and measure the fluorescence of atoms [Ser07] in the trap after a loading time of one second. The atom number in the MOT is not saturated after this time and the values obtained fluctuate from $0.8 \cdot 10^8$ to $1.2 \cdot 10^8$. If the atom number has decreased significantly, the coupling of the seed laser into the TA chip and the coupling into the optical fibers has to be readjusted. This has to be done in rougly 2 to 4 weeks intervals.

4.2 The Dipole Trap

To enter the quantum degenerate regime the phase space density has to become on the order of unity. After the MOT, it is still only about 10^{-5}. The standard technique used to increase phase space density further is evaporative cooling. This technique was developed to cool atomic hydrogen into Bose-Einstein condensation [Hes86]. By letting the hottest atoms of the sample escape from the trap and after rethermalization of the remaining atoms by elastic scattering, the temperature of the trapped atoms can be significantly reduced. This decrease in temperature leads to an increase of the phase space density (if the density remains the same or increases). However, the prize one has to pay is a large loss of atoms during this procedure.

We use an optical dipole trap to create the conservative trapping potential needed to perform evaporative cooling. In a fermionic sample the elastic cross section vanishes for identical particles and ultracold temperatures. Therefore, one either uses different hyperfine states of the same atom or a second species of atoms. Because we did not want to set up a second laser system for another species, we decided to use a mixture of the two lowest Zeeman substates ($|1\rangle$ and $|2\rangle$ defined in section 2.1.2). In an optical dipole trap one can take full advantage of the broad Feshbach resonance at 834 Gauss between states $|1\rangle$ and $|2\rangle$. Here, the elastic scattering rate is resonantly enhanced and hence ensures fast thermalization and thus effective evaporative cooling. For the evaporation procedure, we follow the scheme used by J. Thomas' group at Duke University [O'H99, Gra02] and R. Grimm's group in Innsbruck [Gri07].

These optical dipole traps make use of the fact that the oscillating electric field of a light wave induces an electrical dipole moment on the atom, the induced dipole moment then interacts with the applied oscillating electric field. This leads to an effective potential, which is proportional to the square of the electric field

strength ($\propto E^2$) and thus proportional to the intensity of the light. The sign of the detuning Δ from the atomic transition then decides if the atoms are low or high-intensity seekers. For red detuning, meaning longer wavelengths, the atoms are pushed towards high intensities (for blue detuning towards intensity minima). Since trapping a sample with blue detuned light would require a difficult geometric setup, we use a red detuned optical dipole trap. Here, the atoms are trapped in the intensity maximum. Consequently, the focus of a single red detuned laser beam can already serve as a trap. Heating caused by non-resonant scattering between atoms and photons from the trapping light can be suppressed by choosing a large detuning. However, this makes it necessary to increase the intensity of the trapping beam to achieve a reasonable trap depth. To meet our requirements, we use a single-transverse-mode Ytterbium doped fiber laser with a power of 200 W, manufactured by IPG photonics (IPG YLR-200-SM) for the dipole trap. Its center wavelength is at 1070 nm (width 3 nm), which ensures sufficient large red detuning compared to the atomic transition at 671 nm. One big issue working with such high-power lasers is, as mentioned in [Lom08, Koh08], thermal lensing. If a high-power laser beam is focussed tightly and propagates through an optical element, it deposites energy and heats it. This changes the refractive index of the material locally and results in undefined drifts of foci. In order to avoid this, one has to work with large beam diameters, where possible, remove all optical elements that are not essential or use optical components made of special materials (fused silica lenses or tellur dioxid for the AOM crystals work better than the standard borosilicate glass (BK7)). But even with these changes, we are still not able to use the full laser power of 200 W for a long time if we want to prevent strong thermal lensing effects. Thus, we start to lower the laser power less than 10 ms after the transfer from the MOT and within 100 ms we arrive at half the possible power (for a precise description of the transfer process see [Lom08]). By doing so, we loose far more atoms than necessary in the first 150 ms of evaporation. Only recently we learned that lenses and anti-reflection coatings developed especially for very high power applications are available and we will soon test if they meet our requirements. This could enable us to produce ultracold samples consisting of a larger amount of atoms.

Using a single beam as a trap results in very high aspect ratios (up to 100), which means very elongated cigar-shaped traps. The resulting trapping frequencies in the longitudinal axis are very small, which makes the trap very vulnerable to residual magnetic field gradients or gravitational forces and result in undefined loss of atoms from the trap. To avoid this, we use a crossed beam trap which also results in deeper trapping potentials. In this setup it is crucial to rotate the polarization of the counterpropagating beam by 90 degress in order to guarantee sufficient lifetimes. The explanation for this is still not completely clear but we observe drastic losses if we do not rotate the polarization. Other groups us-

ing the same type of lasers experienced difficulties using large ($\approx 90°$) crossing angles, thus we decided to cross the beams only by an angle of 14°. This also makes it possible to shine both dipole trap beams through one window of the main chamber, which leaves us more optical access for imaging and perhaps, in the future, for an optical lattice. The complete setup of the dipole trap can be found in [Koh08]. The aspect ratio of our trap is about 1/10. At a laser power of 106 mW per beam, the resulting trap frequencies are $\omega_z = 2\pi\, 33(3)$ Hz in the longitudinal and $\omega_x = \omega_y = 2\pi\, 344(15)$ Hz in the axial direction . These values are obtained by parametric heating and by exciting dipole oscillations of the cloud inside the trap, the complete procedure is explained in [Koh08]. The heating rate associated with our dipole trap is only about 1.11 ± 0.12 nK/s at a beam power of 200 mW per beam.

A special feature of our current setup is the use of time-averaged optical potentials. Two crossed AOMs allow to move the dipole trap position in two dimensions. This can be performed much faster than the inverse of the trapping frequencies, therefore the atoms experience a time-averaged potential. It was intended to use this technique to increase the overlap betweeen the dipole trap and the MOT during the transfer. But because we can not use the full beam power for a long time the transfer efficiency could not be increased. This could change if the new high power lenses do not exhibit such strong thermal lensing effects. However, the time-averaged potentials can be and are used to "draw" trapping potentials at lower beam powers, for instance to further decrease density in experiments with three-component Fermi gases.

4.3 The Radio Frequency Setup

An essential tool to change the internal state of the atoms is the use of radio frequency (RF) fields. The three lowest Zeeman sublevels of the electronic ground state of ^{6}Li (see figure 2.1) are spaced by about 50-120 MHz in the magnetic field range of interest. Applying RF pulses with the right frequency drives the addressed hyperfine transition. In our experiments, we need to drive RF transitions at different points in time, during the evaporation to balance the number of atoms in state $|1\rangle$ and $|2\rangle$ and later to produce the three-component sample. The RF signals are generated by different waveform generators, sent through switches, amplified and applied to the atom clouds by an antenna located at the lower reentrant viewport (see figure 4.4). Most of the experimental data discussed in this thesis was generated using the "old" provisional RF setup. But since we had to return borrowed equipment and wanted a more powerful and variable RF system we rebuild most parts of it. A scheme of the "old" and the "new" setup can be found in figure 4.2.

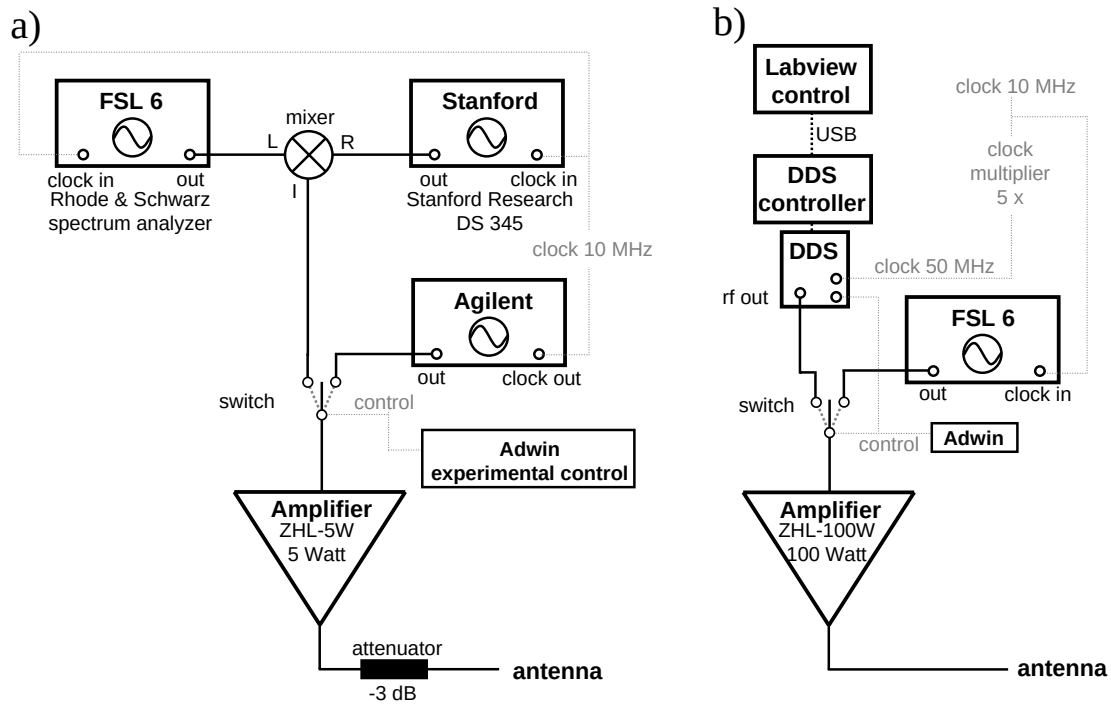

Figure 4.2: Scheme of the "old" (a)) and "new" (b)) radio frequency setup.

"Old" RF setup

The main part of the "old" setup was the spectrum analyzer (FSL 6, Rhode & Schwarz) controllable via our Labview experiment control. It is capable to generate a single frequency at its output with a power of 0 dBm in a frequency range from 0 to 6 GHz. To drive the $|1\rangle - |2\rangle$ and $|2\rangle - |3\rangle$ transitions simultaneously, we mixed the frequency of the spectrum analyzer (roughly 80 MHz) with a 4 MHz signal generated in an arbitrary waveform generator (Stanford DS345). The mixer (ZFM-4-S+, Mini Circuits) creates the sum and difference frequency, each of which is then resonant to one of the transitions ($\approx$76 and $\approx$84 MHz).

During the evaporation we also need a RF pulse to balance the number of atoms in the lowest two hyperfine states, which are loaded from the MOT. This signal is created in another arbitrary waveform generator (Agilent 33250 A, from now on referred to as Agilent AWG). As we need different RF fields at different times, we use a switch (ZX80-DR230-S+, Mini Circuits) to change between both generators and to turn the RF off completely. After passing the switch, the signal is amplified by a 5 Watt Amplifier (ZHL-5W, Mini Circuits). Because the antenna does not dissipate most of the applied RF power, most of it is reflected to the amplifier. But since this amplifier does not tolerate high back reflection, we had to put a 3

dB attenuator before the antenna. This attenuator reduced the incoming power by a factor of 2, but reflections from the antenna have to pass it a second time in reversed direction and thus they are diminished by a factor of 4. Consequently this is too little to damage the amplifier output. In order to synchronize the frequencies of all generators, we connected them to the 10 MHz clock output of the Agilent AWG (see figure 4.2).
The major disadvantages of this setup were:

- The Agilent AWG could not be programmed with the experimental control. Thus, we determined the corresponding transition at the magnetic field of interest with the spectrum analyzer and then programmed the Agilent AWG by hand.

- The old amplifier had only 5 W of power. Thus after the attenuator in front of the antenna the resulting power was only about 2 W. This results in smaller Rabi frequencies which increases the time to drive a transition. This raises problems if the sample decays fast or if decoherence occurs on the same time scale.

- The spectrum analyzer could only generate one frequency per experimental cycle and it was not possible to do frequency ramps.

- The width of the RF transitions in a homogeneous magnetic field is given by the relative slope of the magnetic moments and the magnetic field instabilities. As states $|1\rangle$ and $|2\rangle$ tune almost exactly the same in a magnetic field above 100 Gauss, the width of this transition is quite narrow (0.5 kHz). Hence, small drifts in the magnetic field or the RF setup result in frequency shifts, such that we have to readjust the frequency every day.

The "new" RF setup

To overcome the shortcomings of the "old" setup we implemented a "new" RF setup. The most important part of the "new" setup (see figure 4.2) is a Direct Digital Synthesizer (DDS). This chip (AD9854, Analog Devices) creates sine signals up to 150 MHz and can be digitally programmed using an onboard micro controller (ATmega128-16AC). A program that can assemble whole sequences of RF pulses and ramps is embedded into the Labview experiment control. Before every experimental cycle, the frequencies, pulse lengths, powers (up to 7 dBm) and ramp speeds are programmed on the microcontroller via USB. The microcontroller then sets the DDS chip and waits for the corresponding external triggers produced by the Adwin real-time system. This system has a fundamental advantage, it can generate frequency sweeps and thus does non-adiabatic (Landau-Zener) passages

(see section 5.4.2). Therefore, drifts in the RF setup and the magnetic field do not pose such serious problems anymore. The DDS boards and the front panel were developed in R. Grimm's and R. Blatt's groups in Innsbruck. Currently, we only have one board, but in principle up to 64 could be easily installed. They are adressed by one front panel and each of them can be separately triggered. In addition, every DDS board has two outputs and a frequency doubler in front of each output. In the future we plan to use additional DDS boards to generate the RF signals needed for the AOMs controlling the dipole trap.

Another tool in the current RF setup is a 100 W amplifier (ZHL-100W, Mini Circuits), together with the newly designed RF antenna coils (see next section), the Rabi frequencies are significantly increased. That makes it possible to drive RF transitions faster. We believe that this will enable us to perform RF spectroscopy even at magnetic fields where the sample decays relatively fast. To generate frequencies higher than 150 MHz, for example to drive the $|1\rangle - |6\rangle$ transition, we still need the spectrum analyzer (FSL 6). Therefore, we still have a switch in front of the amplifier (figure 4.2).

RF Antennas

To apply the RF fields to the atoms we need an antenna. The wavelength at frequencies of roughly 80 MHZ is about 4 m. As our antenna is less than 10 cm away from the atoms, all our experiments take place in the near-field regime. Hence, the antenna does not have to send an electromagnetic field. An easy setup is then to use a simple loop of copper wire. In order to increase the intensity at the atom's position, one has to maximize the current through the wire. This is done by matching the antenna to the right frequency. The wire loop has a certain inductance (about 100 nH) and in order to resonantly enhance it, one has to connect a capacitor in series with the loop, the capacities needed are on the order of 100 pF. To endure the currents and voltages, we use CKBX05 ceramic moulded multilayer capacitors (they tolerate up to 200 V).

In order to further increase the power transfer to the antenna, the impedance of the antenna has to be matched to the $50\,\Omega$ impedance of the amplifier output. To calculate the magnitude of capacitors and inductors needed, we make use of a computer program called rfsim99 [rfs]. We use a simple L section consisting of one capacitor and one inductor to match the impedance. As the ohmic resistance of the wire loop is extremely small, it is not possible to perfectly match the $50\,\Omega$ of the amplifier output. One could therefore increase the number of windings of the loop, but this would lead to problems matching the LC loop frequency. Because of the errors and simplifications made, the calculated values are only rough estimates. Small stray inductances as for example the connectors of the capacitors can already change the behavior when they are bent or touched. Therefore,

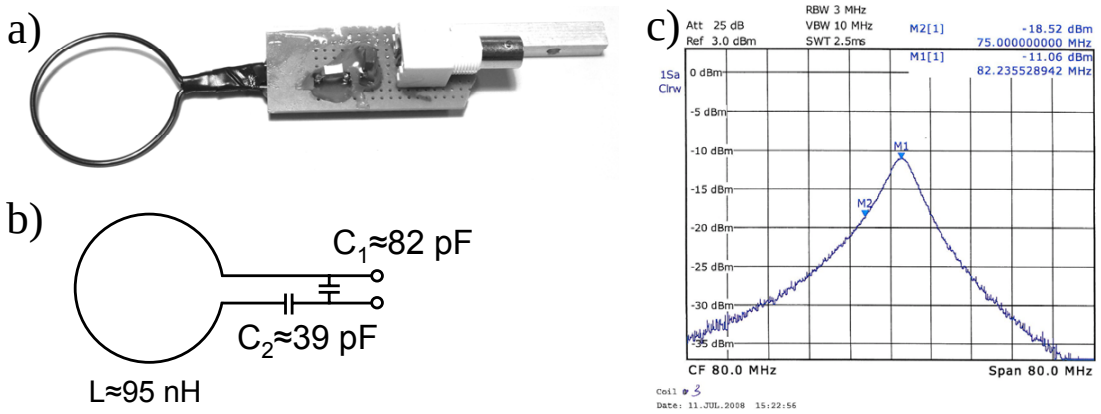

Figure 4.3: a) Picture of the antenna matched for 82 MHz; b) circuit diagram of the antenna; c) resonance characteristics of the 82 MHz antenna, measured with a pick up coil at a distance of 18 mm.

we used a socket and tried different capacitors until the result was suitable for our purposes. Afterwards these capacitors were soldered in and fixed with hot glue. The achievable bandwidth of such an antenna is rather narrow (several MHz, see figure 4.3 c)), therefore we designed antennas matched for different radio frequencies (53, 72 and 82 MHz) and built a mount that made it possible to easily exchange the antennas. A circuit diagram and a picture of one antenna can be seen in figure 4.3. With the LC oscillator and the impedance matched, the currents in the antennas are quite high and if the amplifier is operating at full power, the capacitor starts to disintegrate and the copper wire becomes hot (>80 °C). In order to prevent damage to the antenna, the input power of the amplifier has to be limited to -15 dBm if the frequency is right on the antennas resonance. If it is far detuned, the full power of the amplifier can be used.

The antennas are placed directly below the lower reentrant viewport under an angle of about 45°. The size of the loop was chosen such that it fits around the vertical MOT and imaging beam (see figure 4.4).

4.4 Imaging System

The fundamental tool to investigate our sample is absorption imaging. A resonant laser pulse is applied to the atoms and their shadow is recorded on a CCD camera. This shadow is the two dimensional projection of the three dimensional density distribution of the cloud. Together with a reference image (laser light on, but no atoms) and a background image (all laser beams off), the two dimensional optical

density of the cloud $\rho_{op}(x, y)$ can be calculated:

$$\rho_{op}(x, y) = -ln \frac{I_{abs}(x, y) - I_{background}(x, y)}{I_{reference}(x, y) - I_{background}(x, y)}. \tag{4.1}$$

Given the absorption cross section $\sigma = \frac{3\,\lambda^2}{4\,\pi}$, the two dimensional column density can be determined to be $n(x, y) = \rho_{op}(x, y)/\sigma$. Additionally, one has to take saturation effects into account, but they are negligable for the relatively small intensities in the horizontal imaging setup, which was used for almost all experiments described in this thesis. To decrease noise and facilitate the fitting procedure, the data is integrated along one axis and the resulting one dimensional density distribution is fitted. From this, one can deduce the number of atoms, the temperature and the density distribution (e.g. Gaussian, Bose-Einstein or Fermi distribution), if the laser pulse is sufficiently short to not distort the spatial information of the cloud while imaging (in our case 1-10 μs pulses).

The statistical fluctuations that occur, if N photons are detected is $\sqrt{N}$ because of the Poissonian distribution of the photons. This is called shot noise. To ensure a reasonable signal to noise ratio, one has to additionally guarantee that the optical density is on the order of one. Because if the cloud becomes too dense or too thin, the signal gets lost in the shot noise.

We are currently working with two CCD cameras in our setup: the "Andor" (Andor iXon DV 887 DC) and the "Guppy" (AVT Guppy F-038 B/NIR), a scheme of the imaging setup can be seen in figure 4.4.

4.4.1 Imaging in Horizontal Direction

Most experiments performed in this thesis and before were analyzed with the horizontal imaging setup and using the "Guppy". Therefore, its setup and properties were already described in [Lom08, Koh08]. This comparably cheap camera, is very easy to control, handle and maintain. Thus it is the right choice for purposes, that do not necessary require a very high sensitivity. The interlaced CCD chip of the "Guppy" has 768×494 pixels but we normally bin two pixels in vertical direction, which results in 768×247 pixels with a effective size of $8.4\,\mu m \times 19.6\,\mu m$. The objective of this camera consists of two 1" diameter lenses ($f_1 = f_2 = 150\,mm$) and the resulting magnification is $M = 1.17$. The resolution is determined by the pixel size, so roughly $20\,\mu m$. This is not enough to resolve the transverse axis of the dipole trap in-situ. Therefore, all images have to be made after a time-of-flight.

The different Zeeman sublevels can be separately imaged because the width of the transitions is about 5 MHz, which is narrow compared to the 50 - 130 MHz splitting between adjacent hyperfine states. With our current imaging setup, we

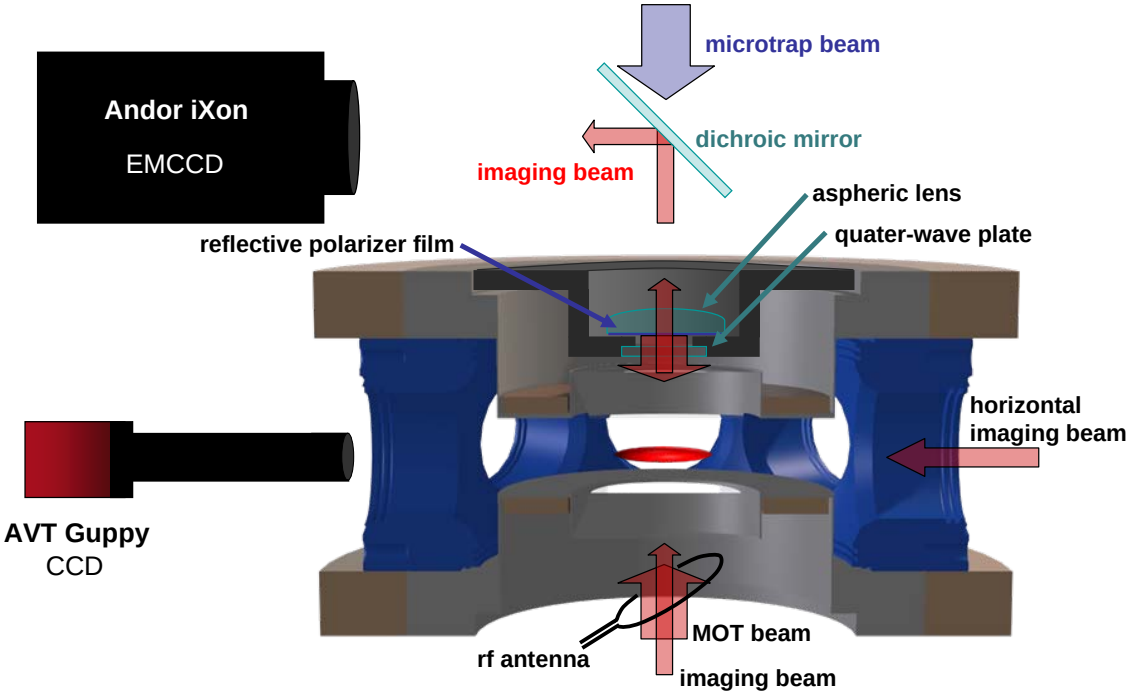

Figure 4.4: Schematic cut through the main chamber, with the horizontal imaging, the high-resolution imaging in the vertical axes, the vertical MOT beams and the microtrap.

are not able to take several images at the same time. Therefore, we have to generate a new sample everytime we want to image a different state.

In experiments we fit the one dimensional density distribution with a Gaussian distribution on the fly, after letting the atoms freely expand for the time of flight. This is a good approximation down to about $T/T_F = 0.35$. For more degenerate samples a more sophisticated analysis with the Fermi distribution has to be performed (see section 2.2), but since this takes more time, we perform it mostly after the measurements to precisely determine the temperature and still use the Gauss fit as an on the fly indicator.

4.4.2 High Resolution Imaging in the Vertical Direction

The second camera setup was implemented during this thesis. It was designed to make high resolution images of the cloud in the vertical direction. The large upper reentrant viewport allows the use of an aspheric lens with large numerical aperture, which makes it possible to reach high spatial resolution. Additionally, the camera has an extremely sensitive electron multiplying CCD chip, which enables

it to count single photons.

This setup allows us to study the atoms inside the trap (in situ). It enables investigation of possible phase separation or of the system's dynamics, e.g. collective excitations. In this setup, the vertical MOT beam and the imaging beam are in the same vertical axis. Additionally, we plan to add a small volume optical dipole trap, the so-called "microtrap", which is also applied in the vertical direction (see figure 4.4). Therefore, one wants an asphere that is specially optimized to tightly focus the microtrap and at the same time allows high resolution imaging. As a first test, we are now using a standard asphere which leads to a microtrap waist of 3.1 μm and an imaging resolution of approximately 3 μm.

In order to retroreflect the MOT beam and to transmit the imaging beam, we use a special reflective polarizer film. This adhesive film is originally used in LCD monitors to enhance the brightness of the screen by retroreflecting one linear polarization and transmitting the perpendicular one. In our case, the imaging beam and the vertical MOT beam are merged with orthogonal linear polarizations and then they pass a quater-wave plate and provide σ^+ and σ^- light, respectively. After passing the atoms, both beams propagate again through a quater-wave plate and one ends up with two perpendicular linearly polarized beams. The film can be adjusted in such way, that the vertical MOT beam is reflected and the imaging beam transmitted. The polarizing film is laminated directly onto the asperic lens, which simplifies the optical setup significantly. After the polarizer film the imaging beam is focussed by the asphere and reflected from a mirror onto the CCD chip of the Andor. This mirror is dichroic and transmits the microtrap light with its wavelength of 1070 nm. All optical elements (lens with polarizer film and the quarter-wave plate) are supported by a specially designed lens holder, which is located right above the upper reentrant viewport and mounted on the main chamber (see figure 4.4).

The first absorption images taken with this setup showed quite strong periodic modulations (fringes). This would not be a problem if those fringes were fixed in position and amplitude, because they would be the same on the reference image and therefore cancel. But if the fringes moved between the absorption and the reference image or if the modulation was too strong (leads to large shot noise), they would remain visible. To overcome this, we made two major modifications. First, we used a special imaging procedure, called frame transfer, which minimizes the time between the absorption and reference picture. Here a part of the CCD chip is covered which enables to take various pictures (absorption image, reference image and the background) and store them under the covered part of the chip before reading out the whole chip at once. Between each picture a clock voltage is applied, which shifts the charges of a pixel in the vertical direction. With the available shift speeds of about $3.3\,\mu$s/pixelshift, the images consisting of 256 lines can be transferred in roughly 1 ms (without frame transfer: $400-500\,ms$ between

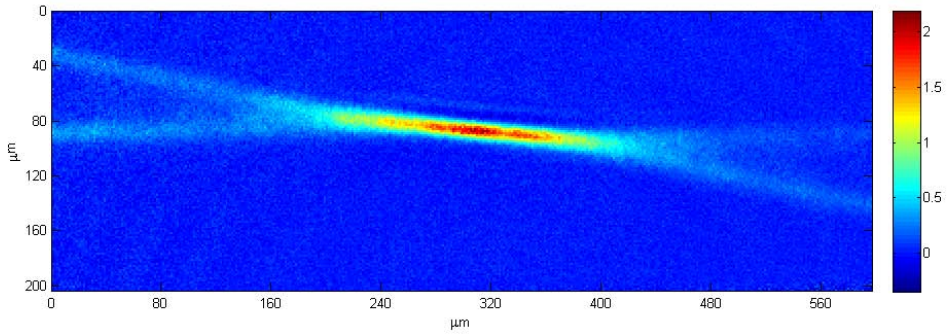

Figure 4.5: Image of the atomic cloud in the trap. Shown is the optical density of an atomic sample. After evaporation the power of the trapping beam is increased again, this leads to a comparatively small and dense cloud and a good visibility of the two trapping beams.

images). By using this technique, the quality of the pictures is significantly improved, especially in the region of low and medium atom densities, because the fringes did not move or change on that ms timescale and therefore cancel. In the region of high density, however, the modulations were still visible, which was due to the little power in the vertical imaging beam. In the beginning, the imaging and MOT beam came out of one optical fiber, therefore the size of the imaging beam was rather large ($\approx 2\,$cm diameter), which resulted in low intensities at the atomic cloud. To provide more light the setup was changed such that the beams are now coming out of two different fibers and are only merged right before the main chamber at a polarizing beam splitter. Hence, the size of the beams can be adjusted independently and the imaging beam now only has a diameter of about 2 mm. Effectively, this increases the intensity at the atom's position which leads to a better image with less fringes. An in situ image of the cloud can bee seen in figure 4.5.

This camera is far more sensitive than the Guppy used in the horizontal imaging system. The price one has to pay for this, is the complexity of the computer control of the Andor. Especially the frame transfer mode is difficult to use and the computer control is still not totally stable.

4.5 Future Plans

There are several modifications of the setup planned for the future:

- The next step, performed presumably in January and February of 2009, will be the implementation of the microtrap setup. This small volume trap, with

high trapping frequencies will be an important tool for the production of finite fermionic samples planned in our experiment. The first preliminary setup was already assembled and tested and will soon be added to the setup. These experiments are carried out by G. Zuern and for more information, we therefore refer to his diploma thesis, which is expected to be finished in April 2009 [Zue09].

- The resolution in the horizontal axis should be improved. For this we already purchased a camera (Stingray F033B, AVT), which is still easy to use but has better specifications concerning pixel size, full well depth and sensitivity than the Guppy. The plan is to build a setup similar to the vertical imaging only along the horizontal MOT beam. The difficulty here is that the distance from the atoms is larger and the size of the window is smaller, which will result in a reduced resolution. To reduce aberrations and still achieve resonable resolutions, we are working with a 2" Gradium (Gradient index) lens. The setup and the camera were already tested and the resolution is about 3μm.

- As pointed out in [Lom08, Koh08] the Feshbach coils remain a problem. The temperature at 200 A is still higher than 80° even with an improved heatsink adhesive. To know which adhesive achieves the best thermal contact, a test setup was built. In a few weeks the first results will be available and another generation of coils will be built. Then the new adhesive will be used and the electrical contact will be soldered with Indium. This simplifies the procedure to attach the connectors since the temperature needed to solder Indium is lower and thus damage of the adhesive is prevented. Furthermore, the size of the connectors was doubled, which reduces the current per area and thus the temperature near the connectors.

- In the next few months we also want to install a second imaging setup in the horizontal direction. This would then be in the direction of the dipole trap and the second horizontal MOT beam. This is a prerequisite to see vortices in the atomic cloud. For this we would also use a Stingray and the setup would be a copy of the other horizontal imaging setup. In order to provide enough laser light for all these imaging beams and to be able to image several spin states at the same time, we ordered another 671 nm diode laser from Toptica (DL 100, with 35mW). The laser has just arrived and has to be integrated in the optical setup and locked with respect to the spectroscopy laser in the next weeks.

- As noted earlier, the standard asphere in the vertical imaging axis is planned to be replaced by a specially designed one. By doing that, the quality of the

imaging and more important the confinement inside the microtrap could be improved.

- We are also thoroughly investigating the possibility to add an optical lattice to our setup. Especially for the three-component experiments that would give us a tool to explore SU(3) Hubbard models, for which interesting new phenomena are predicted [Aza08, Wil07, Rap07, Rap08].

Chapter 5

Creation of a Three-Component Fermi Mixture

This chapter deals with the preparation of a three-component Fermi gas consisting of the three lowest Zeeman substates of ^{6}Li ($|1\rangle$, $|2\rangle$ and $|3\rangle$ in figure 2.1). Before we explain the creation procedure of a three-state mixture in detail, we briefly show how we can achieve Bose-Einstein condensation by evaporatively cooling a two-component sample. For large positive scattering lengths bosonic molecules can be formed at sufficiently cold temperatures and these are able to Bose condense.

We then change to the three-component case and first present our motivation producing such a sample. During the production process, several difficulties arose, especially strong losses. To avoid those, the standard evaporation scheme had to be changed such that molecules formation is inhibited. Section 5.3 illustrates how we resolve these problems and we continue with the production sequence used to produce a three-component sample. Finally in the sections 5.4.2 and 5.5 radio frequency (RF) transitions in ultracold fermions and the thermometry will be discussed in detail.

5.1 Evaporation, Molecule Formation and Molecular BEC

A Fermi gas consisting of identical particles cannot be evaporatively cooled into degeneracy, because the s-wave cross section vanishes for low temperatures (see section 2.1.1). Thus one uses either a mixture of bosons and fermions, where the bosons sympathetically cool the fermions, or two-component Fermi gases. These components can be, for instance, different Zeeman substates of the same atom. In the following we will explain the evaporation scheme for such a two-state mixture

and show how bosonic molecules are formed at sufficiently low temperatures. These molecules can then condense into a molecular Bose-Einstein condensate (mBEC). Furthermore we explain how we are able to observe this phase transition.

The evaporation scheme starts with the transfer of atoms from the MOT to the dipole trap. During the transfer, we optically pump all atoms into the states $|1\rangle$ and $|2\rangle$ and then we evaporate a two-component mixture consisting of these states. Since we cannot perform plain evaporation due to thermal lensing effects, we have to immediately start forced evaporation (see section 4.2). To ensure high thermalization rates and effective evaporation we tune the magnetic field to roughly 750 Gauss where the scattering length (a_{12}) is about $3500\,a_0$ (with a_0 being Bohr's radius, see appendix 7.1).

In the first part of the evaporation, the laser power is lowered to about 40 W in two linear ramps that have been optimized independently. Afterwards, the power is further reduced by varying the radio frequency power in two acousto-optical modulators (AOMs), the second AOM is rotated by 90°with respect to the first one (originally done to enable the creation of time-averaged potential, for more information see [Koh08]). This is normally done in three to four linear ramps. During this "AOM evaporation", the power in the dipole beam is monitored by two photodiodes, one for high intensities and one for lower ones. The signals obtained at the diodes are fed into the 100 kHz digital PID loop embedded in our experiment control and the feedback signal is returned to the AOMs to stabilize and regulate the power of the dipole trap beam.

A large positive scattering length is always associated with a universal bound state right below the continuum [Lan81]. Thus at a magnetic field of 750 Gauss, the binding energy of this dimer state is about $E_b = k_b\, 2.3\mu K$, where k_B is Boltzmann's constant. If the temperature of the sample gets comparable to the binding energy divided by k_B, the molecular state is getting populated by three-body recombination. D. Petrov showed that these "good" three-body processes happen quite often near a Feshbach resonance, thus ensuring sufficiently fast molecule formation. On the other hand, the "bad" three-body processes, leading to molecular relaxation and thus loss from the trap, are strongly suppressed for large scattering lengths [Pet04, Pet05], which leads to long lifetimes of the weakly bound molecules. This was experimentally confirmed by the Innsbruck group in [Joc03a]. A chemical equilibrium between molecules and atoms, which depends on the temperature is established [Chi04b]. This equilibrium tends towards more molecules for temperatures small compared to the binding energy divided by k_B and can be verified by radio frequency spectroscopy [Bar05]. A thorough examination of the atom and molecule number for different temperatures can be found in [Koh08].

If evaporation is continued a molecular Bose-Einstein condensate (mBEC) emerges. In our case the critical temperature is of the order of 100 nK and the number of

molecules is about 1.5×10^5. This phase transition can be shown by the observation of a bimodal density distribution after a time-of-flight. In a BEC, the ground state of the trap is macroscopically occupied, which leads to an inverse parabola density distribution (called Thomas-Fermi (TF) distribution) in the center, while the wings are still thermal and can be fitted by a Gaussian. Such a bimodal distribution of the density can be seen in figure 5.1. The TF distribution can be easily deduced from the Gross-Pitaevskii equation in the Thomas-Fermi limit, which neglects the kinetic term, because it is small compared to the interaction energy.

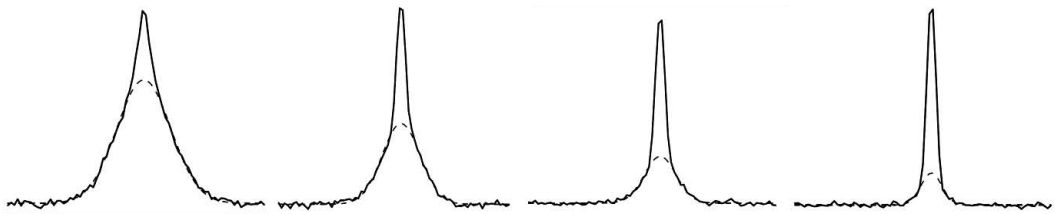

Figure 5.1: Emergence of a Bose-Einstein condensate of molecules. Shown is the integrated column density of atoms for different stages of evaporation. For larger temperatures, only a small condensate fraction is visible (left image). For colder temperatures, the condensate fraction increases until we see an almost pure mBEC (right image). The dashed line is a Gaussian fit to the wings of the BEC, the solid line is the signal obtained by absorption imaging and subsequent integration in one axis.

Compared to atomic BECs, it is more difficult to observe the bimodal distribution in a molecular BEC consisting of fermionic atoms. The reason for this is that we have to work with strongly interacting samples to ensure sufficiently stable molecules (^{6}Li : $a = 3500\,a_0$); this is not the case for bosonic atoms, where the interactions are comparatively small (^{87}Rb: $a = 100\,a_0$). The Thomas-Fermi distribution obtained from the Gross-Pitaevskii equation in the TF limit is:

$$n(\vec{r}) = \frac{\mu - V_{ext}(\vec{r})}{g} \propto r^2/g, \tag{5.1}$$

where $n(\vec{r})$ is the density, μ the chemical potential, $V_{ext}(\vec{r}) \propto r^2$ is the external trapping potenial and $g = 4\pi\hbar^2 a/m$ is the coupling strength. This shows that the larger the interaction strength, the wider the resulting Thomas Fermi distribution and therefore it is almost impossible to visualize the bimodal distribution in our case. This problem can be solved by ramping the magnetic field to smaller values ($\approx 650\,$G). There, the interactions are weaker and thus the TF profile becomes narrower and as a result easier to observe[1]. Another problem with imaging mBECs

[1]In reality, the situation is more difficult since we ramp the magnetic field so fast that we

is that as soon as the molecules become more strongly bound, they cannot be observed because the binding energy alters their optical transition frequency. To avoid this, one ramps the magnetic field very close to the resonance immediately before imaging the cloud. Here, the binding energy is so weak that the frequency shift is negligible. To observe clear bimodal distributions as shown in figure 5.1, one has to combine these two techniques: first one ramps the magnetic field to a lower value to decrease interaction and then during the time-of-flight one ramps back to the resonance to be able to observe the molecules. The images in figure 5.1 were produced using those techniques.

5.2 Motivation and Theoretical Predictions for Three-Component Fermi Gases

In section 5.1, we showed how molecular Bose-Einstein condensation occurs those two-component Fermi gases. Due to their stability and the possibility to change the interactions by means of Feshbach resonances, these two-component samples were the standard system to explore fermionic superfluidity and the BEC-BCS crossover [Zwi05, Bar04, Reg04, Bou04].

Surprisingly, a third state was, up to now, only used to probe the two-component sample, for example as a final state when performing radio frequency (RF) spectroscopy [Gup03, Bar05, Chi04a] or as a non-degenerate temperature probe [Reg05] (see also section 5.5). Theorists however discovered that interesting physics occurs inside a three-component sample years ago.

A sample of three distinguishable fermions has a totally different symmetry compared to the SU(2) symmetry of the two-component sample. The system resembles the three different colors of quantum chromodynamics (QCD) and has a SU(3) symmetry, but with the advantage that they are easier to produce, observe and understand than quarks in a baryon or in a quark-gluon plasma (QGP). Or as the Nobel laureate F. Wilczek puts it in his article 'Quantum chromodynamics: Lifestyles of the small and simple' [Wil07]:

> "Ultracold atoms in optical lattices are already used to simulate complex solid-state phenomena. But could the same platform also give us a better grasp of how quarks group together?"

There were quite remarkable efforts made in the past few years concerning the theoretical description of such a three-component Fermi gas. Some theoretical studies have investigated the stability of multi-component Fermi gases [Blu08,

create a non-equilibrium state. This actually further improves the visibility of the TF profile after a time-of-flight.

Hei01], others have studied how pairing occurs in such a system [Paa06] or if there is superfluidity in a three-component sample [Che07, Zha07, Bed06]. Other questions that arise are e.g.:

- Is the ground state a three-body bound state (trimer or trion) [Flo08, Rap07, Bri04] and does the system break its symmetry to form two-body bound states (dimers) at certain interaction strengths?
- Are the three-body bound states Efimov-like and is Efimov physics applicable to fermionic samples [Bra06]?
- How does BCS pairing look like in such a system [Hon04]?
- Do the different phases separate in a trap and build up shell structures [Paa07]?
- And what happens if the whole system is loaded inside a three or one dimensional optical lattice [Rap08, Luu07, Aza08]?

Various theoretical approaches and models, such as functional renormalization group, density matrix renormalization group (DMRG), other variational methods, Hubbard models, BCS theory, Efimov physics and many more were used to develop these predictions.

This vast amount of theoretical work clearly shows the relevance and impact of such a three-component Fermi system not only for the ultracold gases community. Therefore, stimulated and inspired by discussions with several theoreticians, our group attempted to produce a balanced three-component Fermi gas soon after the first realization of a molecular BEC in our experimental apparatus in January 2008.

5.3 Roadblocks

In the RF spectroscopy experiments performed with strongly interacting samples (e.g. [Chi04a]), it was impossible to observe atoms in the final/third state. This shows, that at least close to the resonances, the lifetime of a three-component sample is rather short. Later, it was measured in [Sch08b] to be of the order of 30 ms (on the $|1\rangle - |3\rangle$ resonance at 691 Gauss).

This means that the fast inelastic loss on resonance prevents the production of a three-component sample in equilibrium, since the sample already starts decaying while being produced [2]. As the three-body loss rate K_3 scales strongly with the in-

[2]The achievable Rabi frequency to populate the third state by RF is on the order of a few kHz. This leads to timescales of several ms to incoherently balance the three-component sample.

teraction strength (see section 3.3), one would try to produce the three-component sample at weaker interactions.

In section 2.1.3, we noticed that due to the large negative background scattering lengths of ^{6}Li no zero crossings of the scattering lengths (a_{12}, a_{13} and a_{23}) occur on the BCS side of the resonances (see figure 2.3). Thus to obtain a weakly interacting system, one has to access the magnetic field region between 530 Gauss and 560 Gauss. This is on the BEC side of the resonance, which means that there is a bound state near the continuum. D. Petrov and coworkers [Pet04, Pet05] pointed out that the dimers, formed out of two fermions, are stable near the Feshbach resonance, but they become unstable if the binding energy becomes too large. This is explainable by the fact that near the resonance, the fermions in the bosonic dimer are so weakly bound that they still exhibit fermionic behavior, thus suppressing three-body events by Pauli blocking (figure 5.2 a)). If the dimers become more deeply bound, they behave more and more like bosons (figure 5.2 b)) and thus the molecule can scatter inelastically with other dimers or atoms. This leads to relaxation into a deeper bound molecular state. Through this process, the dimers gain additional kinetic energy and are immediately lost from the trap. Therefore it is impossible to cool the two-component sample ($|1\rangle$ and $|2\rangle$) to low temperature near the Feshbach resonance, where evaporation is effective, and then ramp the magnetic field to the zero crossings in order to create a three-state mixture. During that ramp the molecular state would always be populated and this would lead to a relatively fast decay at magnetic fields of about 700 Gauss.

For a three-component sample, this so-called "three-body recombination" can occur no matter if the molecules are tightly bound, weakly bound or not bound at all. In contrast to the two-component case the third particle is not Pauli blocked (see figure 5.2 c)) and thus the three-body recombination process can take place when three atoms (one of each state) approach each other. It is then possible that two of the atoms form a deeply bound dimer and the third particle carries away the additional momentum. The binding energy released in such a process is so large that all particles involved gain enough kinetic energy to immediately leave the trap. We will later see that this is the process responsible for the strongly varying stability of a three-component Fermi gas.

To avoid the just mentioned problems, the evaporation scheme has to be changed. In the following section 5.4 we will explain the new evaporation scheme in detail and thus show how we can accomplish the production of a three-component mixture in equilibrium.

Another major difficulty is the production of the three-state sample by RF fields. As mentioned in chapter 4, the widths of the respective RF transitions (caused by the relative slope of the magnetic fields) are so narrow that even the slightest change in the magnetic field or the frequency calibration already inhibits driving the respective hyperfine transition (on the other hand the same effect enables us

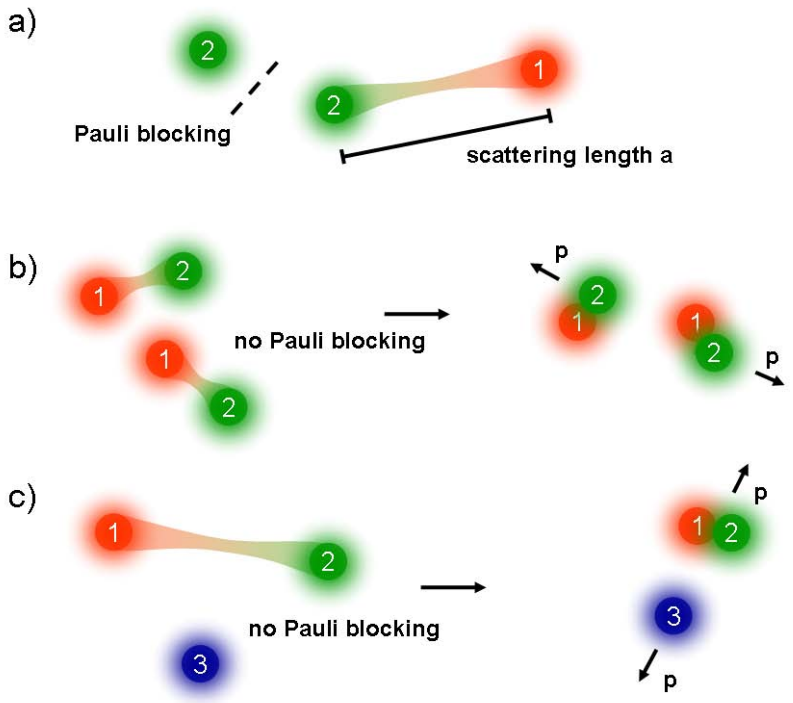

Figure 5.2:
a) In a two-component mixture Pauli blocking leads to relatively stable molecules if the scattering length is quite large, i.e. near the Feshbach resonance [Pet04].
b) If the molecules are more tightly bound, they exhibit bosonic behavior and are not Pauli blocked, this can lead to relaxation after scattering with dimers or atoms.
c) For three distinguishable fermions, the third spin state is also not Pauli blocked (no matter if the molecule is weakly or stronger bound) and therefore the molecule can relax into a deeper bound state. The released binding energy is converted into kinetic energy, which is so large that atom and dimer immediately leave the trap.

to do very precise RF spectroscopy). This problem could be significantly reduced by changing the RF setup and performing Landau-Zener passages [Lan32, Zen32] (see section 5.4.2).

5.4 Production of a Three-Component Sample

We will now proceed to the production of a three-component Fermi gas. The 'standard' evaporation scheme used in previous experiments to achieve molecular Bose-Einstein condensation, unitary interacting Fermi gases and fermionic superfluidity with two-component samples, is not applicable for this case. Thus we had to develop a new evaporation scheme, which meets our requirements to access the

region of weak interactions. In this region, we are able to populate the third state by applying radio frequency fields and thus can realize a three-component Fermi gas in equilibrium. Through this new approach we are able to access the rich physics occuring in a ternary fermionic mixture by preparing the sample where the gas is relatively stable. During the experiments, however, we can change the magnetic field to access strongly attractive or repulsive interactions between all three states of the Fermi gas.

5.4.1 Production Sequence

All our sequences start with a MOT loading phase of about three seconds. Subsequently the two-component sample is transferred into the dipole trap, where evaporation is commenced at 750 Gauss. In contrast to the production of a mBEC, molecules are not desired for the production of a three-component sample. As already mentioned, they would decay if one tries to access the region of weak interactions near the zero-crossings of all scattering lengths. It is also not an option to populate the third state in regions where the scattering lengths are large in amplitude, because the three-body loss scales with $\sim a^4$. This inhibits the formation of a sample in equilibrium, because it would decay during its production. We therefore have to stop the evaporation of the two-component mixture near the Feshbach resonance (750 Gauss, 1. in figure 5.3) before any molecules are formed. This means that we stop evaporation at temperatures significantly higher than the binding energy divided by Boltzmann's constant: the binding energy is $E_b = k_B \times 3.4\,\mu K$ in our case, hence we stop evaporation at about $10\,\mu K$.

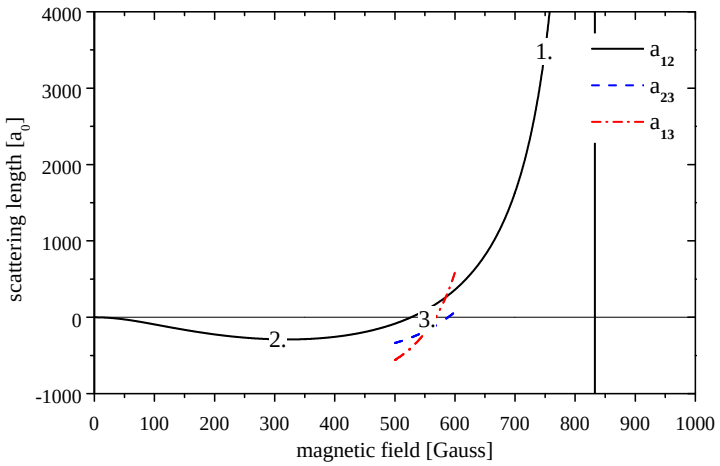

Figure 5.3: Scattering lengths in Bohr radii for the two-body interactions as a function of the magnetic field. Shown are the different regions of evaporation and production of the three-component mixture (for more information see text).

In order to access the region of small scattering lengths, we then ramp the magnetic field to 300 Gauss (point 2. in figure 5.3). Here, the scattering length in our $|1\rangle - |2\rangle$ mixture (a_{12}) is about $-290\,a_0$, with a_0 being Bohr's radius. For negative scattering lengths there is no two-body bound state right below the continuum; thus we can continue evaporation into degeneracy without forming molecules. As the scattering length is about an order of magnitude smaller than at 750 Gauss, the thermalization rates are not as high and consequently evaporation needs more time and is not as effective. Nevertheless, we can reach temperatures down to about 130 nK and roughly 7.5×10^4 atoms in each spin state ($|1\rangle$ and $|2\rangle$). This corresponds to $T/T_F \approx 0.28$, which means that the quantum degenerate regime is reachable. We then adiabatically increase the power in the dipole trap beam by about a factor of two which leads to an increase of the temperature, but does not change T/T_F. This is necessary to guarantee that all atoms stay in the trap and are not evaporated further due to, for instance, magnetic field gradients while ramping the field. As in the 'standard' evaporation scheme explained in section 5.1, we perform our evaporation in several $(4-6)$ linear ramps that are independently optimized. The only difference is that we change the magnetic field to 300 Gauss after two of the linear ramps.

Subsequently, after finishing evaporation, we ramp the magnetic field to the region of the zero-crossings in all three scattering lengths (3. in figure 5.3), where we create the three-state mixture by RF fields. At 560 Gauss, the scattering lengths are $a_{12} = 118\,a_0$, $a_{13} = -98\,a_0$ and $a_{23} = -143\,a_0$, which is small enough to lead to long lifetimes of the three-component mixture (~ 30 seconds), but still ensures decoherence due to residual magnetic fields, together with small but non-zero interactions. The following sections will describe those RF transitions in more detail.

The three-component samples produced in such way have a temperature of about 215 nK at $T/T_F \approx 0.37$ with about 50 000 atoms per state. We do not observe significant heating by driving the radio frequency transitions, but as E_F scales with the number of atoms ($\propto N^{1/3}$), we effectively increase T/T_F by 'distributing' the two-component mixture on three-components. This degenerate three-component mixture is then the starting point for all experiments. For instance, we can jump to different magnetic fields, observe the remaining fraction after a certain time and thus investigate the three-body loss as a function of the interaction strength (see Chapter 6).

For absorption imaging, we ramp back to 560 Gauss, where we can image one Zeeman sublevel per experimental cycle by absorption imaging. Compared to the time the sample stays at the magnetic field of interest (50-5000 ms), the time we need to ramp the field is rather short (about 1 ms). Since the sample is stable at 560 Gauss (lifetime ≈ 30 s) the loss occuring during the ramps and at 560 Gauss can be neglected if we work in the magnetic field region below 600 Gauss.

5.4.2 RF Transitions in Ultracold Fermions

Driving radio frequency transitions is, as mentioned before, our fundamental tool to change the internal state of atoms. In order to better understand the method, this section will focus on the RF coupling between different Zeeman substates in a homogeneous magnetic field.

Driving transitions

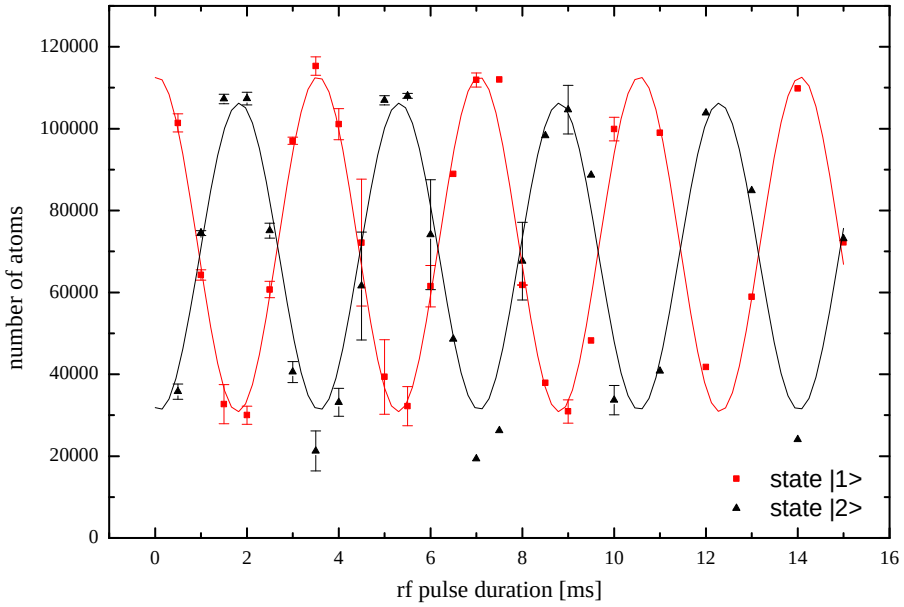

Figure 5.4: Rabi oscillations between states $|1\rangle$ and $|2\rangle$. The fit to the data is a squared sine; the deduced Rabi-frequency is about $\Omega = 1.794\,\mathrm{kHz}$.

Electromagnetic coupling between hyperfine states can be described in the framework of a two-level system and dressed states (see e.g. [Dal85]). The coherent coupling leads to a non-zero probability to change from one state to another if the frequency applied is on resonance with the energy between the respective states. We are working in the strong field Paschen-Back regime, where the nuclear spin and electron spin are decoupled. The electromagnetic coupling between the respective hyperfine states can be described by a magnetic dipole transition Hamiltonian $\hat{H} \propto \hat{S}_x B_0 \, cos(w_{rf}\, t)$. Using this as a periodic perturbation, one can deduce the transition probability as a function of the pulse duration t:

$$P_{ex} \propto sin^2 \left(\frac{\Omega_R \, t}{2} \right), \tag{5.2}$$

where P_{ex} is the probabibility to be in the excited state and Ω_R is the Rabi frequency. The probability shows the well-known Rabi oscillations of a two-level system as deduced for example in [Met99] for an electric dipole transition. An example for this behavior can be seen in figure 5.4. Here, an imbalanced sample of atoms in state $|1\rangle$ and $|2\rangle$ is being exposed to a RF pulse of different durations. The number of atoms in each state oscillates sinusoidally in opposite phase, which shows the coherent coupling between the Zeeman sublevels ($|1\rangle$ and $|2\rangle$).

Landau-Zener passages

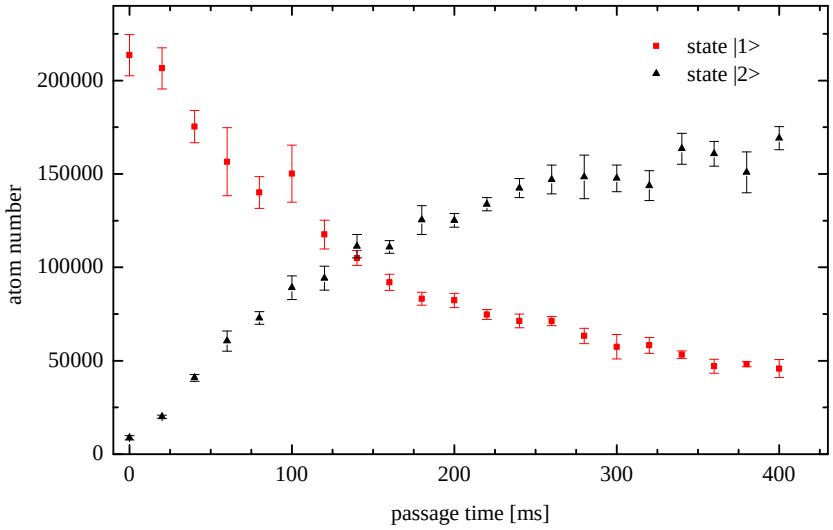

Figure 5.5: Landau-Zener passage between states $|1\rangle$ and $|2\rangle$ for different ramp speeds during the first part of the evaporation. The absorption images are only taken after the complete evaporation. If the imbalance is to big then no atoms in the minority component are left after the complete evaporation. One sees that not the whole sample can be transfered to state $|2\rangle$. The reason for that is that the sample decoheres during the passage.

A way to produce arbitrary ratios of a mixture and at the same time a method which is not so vulnerable to drifts of the apparatus, is given by adiabatic and non-adiabatic Landau-Zener passages [Lan32, Zen32, Met99]. Here, the frequency is swept over the resonance and if this is done adiabatically the complete population of a state can be transferred into the other one. If one increases the sweep rate, one can transfer arbitrary fractions. The probability of the transfer is given by the Landau-Zener law: $P_{\text{transfer}} = 1 - e^{-2\pi\Omega_R^2/\dot{\omega}}$, here Ω_R is the Rabi frequency, which is fixed for a given RF power and a certain transition and $\dot{\omega}$ is the sweep rate. After this transfer, the sample is still in a coherent superposition, which in

this case consists of arbitrary amplitude fractions $\propto a\,|1\rangle + b\,|2\rangle$, depending on the sweep rate. But due to magnetic field inhomogeneities the sample decoheres. This process is analyzed more thoroughly in the next section. Figure 5.5 shows such a Landau-Zener passage between states $|1\rangle$ and $|2\rangle$. Here, the passage is performed during the first part of evaporation near resonance, afterwards the sample is evaporated further. During this evaporation the absolute imbalance ($N_1 - N_2$, with N_i being the number of atoms in state $|i\rangle$) stays the same for a non-degenerate sample. But as soon as the sample becomes degenerate, the majority component is preferentially lost. Therefore, the observed number of atoms cannot be described by the Landau-Zener law. However, it is obvious that with this technique, we are able to invert the initial excess of state $|1\rangle$ atoms and end up with more atoms in state $|2\rangle$ if the sweep time is sufficiently long ($\Omega_R^2 \gg \dot{\omega}$). But even for very long sweep times, we are not able to transfer all atoms from state $|1\rangle$ to $|2\rangle$, this can be explained by decoherence occuring during the passage. One therefore sees that the timescales of decoherence in our system is on the order of several hundreds of ms.

Decoherence during radio frequency pulses

As we observed in the previous section, it was impossible to adiabatically transfer the complete population of a state. The reason for this is that the sample decoheres during the passage. If one considers a Bloch sphere representation, the passage does nothing else than rotating the pure state on the Bloch sphere. Only after some time, decoherence occurs due to magnetic field inhomogeneities. This dephases the pure state into a "ring" state [Zwi03a], whose average then has no coherences (off-diagonal matrix elements in the density matrix). Decoherence denotes the irreversible local disappearance of these coherences in the one-particle density matrix.

Since magnetic field curvatures are the main reason for our magnetic field inhomogeneities, the decoherence time strongly depends on the location of the cloud inside the main chamber. After having installed the high resolution imaging system in the vertical axes, we were able to optimize the trap to a position, where the magnetic field gradients are minimized. After this change, the decoherence time changed from several tens of milliseconds to several hundred milliseconds. Even after 15 ms no sign of decoherence, i.e. damping of the Rabi-frequencies, can be observed (see figure 5.4). Before this change, the Rabi oscillations were overdamped and we could at most see half a period of an oscillation. As a result, the population imbalance could be removed in the old setup by shining in sufficiently long pulses (mostly about 850 ms), because the stationary state consists of a non-coherent mixture with equal populations. Figure 5.6 shows such a decohered transition.

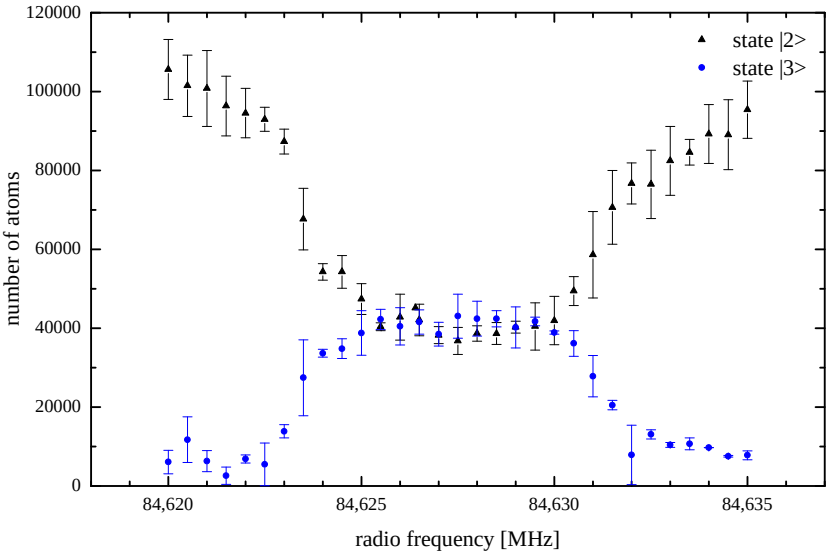

Figure 5.6: Decohered $|2\rangle$ to $|3\rangle$ transition after a rf pulse of 850 ms. Due to magnetic field fluctuations and saturation effects the transition is broadened.

The stationary solution to the three-state system is also a balanced sample, hence we applied the frequencies of the $|1\rangle - |2\rangle$ and $|2\rangle - |3\rangle$ transition for about 850 ms and finally we ended up with an equally balanced mixture of the three states $|1\rangle$,$|2\rangle$ and $|3\rangle$. The experiments described in this thesis were performed at the old position of the trap, with shorter decoherence time. Therefore, 850 ms was sufficient to ensure a completely balanced and decohered sample. A problem here was that at our magnetic field values the observed width of the $|1\rangle - |2\rangle$ transition is very narrow (0.5 kHz) and thus had to be remeasured and adjusted every day. To avoid this problem, we now use a different scheme to produce the three-component mixture. During the first evaporation stage, we make a non-adiabatic Landau-Zener passage in the $|1\rangle - |2\rangle$ mixture, that leaves us with slightly more atoms in state $|2\rangle$ than in $|1\rangle$. As the absolute imbalance stays the same during evaporation of a non-degenerate sample, the relative imbalance increases if fewer particles are left. We choose the initial imbalance so that we end up with twice as many particles in $|2\rangle$ after finishing the evaporation at 300 Gauss. After ramping the magnetic field to the region of the zero-crossings, we can balance the sample by just shining in a pulse resonant with the $|2\rangle - |3\rangle$ transition and wait until the whole sample is balanced and decohered. This transition is broader and hence easier to drive. Saturation effects additionally broaden the transition. As seen in figure 5.6 this particular transition is then about 25 kHz wide.

5.5 Thermometry of Ultracold Fermi Gases

In this section, we will explain how we determined the temperatures of the Fermi gases produced in our experiments. During the experiments, we record the two dimensional density distributions by absorption imaging after switching off the trap and letting the cloud expand for several ms of time-of-flight. This density is then integrated along the other radial direction, in order to reduce the noise and to facilitate the fitting procedure. The result of this procedure is the axial density $n(z)$.

To determine the sample's temperature and its atom number, we use several schemes.

A Gauss fit is used to determine the atom number and temperature of the sample on the fly (in each experimental cycle). The resulting parameters are saved together with the two dimensional absortion image of the density distribution ($n(x, z)$) and can later be processed further. This Gauss fit is only correct for a thermal sample, which has a Maxwell-Boltzmann distribution.

For degenerate Fermi gases, we additionally developed a fitting routine that utilizes the Fermi-Dirac integral function. This fit (from here on called Fermi fit) is more elaborate and hence takes too long (about 30 to 45 seconds) to be done in each experimental cycle. It can, however, be employed after the actual measurements for experiments with degenerate samples that rely on an accurate thermometry.

After the discussion of the two fitting procedures outlined above, we will show at the end of this section how a third component can be used as a non-degenerate temperature probe and thus avoid the evaluation of the Fermi-Dirac integral, which can only be solved numerically.

The Gauss fit

A thermal Fermi gas in a harmonic trap can be described by a Maxwell-Boltzmann distribution. Thus, after letting the cloud expand for a certain time-of-flight, the density distribution can be used to deduce the initial momentum distribution by fitting a Gaussian profile. For this process, we assume a ballistic expansion, which means that the interactions occuring during the expansion can be neglected. Since we perform our thermometry near the zero-crossing of the scattering lengths and since our Fermi gases are very dilute, this assumption is more than justified. We normally fit the axial density distribution $n(z)$ of a cigar-shaped sample, where the z-direction is the long axes of the cloud (aspect ratio about 1/10). After switching off the trap we let the cloud expand until the size is more than a factor of 20 larger than the initial width. Therefore, the initial size of the cloud can be neglected. The thermal energy ($k_B\,T$) of the initally trapped sample is completely converted

into kinetic energy ($m\,v^2/2$) after sufficiently long time-of-flights and thus the temperature of the sample can be written as

$$T = m\,v^2/(2\,k_B) = m\,\sigma^2/(2\,k_B t_{tof}), \tag{5.3}$$

where σ is the Gaussian width of the cloud after the time-of-flight t_{tof}. From the integral of the axial density distribution the number of particles in the sample can be deduced (see [Koh08]).

The Fermi fit

For a degenerate sample, the density and momentum distribution are described by the Fermi-Dirac integral function (see section 2.2.1). We already noted that using this function is rather complicated since it is only numerically calculable. In addition, the chemical potential is also not analytically accessible. However, we tried to develop a fitting routine which is able to determine the temperature of a degenerate sample based on numerical calculations of the Fermi-Dirac integral (numerical method described in [Goa95]).

Since we examine the axial density distribution, we employ the cylindrical symmetry of the sample and integrate equation 2.32 over dp_x and dp_y. Using the relation 2.30 one obtains

$$n(p_z) \propto f_{5/2}\left(\exp\left(\frac{\mu - p_z^2/2m}{k_B\,T}\right)\right). \tag{5.4}$$

Thus after a time-of-flight this results in

$$n_{tof}(z) = n\left(p_z = \frac{m\,z}{t_{tof}}\right) \propto f_{5/2}\left(\exp\left(\frac{\mu - \frac{m}{2\,t_{tof}^2}\,z^2}{k_B\,T}\right)\right). \tag{5.5}$$

Since we only need the Fermi fit to determine the temperature below about $T/T_F \approx 0.5$ (as we will see later, the Gauss fit still works for higher temperatures), we use the Sommerfeld approximation for the chemical potential. This significantly simplifies the problem, but still we have to evaluate the Fermi-Dirac integral. For this we used the Gnu Scientific library (GSL) [Gnu] that includes a numerical calculation of the Fermi-Dirac integral in its special functions. We produced a look-up table (1000 exponentially spaced values), which was then imported into an Origin C fitting routine and linearly extrapolated between every two points. Origin uses this table and the Levenberg-Marquardt algorithm to perform non-linear fits to axial density distributions imaged after a time-of-flight. The fitting parameters are an overall offset, an amplitude, the center of the distribution and T/T_F.

In order to check the reliability of the fit we simulated Fermi distribution functions (using the Sommerfeld approximation) with different temperatures using our

experimental parameters, for example the pixel size and resolution of our camera. These "theoretical" distibutions were then fitted with a Gauss and the Fermi fit, an example of such a test fit for $T/T_F = 0.05$ can be found in figure 5.7 (a). A experimentally measured sample with about the same temperature is analyzed in 5.7 (b).

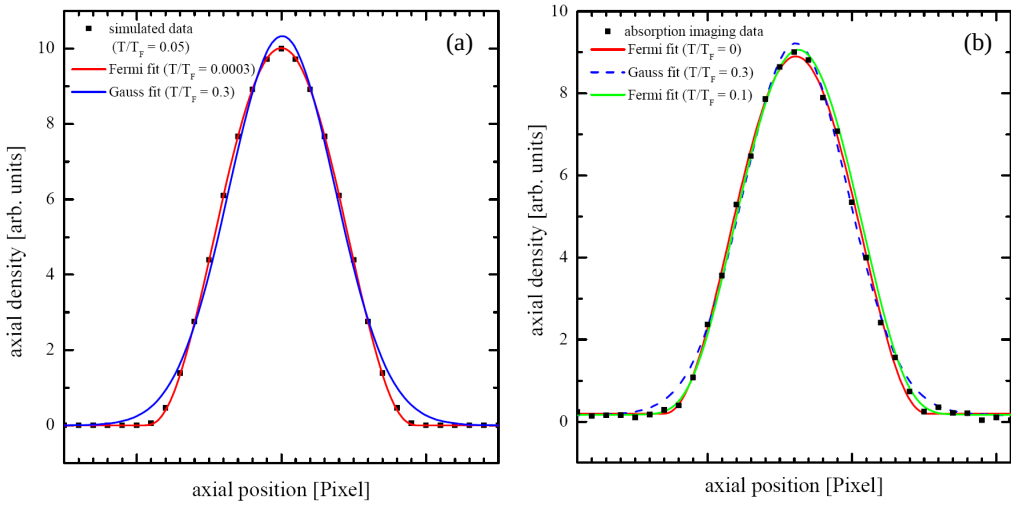

Figure 5.7: Simulated (a) and experimental (b) axial density distribution (black squares) with a Gaussian and a Fermi fit. The number of points in the simulation is chosen so that it resembles the Pixel size and amplification of our camera setup. One clearly sees that for both simulation and experiment, the Gaussian fit does not resemble the distribution very well, it overestimates the height and has wider wings. The difference in shape between simulated $T/T_F = 0.05$ and fitted Fermi distribution ($T/T_F = 0.0003$) in (a) is only marginal. The differences between the Fermi fits with $T/T_F = 0$ and $T/T_F = 0.1$ to the experimental data are due to the additional experimental uncertainty so small that they can (at our optical resolution) hardly be distinguished.

These simulations were carried out for various temperatures. Consequently, we were able to compare the Fermi and Gauss fit. This comparison can be found in figure 5.8 and several interesting conclusions can be drawn from this. First, one notices that for high temperatures ($T/T_F \gtrsim 0.5$) the Gauss fit, the Fermi fit and the simulated density distribution in Sommerfeld approximation all coincide. This can be explained by the fact that for temperatures above $T/T_F \sim 0.5$ the fugacity $z = e^{\mu/(k_B T)}$ is smaller than unity, hence the one in the denominator of the Fermi distribution can be neglected and one obtains a Gaussian distribution function. The fugacity is then only a numerical constant multiplying the overall amplitude, but this value is a free fitting parameter and is not used for the analysis.

Thus using the Sommerfeld approximation for higher temperatures is not an issue and the Gaussian and the Fermi fit reproduce the simulated density distributions well.

For colder temperatures ($T/T_F \lesssim 0.5$), the Gaussian does not fit the simulated data. It constantly overestimates the temperature and saturates at a value of about $T/T_F = 0.3$. The Fermi fit does not perform well in this region either, which is most likely due to the little data points available in the relevant region (i.e. in the wings), the use of the Sommerfeld approximation and the employment of a finite look-up table for the Fermi-Dirac function. We noted earlier (section 2.2.1) that for temperatures below $T/T_F = 0.3$, the changes due to degeneracy are so marginal, that given the low resolution of our camera system, it is hardly possible to see the differences from a $T = 0$ Fermi gas. This explains why the Fermi fit gives a temperature of about $T/T_F = 0.0003$ for a simulated sample of $T/T_F = 0.05$ (see figure 5.7 (a)).

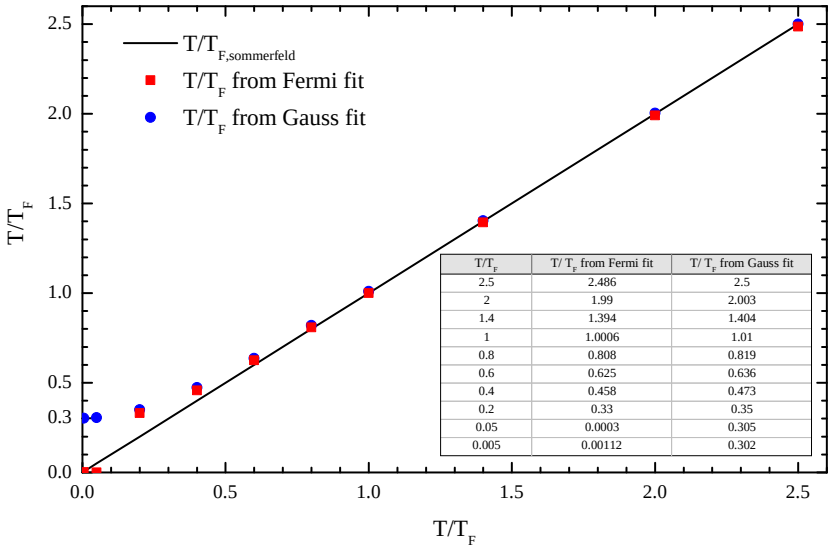

T/T$_F$	T/ T$_F$ from Fermi fit	T/ T$_F$ from Gauss fit
2.5	2.486	2.5
2	1.99	2.003
1.4	1.394	1.404
1	1.0006	1.01
0.8	0.808	0.819
0.6	0.625	0.636
0.4	0.458	0.473
0.2	0.33	0.35
0.05	0.0003	0.305
0.005	0.00112	0.302

Figure 5.8: Comparison of a Gauss and the Fermi fit to an axial density distribution simulated in the Sommerfeld approximation with our experimental parameters (more details in the text).

Although it seems that the Fermi fit does not provide a useful tool for analysis, there were several useful conclusions that we could draw from this discussion and evaluation. First, with our new high resolution imaging setup we could in principle obtain better results, especially if the look-up table is enlarged or fitted better for higher values of the fugacity. Additionally, the calibration shown in figure 5.8 can be used to deduce an approximate temperature by looking at the temperature given through the Gauss fit and extrapolating this to the "real" temperature. This

is not at all an exact calculation, because a lot of approximations were made and certain parameters, for example for the resolution and pixel size were assumed. It can nevertheless provide a good guess for the temperature of the Fermi gas.

However, for a more precise thermometry, we had to use a technique developed at Jila [Reg05], which will be discussed in the next section.

Thermometry using the third component

Another method to determine the temperature of a degenerate Fermi gas, which works especially well for medium degeneracy ($T/T_F = 0.2 \ldots 0.5$), is the application of an additional spin state as a non-degenerate temperature probe. This technique uses the fact that the Fermi energy scales with the atom number, we recall that

$$E_F = (6\,N)^{1/3}\ \hbar\,\bar{\omega}. \tag{5.6}$$

Thus if the number of atoms is smaller, the Fermi energy is also smaller. By populating an additional spin state with less particles than the initial one, the Fermi energy of the new component is lower. If one now assumes that the components are in thermal equilibrium, then the resulting T/T_F of the new component is larger.

Let us assume that we start with a two-component sample with $75\,000$ atoms in each state ($|1\rangle$ and $|2\rangle$) at an absolute temperature of 215 nK and $T/T_F = 0.3$. If we now transfer some atoms to state $|3\rangle$(for example $N_3 = 20\ 000$), then the resulting T/T_F is 0.466. This value can now already be fitted with a Gaussian distribution because the effects of degeneracy are negligable for such values of T/T_F.

This method however, can only be applied if the three-state mixture is long lived. Additionally, the gas should be weakly interacting, because we neglect all effects of interaction. Both requirements are met for the magnetic field region near 550 Gauss, where we perform our thermometry. We will see later that the lifetimes of the three-component mixture is on the order of 30 seconds. This is sufficient to let the sample decohere after the population of the third state by radio frequency pulses. However, the degeneracy must not be to strong if one wants to use a Gaussian fit for the minority component.

This process, which facilitates our thermometry, is not favourable for the production of a very cold three-component sample. It sets a limit to the lowest achievable temperatures in a three-state mixture, since one normally cools a two-component mixture (due to the short lifetimes for strong interactions in a three-state mixture) and then adds the third component. Thus even if the two-state mixture has a very low T/T_F the final T/T_F in a three-component gas is significantly larger (by a factor $N_2^{1/3}/N_3^{1/3}$).

Chapter 6

Experiments with Three-Component Fermi Gases

This chapter focuses on the experiments with three-component samples, which were performed during this thesis. Some of the measurements present here were published in [Ott08]. This chapter also contains additional measurements, especially of the high-field region (600 - 1400 Gauss). Furthermore, we explain the model used to describe the measured three-body loss and show how we extract the three-body loss coefficient K_3 from the experimental data. The observed behavior of K_3 cannot just be explained by the two-body scattering lengths. Therefore, we introduce an effective interaction parameter for the fermionic three-body case, which, together with the formulas derived in section 3.3, is able to explain our results suprisingly well. The model used is based on universality of systems with large scattering lengths and Efimov physics and it predicts a three-body bound state that crosses the continuum at two different magnetic field values. At the end of this chapter we comment on very recent theoretical work dealing with our experiments [Bra08, Nai08, Sch08a], they all predict a trimer state crossing the continuum although the theoretical approaches used differ significantly.

Most measurements in this chapter were done with the "old" RF setup (see section 4.3), thus the sample was produced as explained in section 5.4.2. The imaging was performed with the horizontal imaging setup (see section 4.4.1).

6.1 Collisional Stability of a Three-Component Fermi Gas

The first experiments conducted, investigate the stability of the three-component Fermi mixtures as a function of the magnetic field. We expected that in the region of strong interaction (650 - 1200 Gauss), later referred to as "high-field region",

the sample was quite unstable due to the molecular states associated with the Feshbach resonances and the large values of the scattering lengths, which enter the three-body loss rate $\propto a^4$ (at that time known for the case of identical bosons [Web03b]). Thus we first looked at the low magnetic field region from 0 to roughly 650 G (from here on called "low-field region"), where we expected the sample to be more stable. But we were surprised by the strong variation of loss for different magnetic fields.

6.1.1 Low-Field Region

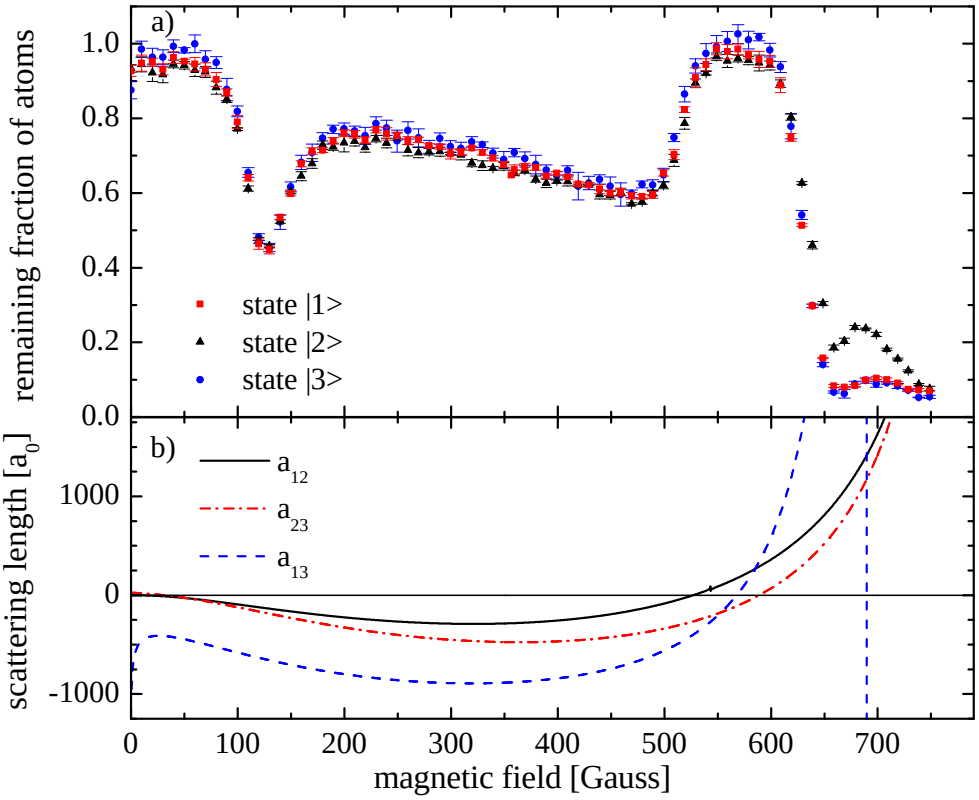

Figure 6.1: a) Remaining fraction of atoms after holding them for 250 ms at various magnetic fields. Each point is the average of at least five independent measurements. The sample contains 50 000 atoms per state at a density of 6×10^{11} atoms$/cm^3$ and has a temperature of roughly 215 nK. The two-body scattering lengths for all possible combinations are shown in b) (taken from [Jul], for symmetry reasons $a_{ii} = 0$ for s-wave interaction).

The data taken in the low-field region is shown in figure 6.1. For these measurements, a three-component Fermi gas was produced as explained in the previous

chapter. Then we ramped to a certain magnetic field, waited for 250 ms and finally imaged the remaining fraction of atoms. One clearly sees strong variations in the collisional stability of such a three-state sample. The measurements were performed with a mixture consisting of 50 000 atoms per state at a temperature of 215 nK and a density of 6×10^{11} atoms$/cm^3$. The harmonic cigar-shaped optical dipole trap had trapping frequencies of $\omega_x = \omega_y = 2\pi \times 386(15)$ Hz in the transversal and $\omega_z = 2\pi \times 38(2)$ Hz in the longitudinal direction (measured as explained in [Koh08]). Using the thermometry explained in section 5.5, we measured the sample to be slightly degenerate ($T/T_F \approx 0.37$).

In order to exclude two-body processes, we repeated the experiments with all possible binary mixtures (see figure 6.2). Thus we could clearly show that the loss processes observed below 600 Gauss are solely due to three-body interactions of three distiguishable fermions. The data produced with binary mixtures show that the binary mixtures are stable beside the regions where molecules are formed (above 600 Gauss). This can be expected since every three-body process in a two-state mixture involves two identical fermions and is thus Pauli blocked. That the interactions in our case only occur between different hyperfine states also helps us to avoid a problem present in earlier experiments [Bur97, Web03b], which measured three-body loss rates in bosonic samples, where it is difficult to exclude two-body processes.

We then tried to explain the behavior in the three-component mixture by the behavior of the two-body scattering lengths. This only worked near 0 Gauss and at about 550 Gauss. In these regions, two or more scattering lengths are small compared to the van der Waals length $l_{vdW} \approx 60\, a_0$, which represents the short range length scale of the problem. In the case of two small scattering lengths and a large one compared to l_{vdW}, we effectively have an interacting two-component sample, which is stable and an additional non-interacting 'spectator' Fermi gas consisting of the third component. As a result, the three-body loss is weak. If only one scattering length is small, then one component still strongly interacts with both other states and therefore it can mediate the strong interaction (see figure 6.3).

Beside these regions, the two-body scattering lengths could by no means explain the observed loss. Around 130 Gauss we observed a strong loss feature, which could not be explained at that time. Possible interpretations were spin changing collisions, relaxation into a deeply bound dimer state or a three-body bound state crossing the continuum. We were especially puzzled that the two-body scattering lengths were totally smooth and negative in that region and hence did not provide an obvious explanation at all.

For higher fields (200 - 500 Gauss), an almost linear dependence of the three-body loss was observed as a function of the magnetic field. This could also not be explained using the two-body interactions. It was not clear why the loss did not

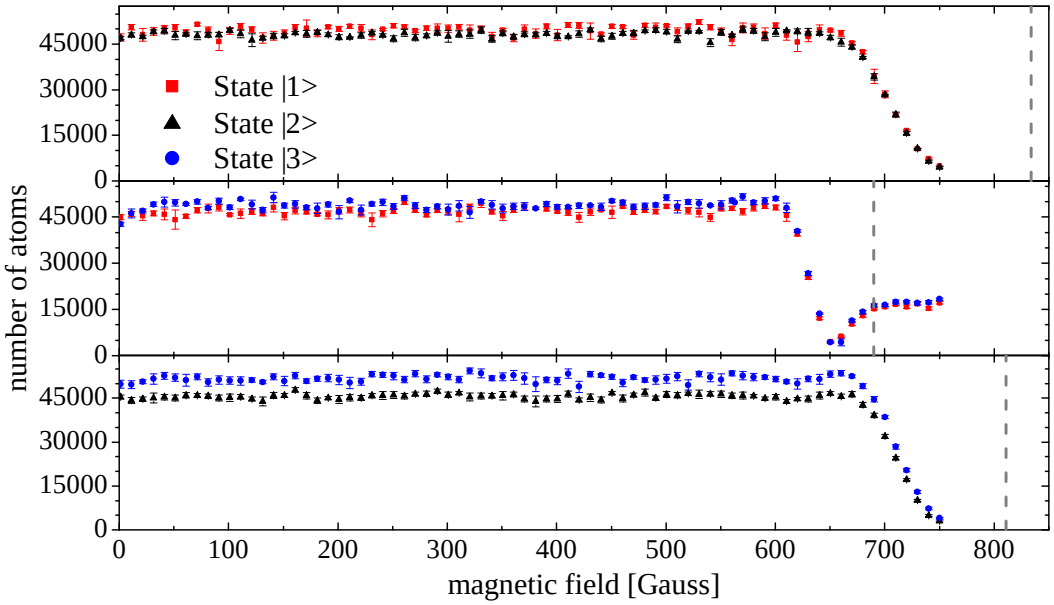

Figure 6.2: Number of atoms after 250 ms at various magnetic fields for all binary mixtures. The vertical dashed lines indicate the position of the particular Feshbach resonance. Below 600 Gauss all samples are stable. In the region, where the respective dimer changes from a universal weakly bound state (where still fermionic behavior of the constituents of the dimers is observable) to a deeply bound bosonic dimer, inelastic collisions lead to loss in the binary sample due to molecular relaxation (process 5.2 b).

have its maximum where the scattering lengths do, namely at about 300 Gauss. At about 500 Gauss, the stability reaches another minimum, which is not as pronounced as the one near 130 Gauss. For fields above this value the behavior changes rather drastically from a region of strong loss (near 500 Gauss) to a region where the sample is stable (530 - 610 Gauss) with lifetime up to 30 seconds.

In the magnetic field region above about 610 Gauss, $|1\rangle - |3\rangle$ molecules start to form. As we image the cloud at 526 Gauss, the molecules are not detected when we ramp the field there. This imaging procedure is also responsible for the behavior of state $|2\rangle$ between 650 and 750 Gauss.

In order to investigate the position of the loss 'resonance' near 130 Gauss and to observe possible asymmetries, we repeated the measurements shown in figure 6.1 only with higher magnetic field resolution (see figure 6.4) . In this case, the sample had a temperature of about 1 μK and contained about 150 000 particles per state. It was held for 250 ms at magnetic fields in the vicinity of the loss feature and imaged at 526 Gauss. Additionally, we also recorded the temperature of the sample as a function of the magnetic field. One clearly sees that the stronger the

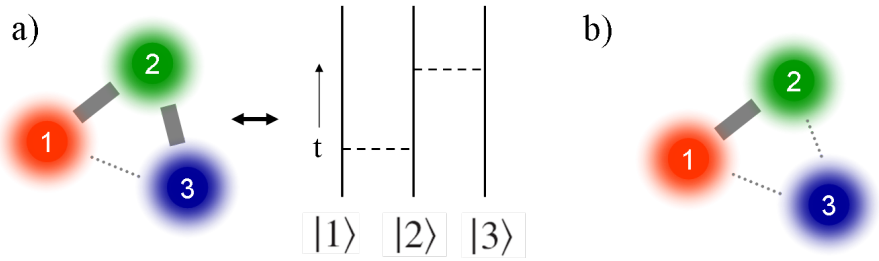

mediated three-body process possible three-body processes surpressed

Figure 6.3: The width of the lines between the respective states indicates the strength of the interaction. For two large (here a_{12} and a_{23}) and one small (a_{23}) scattering length (always compared to the van der Walls length l_{vdW}) three-body interactions are still possible. They are mediated by the state $|2\rangle$, which first interacts with one and than with the other state (see a)). If only one scattering length is large (e.g. a_{12}) three body processes are suppressed, because binary mixtures are stable (see b)).

loss the higher the temperature of the remaining sample. This would not happen if all atoms of the sample decay at the same rate and immediately leave the trap after the process took place. Therefore, either some particles remain in the sample after getting energy in the process responsible for the loss or a kind of anti-evaporation takes place. This means that the loss process is more likely in regions, where the density is higher, which would be in the center of the trap. The average temperature of the atoms is here smaller than at the edges of the trap. Thus the probability is higher to loose colder atoms. This leads to an effective increase in temperature, from our point of view this was the most probable scenario and therefore we included this in the analysis of the three-body loss rate in section (6.2).

With the measurements shown in figure 6.4 we were able to determine the narrow loss resonance's location to 127 ± 2 Gauss for a temperature of 1 μK. We also checked if the feature persists at higher temperatures. The result was that the qualitative behavior and the resonance position change only within our experimental uncertainties in a quite large temperature domain (about 150 nK to roughly 10 μK).

The slope on the low-field side of the loss resonance seems to be a bit steeper than on the other side. On the high-field side, the 'background' loss (beside the resonance) is stronger. For one certain magnetic field value (214.85 Gauss), the number of remaining atoms in state $|2\rangle$ is strongly reduced. The reason for that is the narrow p-wave Feshbach resonance for state $|2\rangle$ located at 214.9 Gauss with a width of 0.4 Gauss [Sch05]. This good agreement shows that our magnetic field calibration is reasonable.

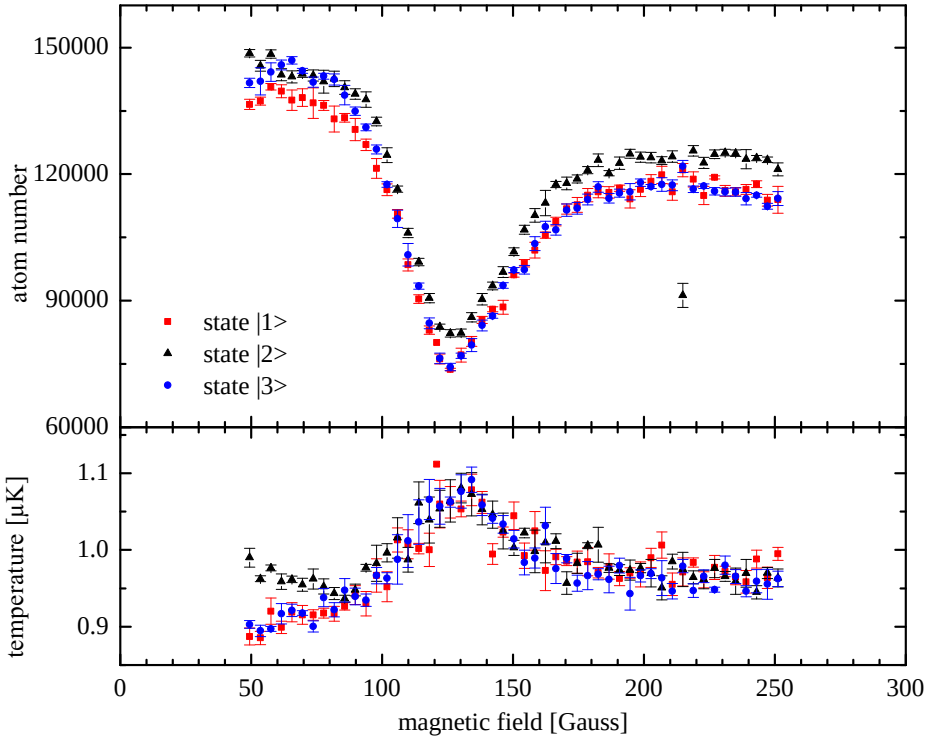

Figure 6.4: Measurement of the remaining fraction of atoms in a three-component Fermi gas after holding it for 250 ms in the vicinity of the "loss feature" near 130 Gauss. Additionally, the temperature was measured and one sees that the stronger the loss, the higher the temperature of the remaining sample. At 214.85 Gauss the number of remaining atoms in state $|2\rangle$ is significantly reduced, this can be attributed to the known p-wave Feshbach resonance for state $|2\rangle$ at 214.9 Gauss (width of 0.4 Gauss).

In conclusion, we were able to produce a balanced three-component mixture which was mildly degenerate. At some magnetic field values, namely around 550 Gauss and below 50 G, the created mixture exhibits a remarkable stability with a 1/e lifetime of more than 30 s. This leaves time for conducting more advanced experiments, like loading the mixture into an optical lattice.

By performing reference measurements with all possible binary mixtures, we could exclude two-body processes in the magnetic field region below 600 Gauss. Hence all structures in the loss below that field have to be caused by three-body processes involving one particle in each state. Furthermore, we observed a prominent loss feature at 126 Gauss (with a FWHM width of about 50 Gauss) and an almost linear increase of the loss from 200 to 450 Gauss. This linear slope leads to a second, broader loss maximum around 500 Gauss. However, we were not able

to explain or understand the observed behavior by means of the two-body interactions. Thus further investigations were necessary. In order to get more quantitative information, we then started to measure the loss as a function of time for different values of the magnetic field and deduced the three-body loss coefficient from this (see section 6.2).

6.1.2 High-Field Region

Before we investigated the low-field region in more detail, we also examined the high-field region from 600 to 1400 Gauss (figure 6.5). Here the scattering lengths in the different channels diverge because of the broad and overlapping Feshbach resonances at 690 Gauss ($|1\rangle - |3\rangle$), 811 Gauss ($|2\rangle - |3\rangle$) and 834 Gauss ($|1\rangle - |2\rangle$). In contrast to the region below 600 Gauss, the binary mixtures are not stable in several magnetic field regions, where it is almost impossible to distinguish between two- and three-body processes.

Owing to the strong interactions, the lifetime of the sample is significantly shorter than in the low-field region. We therefore held the sample for 20 ms (low-field region: 250 ms) at the respective magnetic fields. Still, the loss was so drastic that only a third of the sample remained at the magnetic field of strongest loss. This supports the statement in [Sch08b] that the lifetime on resonance (691 Gauss) is of the order of 30 ms. Our measurements were performed with a non-degenerate sample at a temperature of $1.2\,\mu K$ and about 90 000 atoms per state (see figure 6.5). The number of atoms per state was not totally matched in this case. As one can see, there was a slight imbalance towards more atoms in state $|1\rangle$ and less in state $|3\rangle$. But we expect that this does not change the qualitative behavior of the sample significantly. Due to molecule formation we had to image the cloud at a magnetic field above all resonances, so the atoms initially bound in molecules could also be observed. Thus we ramped to 1150 Gauss after each experimental cycle and imaged the remaining cloud (one spin state per cycle). The error bars show the statistical deviations from six independent measurements. They are only displayed for one magnetic field value, as they are of the same order of magnitude for the complete magnetic field region.

In contrast to the low-field region, the sample's stability has no distinct loss extrema, beside the enhanced loss in the region of 650 Gauss where the $|1\rangle - |3\rangle$ binary mixture becomes unstable. In the region above 850 Gauss, the lifetime increases. This can be explained by the fact that the scattering lengths decrease for higher fields. Above 1200 Gauss the stability seems to saturate. This behavior can also be understood by means of the two-body interactions. In this region, all three scattering lengths reach their background value of roughly $-2000\,a_0$. As a result the behavior in the high-field region seems to be explainable and understandable by means of the behavior of the two-body scattering lengths. We will later analyze

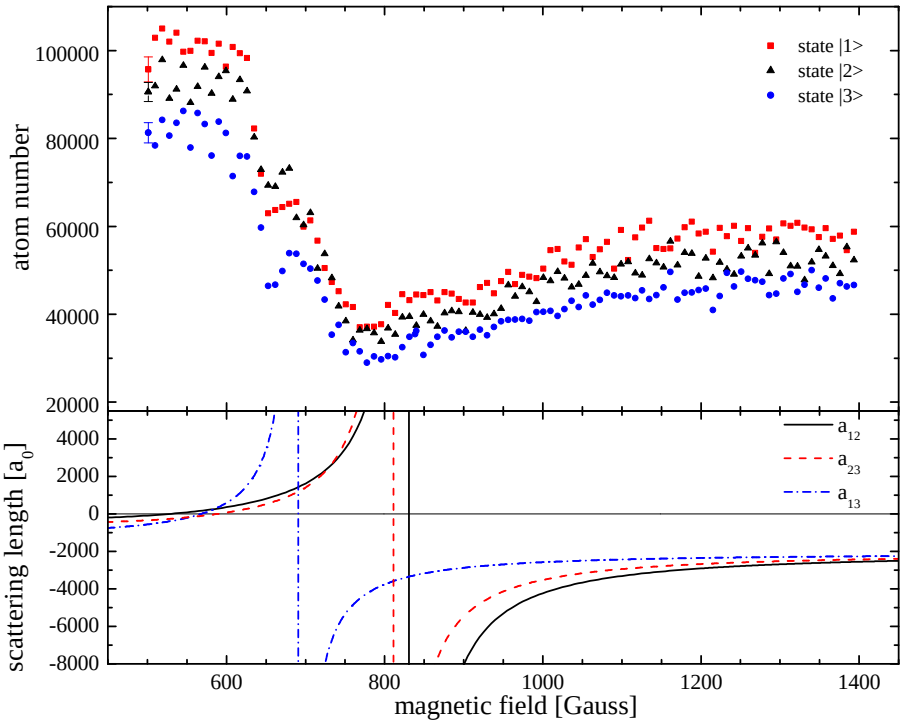

Figure 6.5: Number of atoms remaining in a three-state mixture after holding the sample at different magnetic fields for 20 ms. The strongest loss occurs in the region of 750 to 800 Gauss, there a_{23} and a_{12} are very large and positive. With the decrease of the scattering lengths on the BCS sides, the loss also diminishes. But aside the region of 650 Gauss, where the $|1\rangle|3\rangle$ binary mixture is unstable, there are no distinct loss extrema observable.

this more thoroughly and show that this is not completely true.

This magnetic field region is partcicularly interesting because the interactions in all channels are almost equal and thus the sample has a SU(3) symmetry. This is an important point for future experiments, which could for instance try to study SU(3) Hubbard models.

6.2 Three-Body Processes in a Three-Component Fermi Gas

As explained earlier, we sought a more quantitative measurement of the trap loss. On this account, we recorded the number of atoms and the temperature of the sample as a function of time for various magnetic fields. From the recorded decay curves, one can extract the three-body loss coefficient K_3 for each state and each

magnetic field value.

In our case, the three-body loss happens almost entirely due to three-body recombination, which means two particles form a bound state and the third one carries away the excess momentum. Therefore, we will use the terms "three-body loss" and "three-body recombination" synonymously from now on (in our case they only differ by a numerical factor). But a priori this is not necessarily the only imaginable process.

From the stable binary mixtures (see figure 6.2), we can infer that below 600 Gauss two-body processes are negligible ($K_2 \approx 0$). Hence the relevant processes leading to trap loss are one-body processes (e.g. collisions with the background gas or scattering with trap photons) and three-body collisions between one atom of each spin state $|1\rangle$, $|2\rangle$ and $|3\rangle$. All processes including atoms in the same state or more than three particles are Pauli blocked, because they would include two identical fermions. Therefore, we will neglect those processes in our analysis.

In this section we will follow the reasoning and model deduced in [Web03b, Web03a] and for the numerical analysis we will use the program code developed in Innsbruck [Web03b].

6.2.1 Theoretical Model of the Three-Body Loss

Equation for the number of atoms

The differential equation that governs the loss processes is given in the most general case by

$$\dot{n}(\boldsymbol{r}, t) = -\sum_i K_i \, n^i(\boldsymbol{r}, t), \tag{6.1}$$

with $n(\boldsymbol{r}, t)$ being the atomic number density and K_i the i-body loss coefficient. In our case, neglecting two-body processes and all processes with $i \geq 4$, this can be reduced to

$$\dot{n}(\boldsymbol{r}, t) = -K_1 \, n(\boldsymbol{r}, t) - K_3 \, n^3(\boldsymbol{r}, t). \tag{6.2}$$

Sometimes the use of the three-body recombination rate α_{rec} is preferred. It describes the number of recombination events per time and is connected to K_3 as follows:

$$K_3 = n_{loss} \, \alpha_{rec}, \tag{6.3}$$

where n_{loss} is the number of atoms lost per recombination event. In our case, the released binding energy of the deeply bound dimer state is large compared to depth of the trap, at least in the magnetic field region <600 Gauss, where no shallow bound state exists. Hence, all three atoms involved receive a significant amount of kinetic energy and as a result they all leave the trap. Consequently, $n_{loss} = 3$ and we obtain $a_{rec} = \frac{1}{3} K_3$.

In order to obtain observable quantities such as temperature T and atom number N, we have to average over the complete sample. We assume a harmonic trap with an average trap frequency of $\bar{\omega} = (\omega_x\,\omega_y\,\omega_z)^{1/3}$ and hence for a non-degenerate sample a Gaussian density distribution. From the normalization $N = \langle n \rangle = \int n(\boldsymbol{r})$, we obtain

$$n(\boldsymbol{r}) = N \left(\frac{a}{\pi}\right)^{3/2} e^{-a\left(x^2+y^2+z^2\right)}, \tag{6.4}$$

with $a = \frac{1}{2}\,m\,\bar{\omega}^2/(k_B\,T)$. The averaged differential equation then reads

$$\dot{N} = -K_1\,N - K_3\left\langle n^3 \right\rangle. \tag{6.5}$$

Here, we omitted the explicit time dependence of the density, which is possible since the time evolution can be separated if the thermalization rate is large compared to the loss rate (see [Kra06a]). With

$$\left\langle n^3 \right\rangle = \frac{1}{\sqrt{27}} \left(\frac{m\,\bar{\omega}^2}{2\,k_B\,\pi}\right)^3 \frac{N^3}{T^3}, \tag{6.6}$$

we obtain the following differential equation for the atom number:

$$\frac{dN}{dt} = -\alpha\,N - \gamma\,\frac{N^3}{T^3}, \tag{6.7}$$

with $\alpha = K_1$ and $\gamma = K_3\,\frac{1}{\sqrt{27}} \left(\frac{m\,\bar{\omega}^2}{2\,k_B\,\pi}\right)^3$.

Equation for the temperature dependence

As stated earlier the three-body recombination process leads to an increase of the sample's temperature due to "anti-evaporation". The reason for this is that the probability for a three-body process to occur scales with the density to the third power ($\propto n^3$). Hence, recombination occurs more often in the region of high density, i.e. in the center of the trap. As the mean temperature of the atoms is lower there, this results in heating of the cloud during the loss. For our experimental parameters the heating through recombination amounts to about 20 per cent of the temperature of the sample.

One now needs a model that mimics the temperature increase during the loss. Our ansatz to include this effect, was to compare the average energy of a trapped particle $(3\,k_B\,T)$ to the heating energy $(k_B\,T_h)$. Therefore, we obtain the following relation

$$\frac{\dot{T}}{T} = \frac{\dot{N}}{N}\,\frac{k_B\,T_h}{3\,k_B\,T}. \tag{6.8}$$

If we now plug in equation 6.7 and assume that only three-body events lead to heating, the resulting differential equation for the temperature dependence is

$$\frac{dT}{dt} = \gamma \frac{N^2}{T^3} \frac{T_h}{3}. \tag{6.9}$$

The Innsbruck model defines the heating energy as $k_B\,(T + T_h)$ (see [Web03a]). This results in a more difficult differential equation and thus a more unstable numerical convergence. But since the increase in temperature is relatively small compared to the absolute temperature of the sample, this does not significantly change the result. As one can see later, our simpler model is able to describe the increase of temperature completely satisfactory. If we examine our fitted heating energy T_h, we indeed observe that it is on the order of the temperature of the sample T. This shows that all parts of the recombination event (dimer and high energy atom) leave the trap without depositing a significant amount of additional energy in the sample and that other heating processes are negligable.

Numerical method

The numerical method used for the analysis was developed by T. Weber and it is carefully discussed in his thesis [Web03a] or in [Web03b]. The main idea of this numerical optimization process is to iteratively solve the coupled differential equations 6.7 and 6.9 with three parameters α, γ and T_h such that the sum error of squares is minimized. Therefore one first chooses an initial α and γ (done by a fit without temperature dependence). With those values one fits the experimentally obtained temperatures with equation 6.9 with T_h being the only fitting parameter. Using the obtained result, one can calculate the error sum of squares between the observed atom number and the numerical solution of 6.7. These steps are then repeated while α and γ are changed such that they minimize the error sum. A Matlab nonlinear optimization algorithm is used for this process [Web03a].

6.2.2 Experimental Determination of the Three-Body Loss Rate

For every state ($|1\rangle$, $|2\rangle$ and $|3\rangle$) and every magnetic field value we measured the atom number and temperature for hold times from 0 to 5 s (250 ms steps, thus 20 different values). The measurements for each magnetic field were done in random order and for every time, magnetic field and state we did three independent measurements.

In total, this were more than 7 000 experimental cycles, taken in two large runs. The first run took about 18 hours and covered the whole magnetic field area from 0 to 600 Gauss in 20 Gauss steps. The second run covered the region of the narrow loss feature around 130 Gauss with 7 Gauss per step. After these measurements

the data was split and separately analyzed for each spin state. These files were then sorted with a small Matlab script according to magnetic field values and time (using the bubble sort algorithm). Then the three independent measurements were averaged (arithmetic mean value) and finally further processed by the code developed in Innsbruck.

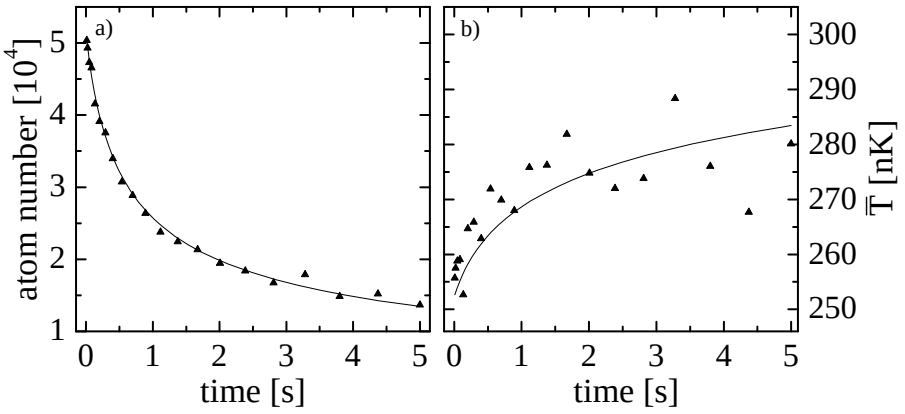

Figure 6.6: Atom number (a) and temperature (b) of state $|2\rangle$ as a function of time at a magnetic field of 300 Gauss. $\bar{T}$ is the effective temperature of the sample obtained by a Gaussian fit to the cloud after a time of flight. Every data point is the arithmetic mean value of three independent measurements. The solid line is the fit obtained with the method described in the text (see section 6.2.1). The resulting K_3 for those parameters is $1.93 \times 10^{-23}\ \frac{cm^6}{s}$.

The data obtained for the atom number and temperature was fitted with the model described in section 6.2.1. In figure 6.6 one can see the decay and heating curve for state $|2\rangle$ at 300 Gauss. The obtained K_3 is in this case $1.93 \times 10^{-23}\ \frac{cm^6}{s}$.

All those experiments were performed with a sample consisting of 50 000 atoms per state at a temperature of 215 nK and a peak density of 6×10^{11} atoms/cm^3. With trapping frequencies of $\omega_x = \omega_y = 2\pi \times 386(15)$ Hz and $\omega_z = 2\pi \times 38(2)$ Hz this corresponds to $T/T_F \approx 0.37$ (analyzed as explained in section 5.5). Hence, the sample is slightly degenerate, which means that the density distribution of the atoms in the trap is modified. Fortunately, the changes that occur due to the slight degeneracy are only weak. In order to counteract these minor changes, we fit a Gaussian distribution to the density after the time-of-flight and thus obtain an effective temperature $\bar{T}$ (see figure 6.6). For a degenerate sample $\bar{T}$ is slightly higher than the real temperature T (about 15%), this overestimation compensates to some extent the small effects of degeneracy. The reason for this is that the density in the degenerate sample is reduced by the Fermi pressure. Therefore, the real density of the sample is better approximated by a thermal sample with a higher effective temperature. During the loss process the number of atoms diminishes and

the temperature of the sample increases. Hence the temperature quickly exceeds the Fermi temperature. As a result, only the very first points are measured in a degenerate sample. For a thermal sample ($T/T_F \gtrsim 0.5$) the effective temperature is equal to the real one: $\bar{T} = T$. Thus it is a reasonable approximation to use $\bar{T}$ instead of T for the analysis.

From the fits to our data we obtain the three-body loss coefficient K_3 for all three states and various magnetic fields (see figure 6.7). The behavior of K_3 shows a shape expected from the low-field region measurements in section 6.1.1, with two loss maxima (a narrow and significantly wider one) at 130 and around 500 Gauss respectively, slowly rising slope between the two maxima and more stable regions for small fields and around 550 Gauss. The values of K_3 vary strongly as a function of the magnetic field almost three orders of magnitude separate the regions of small loss ($\leq$50 Gauss and around 550 Gauss) and the maximal loss near 130 Gauss (max. $K_3 \sim 9 \times 10^{-23}\ \frac{cm^6}{s}$).

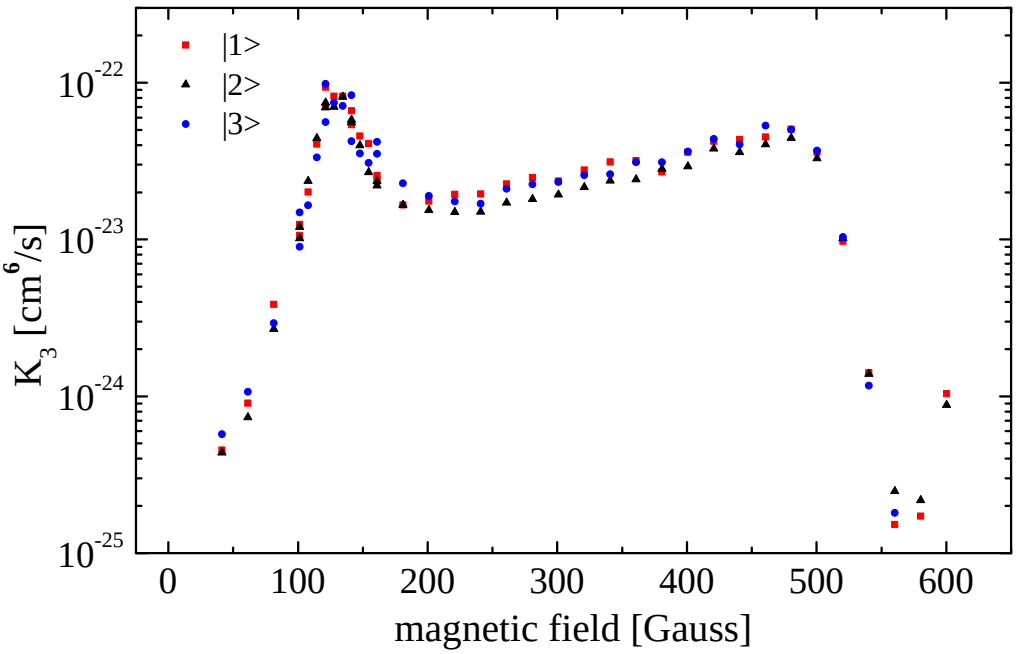

Figure 6.7: Three-body loss coefficient K_3 as a function of the magnetic field for the different spin states. The values are obtained by fitting experimental data as shown in figure 6.6 with the numerical routine explained earlier. The loss coefficient varies of nearly three order of magnitude. At about 130 Gauss a distinct loss maximum can be observed.

The relative error of the three-body loss coefficient can be estimated by the magnitude of the scatter of K_3 for the different Zeeman states. It is significantly

smaller than the observed variation of K_3 and caused by processes like fitting uncertainties, shot-to-shot number fluctuations, uncertainties in the spin balance and fluctuations of the imaging apparatus. Additionally, there is an error affecting the absolute scale of the measured three-body loss coefficient. K_3 scales proportional to $\propto N^2\,\bar{\omega}^6$, thus uncertainties in the absolute number of atoms of about 40% and an error of about 7% in the mean trap frequency lead in total to an uncertainty of about a factor of 2 in the absolute scale.

When we published these results [Ott08], we did not entirely understand most of the observed behavior. The more stable regions could be explained by the fact that there at least two scattering lengths were small. As explained earlier in section 6.1.1 this effectively results in a two-component Fermi gas and an independent component that is only weakly interacting. Thus the sample is stable. The reason for the two loss maxima and the slope in-between was at that time not yet understood. The observed three-body loss did not show in any way the expected a^4 behavior, which was predicted and observed in [Fed96, Esr96] and [Bur97, Ste99] for bosonic samples.

6.2.3 Temperature Dependence of the Three-Body Loss

In order to examine if the observed behavior showed a temperature dependence, we repeated the measurements with warmer samples. For 7 μK we measured the decay of the cloud for different magnetic fields and extracted K_3. The observed behavior of the three-body loss as a function of the magnetic field does not change at all compared to the sample with 215 nK sample (see figure 6.8). But the "warm" data lie a factor of about 5.6 below the 215 nK values. One reason for this could be that the error of the trapping frequency for higher temperature is larger than for the cold sample. For such high temperatures the power in the dipole trap beam is monitored and controlled by a different photo diode [Koh08]. To obtain the values needed anyway, we had to calibrate the two photodiodes with respect to each other and then we extrapolated the trapping frequency behavior. The result is a mean trapping frequency of $\bar{\omega} = 5770\,\mathrm{Hz}$, but the uncertainty for this value is large and difficult to determine. For an exact accordance between warm and cold data, the mean trapping frequency should be different by about 35 per cent. This is a reasonable uncertainty if one considers the unprecise assumptions made to obtain the trapping frequencies at 7 μK. Another possibility to explain the discrepancy could be that the degeneracy slighty alters the three-body loss.

In conclusion, we observed that the relative behavior of K_3 as a function of the magnetic field does not change even though the temperature is higher by a factor of 30. Temperature effects should first of all change the overall shape of the three-body loss [D'I04], they "wash-out" and shift resonances. Therefore, it seems that in the examined magnetic field region, temperature effects do not affect our three-

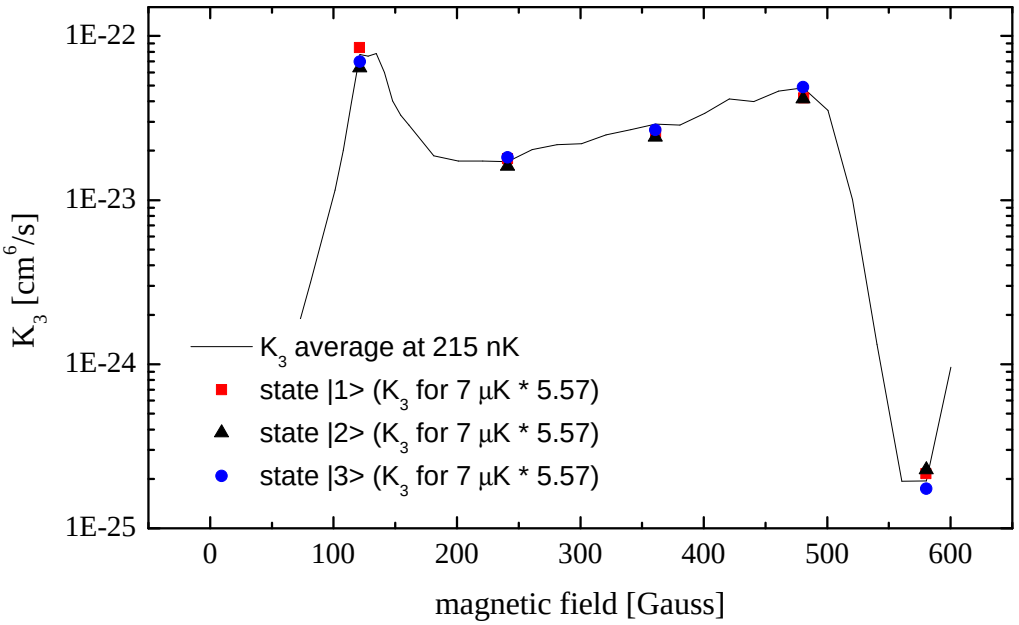

Figure 6.8: Three-body loss coefficient K_3 as a function of the magnetic field for the different spin states and temperatures. The solid black line is the arithmetic mean value of K_3 for the 215 nK sample (see figure 6.7). The squares, triangles and dots are the values obtained for a 7 μK sample. For a better comparison those values were multiplied by 5.57 to directly coincide with the cold data. One sees that the behavior of K_3 as a function of the magnetic field is identical although the temperature is different by more than a factor of 30. The offset between both temperatures is explainable by the large error for the trapping frequency for the 7 μK sample.

body loss process for temperatures below 7 μK.

The absolute scale changes within our uncertainties (which are quite large, due to the $\propto \bar{\omega}^6$ dependency of K_3) and we can therefore not make any precise predictions for that.

6.3 Theoretical Interpretation of Our Data

Here we will examine how we can relate the experimental data of the three-body loss (section 6.2) with the universal three-body theory developed in chapter 3.

6.3.1 Effective Scattering Length in a Three-Component Fermi Gas

Most of the theoretical predictions and considerations (see chapter 3) we have discussed so far, were developed for identical bosons. Since three non-identical fermions show some similarities to the case of identical bosons (e.g. no Pauli blocking for three-body processes involving all states) we wanted to use those predictions for our experiements (also because three-body recombinations in fermionic samples have only been theoretically studied for the one or two-component case e.g. [Sun03]). However, one fundamental difference from the bosonic case is that we are working with three dinstinguishable fermions. As a result, the interactions in our system are governed by three different s-wave scattering lengths (a_{12}, a_{13} and a_{23}). Hence the fermionic three-body interactions are not limited to the symmetric case, where three particles interact with the same coupling strength. This fact enables us to access a novel physical system, which was so far not experimentally available. However, the same fact also makes the theoretical treatment more elaborate. Therefore, it is of great help to introduce an effective "mean scattering" length a_m. This mean scattering length should combine all three different interactions in such a way that it resembles the systems key properties at least for the magnetic field of interest.

Since in our system all three states are part of a nuclear spin triplet, the possible two-body s-wave scattering lengths have some similarities (see figure 6.9). All of them are negative for small fields, they all cross zero around 530 Gauss and at roughly 300 Gauss they all exhibit a local minimum.

We noted earlier (see for example figure 6.3) that three-body processes still occur when one scattering length is small and the other two are large. Therefore, the effective interaction strength should resemble this. The cross section for a two-body collision of distinguishable fermions in the low-energy limit is given by

$$\sigma = 4\,\pi\,a^2. \tag{6.10}$$

If one now considers a three-body collision, mediated by two subsequent two-body collisions as shown in figure 6.3, an adequate way to combine scattering lengths would be proportional to $\propto a_{ij}^2\,a_{jk}^2$, where j is the mediating species. Now, one only needs to sum over all possible combinations and obtains:

$$a_m^4 = a_{12}^2\,a_{13}^2 + a_{12}^2\,a_{23}^2 + a_{13}^2\,a_{23}^2, \tag{6.11}$$

$$a_m = \sqrt[4]{a_{12}^2\,a_{13}^2 + a_{12}^2\,a_{23}^2 + a_{13}^2\,a_{23}^2}. \tag{6.12}$$

In some cases it will also be useful to define:

$$a_{m,1/3} = \sqrt[4]{\frac{1}{3}\,(a_{12}^2\,a_{13}^2 + a_{12}^2\,a_{23}^2 + a_{13}^2\,a_{23}^2)}. \tag{6.13}$$

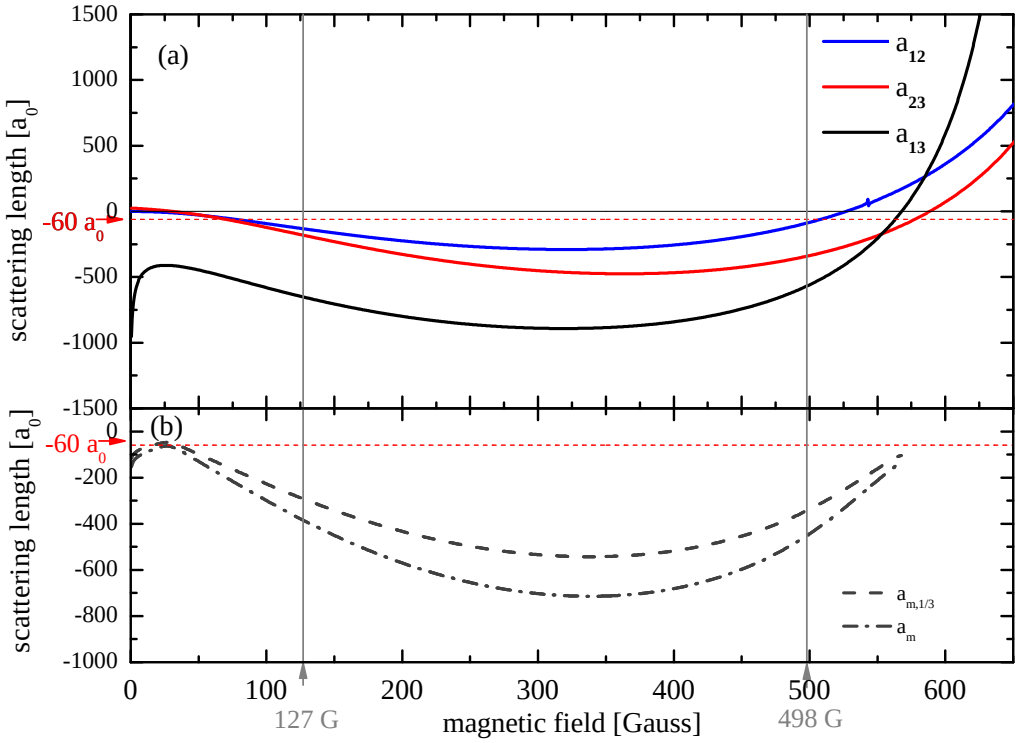

Figure 6.9: (a) All two-body s-wave scattering lengths as a function of the magnetic field. (b) shows the obtained effective scattering length in the region of interest with and without the 1/3 factor (see equation 6.12 and 6.13). For the later analysis the van der Waals length $l_{vdW} \approx 60a_0$ and the positions of the recombination maxima (at 127 and 498 Gauss) are also plotted. One sees that $|a_m| \lesssim l_{vdW}$ below 50 Gauss and at about 550 Gauss, in between the mean scattering length is negative and exhibits a local minimum at about 300 Gauss.

However, the numerical factor is on the order of one and the later analysis will only depend on the relative change of a_m, consequently this factor is not essential. Figure 6.9 shows the values of a_m and $a_{m,1/3}$ obtained for the low-field region. The van der Waals length and the maxima of the three-body loss are also plotted to facilitate later comparisons. With this effective interaction strength we are able to compare our data with the theory developed for bosons. One can see in figure 6.9 that the effective scattering lengths are, at the position of the two loss maxima, significantly larger than the van der Waals length (more than a factor of 5). In the Lithium case, this short range length scale is $l_{vdW} = 62.5\, a_0$. This implies that the system behaves (at least from about 100 to 500 Gauss) universal and thus one can neglect all effects stemming from the short range characteristics of the interaction potential. Thus we can make use of the theory developed for such

universal systems (e.g. [Bra06] or chapter 3).

6.3.2 Limits of Three-Body Recombination and Thermal Effects

In the theoretical considerations (see section 3.3.3), it was mentioned that the three-body recombination can be affected by temperature effects and limitations due to unitarity. Thus we will now examine how these processes affect our experiments. The original relations for these limitations were derived in [D'I04] for a bosonic sample and we adapted their model to describe femionic systems.

Unitary limitation

The values we obtained for the three-body loss coefficient K_3 are several orders of magnitude larger than the values measured for bosonic samples [Web03b, Bur97]. Therefore, one has to check if K_3 is already limited by unitarity. This limit is the maximum value for a given temperature. It is reached if all three-body collisions lead to three-body recombination and hence no elastic three-body collisions occur.
The limit can be easily obtained from the formula given in [D'I04]:

$$\bar{K}_3 = \sum_{J,\pi} \sum_{i,f} \frac{32\, N!\, (2J+1)\pi^2\, \hbar}{\mu\, k^4} \left| S_{f,i}^{J\,\pi} \right|^2 . \tag{6.14}$$

Here, due to a different definition of the three-body loss coefficient our $K_3 = \bar{K}_3/2$, J is the total orbital momentum involved, π the overall parity, μ is the three-body reduced mass ($\mu = m/\sqrt{3}$), $k = \sqrt{2\mu E/\hbar^2}$ is the wave number and i and f are the possible initial and final states, respectively. N is the number of identical particles participating in a three-body event, in our case N=1 (for identical bosons N this would be 3). In our experiments only s-wave interactions play a role, therefore we only take the $J = 0$ term into account. The initial state is given by three scattering atoms ("i = AAA") and the final state by all possible "high-energy" scattering states of a deeply bound dimers plus a free atom ("f = X").
The unitarity limit can be obtained from equation 6.14 by setting $|S_{X,AAA}|^2 = 1$, which means that every collision event leads to recombination. To account for the fact that one has a sample with fixed temperature and not with fixed energy in experiments, one additionally has to average $K_3(E)$ to obtain the thermal average $\langle K_3 \rangle (T)$. It turns out that this only introduces another factor of 1/2 for unitarity. Including all this, the maximal K_3 is given by

$$K_{3,max} = \frac{32\,\pi^2\,\hbar}{\mu\, k^4\, 4} = \frac{32\,\pi^2\,\hbar^5}{\mu^3 (k_B\, T)^2 16}. \tag{6.15}$$

If one plugs in the parameters of our experiment, the result is:

$$K_{3,max}(215\,nK) = 1.52 \times 10^{-19}\,\frac{cm^6}{s}. \tag{6.16}$$

This is several orders of magnitude larger than our experimentally determined values (our maximum $\approx 8 \times 10^{-23}\,cm^6/s$), hence our data are well below the unitary limit in the low-field region (below 600 Gauss) and for the cold sample. For the "warmer" sample ($T = 7\mu K$) one obtains $K_{3,max}(7\,\mu K) = 1.44 \times 10^{-22}\,cm^6/s$, which is about a factor of 10 larger than the measured values, hence we are still below the unitarity limitation.

As we did not measure K_3 for the regions of the Feshbach resonances, we are not able to conclude anything definitively for that region so far. But if one looks at the data of [Huc08], who determined K_3 also for values in the resonance region (their maximum value is about $1 \times 10^{-21}\,cm^6/s$), then their loss coefficient is on the same order of magnitude than the unitary limit for their temperature $K_{3,max}(1.9\mu K) = 1.95 \times 10^{-20}\,cm^6/s$.

Thermal effects

To check whether thermal effects affect the obtained results, D'Incao and coworkers [D'I04] introduced a critical scattering length, defined by

$$a_c = \frac{\hbar}{\sqrt{m\,k_B\,T}}. \tag{6.17}$$

For scattering lengths significantly smaller than this value, temperature effects, like washing out possible Efimov resonances, should not matter.

For $T = 7\,\mu K$ one obtains $a_c = 2030\,a_0$, which means that in the low-field region, where all scattering lengths are smaller than $900\,a_0$ temperature effects are negligable for our experimental parameters. This explains why the $215\,nK$ and $7\,\mu K$ data behave similarly as a function of the magnetic field, although the temperature is different by a factor of about 30.

From equation 6.17, one can calculate a temperature T_{therm} above which thermal effects come into play. This can be done by plugging in the maximum absolute value of the scattering length in the region of interest. From figure 6.9, we see that $a_{m,max} \approx -800\,a_0$, hence T_{therm} is about $45\,\mu K$.

For the high-field region the case is different. There, we measured loss from a thermal sample with a temperature of $1.2\,\mu K$, thus $a_c(1.2\,\mu K) = 4900\,a_0$. This means only for $a \ll a_c$ temperature effects should not occur. If one looks at the scattering lengths in that region (see figure 6.5) one observes, that above ≈ 950 Gauss thermal effect should not significantly alter the results.

If we examine again the experiments performed in [Huc08], we see that $a_c(1.9\,\mu K) = 3895\,a_0$. Hence, for all data at high magnetic fields (600-1000 Gauss) $|a| > a_c$ and thus thermal effects can not be neglected.

In conclusion, we can state that for all our measurements we are not limited by unitarity. Additionally, we calculated that in the low-field region thermal effects only play a role for temperatures $\gtrsim 45\,\mu K$. This explains why we did not see any change in the shape of K_3 in the low-field region for temperatures up to $7\,\mu K$ (see section 6.2.3). In the high-field region, thermal effects should not be important for magnetic fields above 950 Gauss, but they cannot be neglected in the region below that value. This shows that if one wants to examine the region of strong interaction, one has to use a extremely cold sample to enshure that thermal effects do not affect the measurements.

6.3.3 Theoretical Prediction for the Three-Body Loss Coefficient

In the present section, we will show how we can relate the experimental data of three-body loss with theory. Since we will apply the theory developed for the case of bosonic samples, we will use the effective mean scattering length a_m that was introduced above (for the sake of simplicity we will omit the index m and refer to the mean scattering length as a from now on).

We will first focus on the low-field region where we determined K_3. For our analysis we use formulas derived in chapter 3 and [Bra06]. This theory is based on the universal behavior of systems with large scattering lengths.

Low-field region

Several years ago, it was shown that in the low-energy limit the three-body recombination rate and thus the three-body loss coefficient into a deeply bound dimer should scale with the scattering length to the fourth power [Esr96, Nie99]:

$$K_3 = C(a)\,\frac{\hbar\,a^4}{m}, \tag{6.18}$$

where C is a factor, which depends on the scattering length. It was also stated by [Esr96] that $C(a)$ has resonances, wherever a three-body bound state crosses the three-atom continuum. Additionally, it was predicted that those resonances should show a log-periodic dependence on the scattering length (see [Bra06] or section 3.3).

During the first analysis of our experiments, we were puzzled that our data of the three-body loss coefficient did not resemble the expected a^4 dependency. To clarify the behavior of the three-body loss, it is helpful to divide K_3 by a numerical

constant $\times a^4$. The result is proportional to $C(a)$ as defined above and can be seen in figure 6.10. From this data it is then clearly visible that $C(a)$ shows two distinct peaks, a narrow one at 127 Gauss and a broader one at about 500 Gauss.

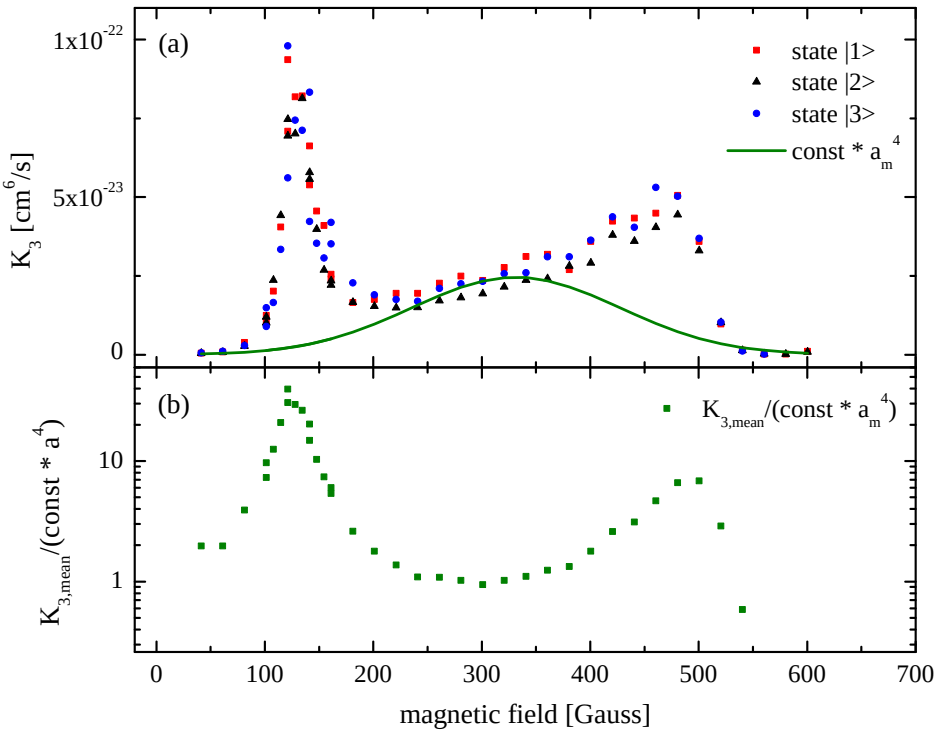

Figure 6.10: Figure (a) shows the values of the three-body loss coefficient K_3 together with a numerical constant $\times\, a_m^4$. In (b) the arithmetical mean of K_3 is divided by this factor, the result is $C(a)$ (defined in the text). Here, the two peaks are more pronounced and hence easier to observe. The peak maxima are located at 127 Gauss and around 500 Gauss.

The observed positions of the peaks are located in a region where $a_m > 5\, l_{vdW}$, hence the physics should be universal and only depend on the scattering length. In fact, we noticed in chapter 3 that to describe the three-body observables of a universal system, one actually needs an additional three-body parameter (e.g. κ_*). If inelastic processes occur this three-body parameter can be complex. The imaginary part is called inelasticity parameter η_* and can be connected to the width of the respective three-body resonances.

If one examines the scattering lengths at the resonance positions, one notices that the resonances occur at about the same value of a_m (roughly $-400\, a_0$). Additionally in this magnetic field region $a \gg l_{vdW}$, thus universality is applicable. These two facts are strong evidences that we indeed observe one Efimov-like three-body

bound state that crosses the continuum at two different fields. As explained earlier, this three-body bound state opens an additional loss channel into a deeply bound dimer state plus a free atom at the interaction strength, where the trimer state reaches the zero-energy continuum. This leads to a resonantly enhanced three-body loss rate, commonly referred to as Efimov resonance.

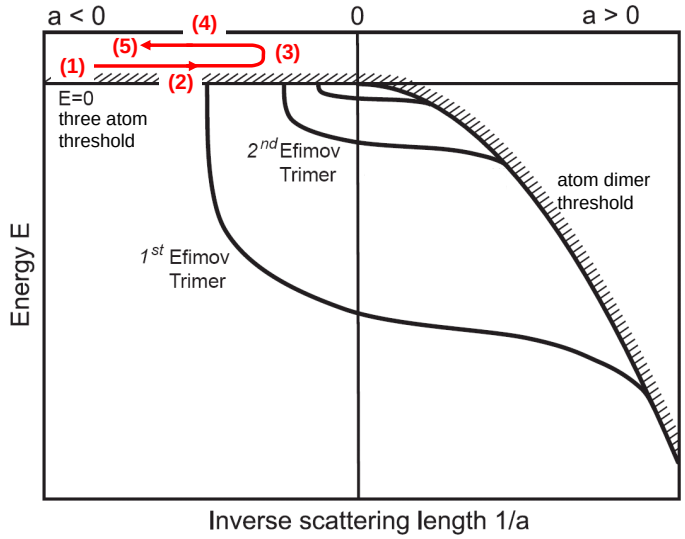

Figure 6.11: Efimov's scenario near a Feshbach resonance. Shown are several Efimov trimers that connect the three-atom continuum with the atom dimer threshold. The red line shows what happens in our case if the magnetic field is increased from 0 to about 600 Gauss. At a certain interaction strength (2), the hyperspherical potential supports a three-body bound state. If the magnetic field is further increased, the trimer state becomes deeper bound. At about 300 Gauss the magnitude of the scattering length starts to diminish again (3), thus the trimer binding energy is reduced until the trimer state hits the continuum (4). Figure adapted from [Kra06a].

However, in our case, the scenario is different from the one that is suggested around a Feshbach resonance, where Efimov predicted an infinite number of three-body bound states for diverging scattering length. In our system below 50 Gauss the scattering length is $\lesssim l_{vdW}$ ((1) in figure 6.11) but if one increases the magnetic field, the interactions become larger and one enters the universal regime. At a certain interaction strength the attraction between three atoms is strong enough to form a three-body bound state (corresponds to (2) in figure 6.11 and happens at a field of 127 Gauss). If the magnetic field is then further increased, the trimer binding energy grows as long as the magnitude of the scattering length increases. Above about 300 Gauss (3), the absolute of the scattering length starts to diminish

again, thus the trimer binding energy also decreases until the interactions become so weak that the trimer state reaches the continuum ((4) corresponds to a magnetic field of about 500 Gauss). At about 550 Gauss (5), the scattering length is once again on the order of the short range length scale (l_{vdW}).

Since all the assumptions made for the derivation of the three-body loss into deeply bound dimers in chapter 3 seem to be satisfied, we can try to fit the experimental data with the formula given in equation 3.32. This equation describes three-body recombination into deeply bound states for a universal system with $a < 0$ in the low-energy limit:

$$K_{3,deep} = \frac{c \sinh(2\,\eta_*)}{\sin^2[s_0 \ln(a/a_*)] + \sinh^2 \eta_*} \frac{\hbar\, a^4}{m}, \tag{6.19}$$

here $s_0 = 1.00624$ is the scaling parameter and c is a numerical constant. η_* is the inelasticity parameter earlier mentioned and a_* is one possible choice for the three-body parameter. This three-body parameter "fixes" the position of the Efimov reconances and those resonances occur for $a = a_* \left(e^{\pi/s_0}\right)^n$ (see section 3.3.3).

The overall amplitude of the three-body loss coefficient can, in principle, be calculated (e.g. using effective field theory). In fact, [Bra08] is able to determine c in our system. Their value is about a factor of 5 lower than our data, but taking into account the large uncertainty for the absolute scale in our measurements, this is still a reasonable agreement. Their model is based on the Skorniakov-Ter-Martirosian equations and takes all three different scattering lengths into account[1]. Therefore, it is significantly more complicated and elaborate than the model we are using here. Thus we use c as a free fitting parameter in the following analysis.

The fit and the data can be seen in figure 6.12. To obtain the fit (solid line), we used the formula 6.19, with three free parameters (c, η_* and a_*). The values were chosen such that $K_{3,deep}$ fits the narrow loss resonance around 127 G. For the scattering length we use the mean effective scattering length defined in equation 6.12 and from this fit we obtain: $c = 1871, \eta_* = 0.08$ and $a_* = -384\, a_0$. One sees that the region around the lower loss feature can be well explained using this relatively simple model, but for magnetic fields higher than about 250 Gauss the model does not describe the data very well. There are several explanations for this discrepancy. First we utilize a simplified model, which uses the mean scattering length. This could partcicularly lead to problems in the region where some of the different scattering lengths that enter a_m are smaller or comparable to l_{vdW} (happens for example for fields $\gtrsim 500$ Gauss). Here, the universal behavior breaks down and it is not easy to predict which consequences this has for three-body recombination. In the region where the sample is relatively stable (below about 100 Gauss), the

[1] In the next section we will discuss their approach and results in more detail.

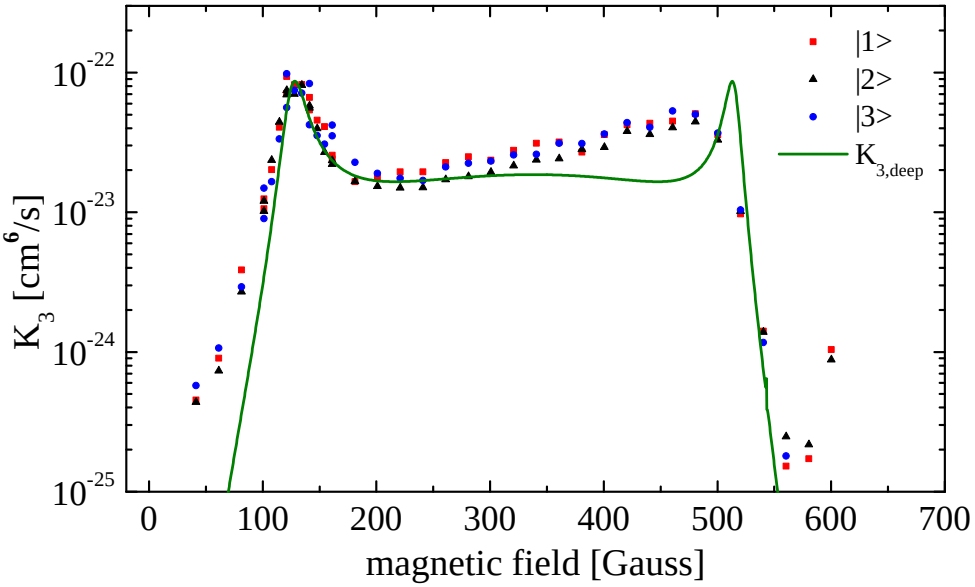

Figure 6.12: Experimental data of the three-body loss coefficient as a function of the magnetic field. The solid line is a three parameter fit using $K_{3,deep}$ from equation 6.19, which was optimized to fit the data at the narrow loss resonance. The accordance to the lower peak is clearly visible, but the broader peak at around 500 Gauss and the linear slope between the maxima are not well discribed by this prediction.

measured K_3 is significantly above the theoretical prediction. A reason for that could be that our model neglects the very small two-body losses. They would only matter where the three-body recombination rate is small and their disregard would lead to an overestimation of K_3. Another explanation could be that we used constants do describe the width η_* and the three-body parameter. In principle, these values are smooth functions of the magnetic field (see [Bra04, Bra01]). In these publications, E. Braaten and coworkers state that these functions can be approximated by constants near a sufficiently narrow Feshbach resonance. In our case, the resonances are rather broad (e.g. width for the 834 Gauss resonance in the $|1\rangle|2\rangle$ channel is about 300 Gauss (from [Bar05])) and 130 Gauss is still about twice the width away from the resonance.

Therefore, we fitted the upper half of the magnetic field region independently (see dashed line in figure 6.13) and found that the behavior of K_3 above 250 Gauss is described best with $\eta_* = 0.15$. Hence, to account for the observed change in η_* as a function of the magnetic field, we linearly extrapolated between the two independently obtained values ($\eta_* = 0.08$ at 127 Gauss and $\eta_* = 0.15$ at 498 Gauss). The result is $K_{3,deep,\eta(B)}$ and can be seen in figure 6.13 as the solid line.

The improvement compared to the simpler model with a constant η_* is clearly visible. Up to 400 Gauss this model describes well the measured behavior. The region of the broader peak is however still not perfectly characterized, it looks as if the change in the inelasticity parameter is still not adequate.

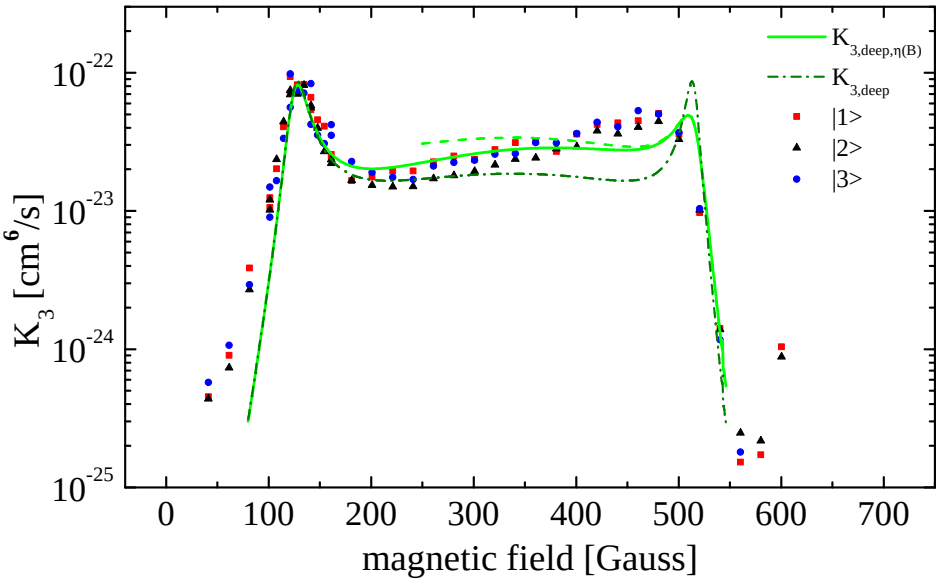

Figure 6.13: Fit for K_3, with η_* depending linearly on the magnetic field (called $K_{3,deep,\eta(B)}$, solid line). This enhanced model improves the accordance of model and data especially for the linear slope between the loss maxima (dash-dotted line shows the model for constant η_*). The dashed line shows the fit to the magnetic field region above 250 Gauss with an inelasticity parameter η_* of 0.15. The upper resonance is still not resembled perfectly. The parameters c and a_* were not changed with respect to the previous fit in figure 6.12.

In the ^{6}Li system, the scattering length can be negative far on the BEC side of the Feshbach resonances. The reason for this is the large and negative triplet background scattering length. Thus although we are in a regime where no shallow bound state occurs, we know the deeply bound states, which are nearest to the continuum, namely the states that are responsible for the respective Feshbach resonances: the molecular states with $S = 0$, $F = 0$, $m_F = 0$ and $S = 0$, $F = 2$, $m_F = 2, 1, 0$ (see section 2.1.3). They all tune roughly with two Bohr magnetons compared to the continuum, thus we can make a crude estimation of their binding energies:

$$E_B = 2\,\mu_B(B - B_0), \tag{6.20}$$

where μ_B is Bohr's magneton and B_0 the magnetic field of the Feshbach resonance. This approximation holds only far from the Feshbach resonances, where

the molecular states tune nearly linear with the field compared to the continuum. Near the respective resonance, the binding energy of the then only weakly bound (shallow) dimer is $\propto \frac{\hbar^2}{m\,a^2}$. In the magnetic field region we examined, the binding energy varies substantially. For example the $S = 0$, $F = 2$, $m_F = 0$ bound state, which is responsible for the narrow 543 Gauss Fesbach resonance in the $|1\rangle|2\rangle$ channel, has a binding energy of about $h \times 120\,\mathrm{MHz}$ at 500 Gauss and at 127 Gauss the binding energy is already about $h \times 1164\,\mathrm{MHz}$. Thus it is obvious that the inelasticity parameter η_* should change significantly in this magnetic field region.

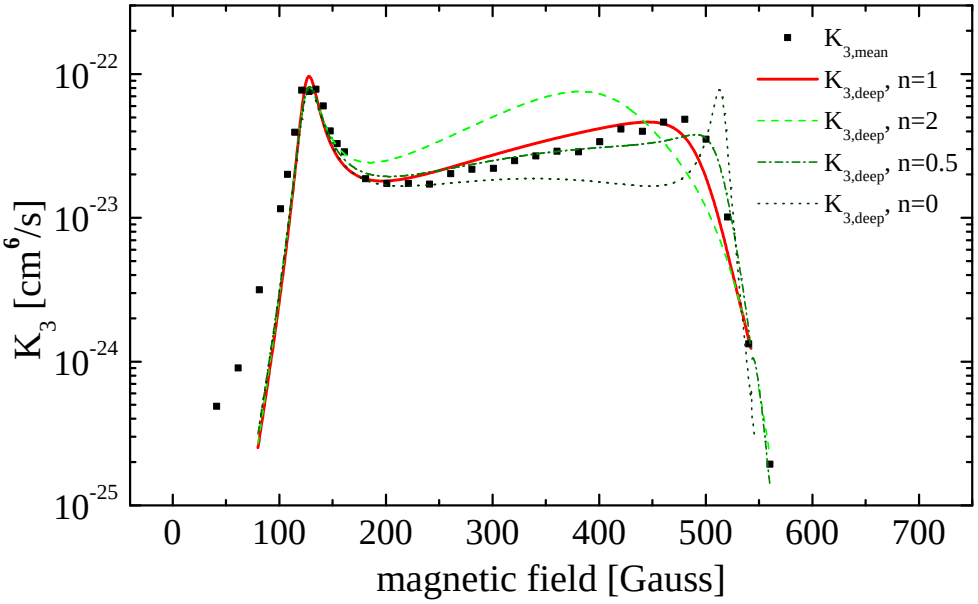

Figure 6.14: The squares show the arithmetic mean value of the experimental data for K_3. The lines are the fits to that data using different dependecies of η_* with the dimer binding energy (described in the text). The solid line is a fit for $\eta_* \propto 1/E_B$ and best resembles the behavior of the measured values.

As η_* is a measure for the width of the respective three-body bound state it should, at least approximately, scale proportional to $\propto 1/\left(E_B\right)^n$ (n beeing a constant > 0). This means the shallower the trimer is bound, the shorter its lifetime and thus the broader the observed resonance. It is so far by no means clear how η_* should scale exactly with the dimer binding energy or if there is a simple scaling law at all, but there are theoretical efforts under way to analytically calculate this dependency [Bra]. We tried different values for n (namely n= 0, 0.5, 1, 2) and the n=1 case described the data the best. We define

$$\eta_*(E_B) = A\,\frac{1}{\left(E_B\right)^n}, \tag{6.21}$$

with a numerical constant A, to fix the width of the narrow resonance (A is chosen such that $\eta_*(E_B) = 0.085$ at 127 Gauss and $B_0 = 543$ Gauss). The result of this model for n=1 can be seen in figure 6.14 as a red solid line. The other parameters (c and a_*) are the same as in the previous fits. This model describes the data impressively well. Especially the linear slope between the two loss resonances is very well resembled. There are still some small discrepencies, especially at around 500 Gauss, but they are most likely due to non-universal behavior and due to the asymmetry in the scattering lengths.

To sum up, we were able to reproduce the experimental data for the three-body loss coefficient with a model based on the universal description of recombination into a deeply bound dimer plus atom. For certain interaction strengths the three-body recombination rate is enhanced. It is most likely that an Efimov-like three-body bound state crosses the continuum for these values of the interaction. We observe two different magnetic fields, where such a resonant behavior occurs. The behavior of the interaction strength in that region suggests that the same trimer state is responsible for both observed resonances. Furthermore, the shape of these resonances differ significantly and a model in which the width of the Efimov state scales inversely proportional to the shallowest dimer state binding energy best resembles the experimental data. The agreement between our relatively simple model, which uses only a mean effective scattering length, and the data for the three-body loss coefficient is remarkable and suprising. This shows the strong impact of universality on three-body processes in ultracold gases.

High-field region

We have not been able to measure the three-body loss coefficient in the high-field region so far. The reasons for that are problems with the Feshbach coils and a recent upgrade of the experimental apparatus. The measurements can, in principle, be done relatively fast and are planned to be carried out in the near future. One important problem with those measurements will be to create a sufficiently cold sample since the interactions are stronger for the high-field region above all Feshbach resonances (> 843 Gauss) and thus thermal effects start playing a pivotal role at higher temperatures.

Nevertheless, we can draw some conclusions on possible three-body resonances due to Efimov trimers from the measurements where we recorded the remaining fraction after a certain time at different magnetic fields (see figure 6.5). In section 6.1.2, we stated that it seems like the observed loss could be explained only with the two-body scattering lengths. This is, as we showed in the theoretical considerations not true for universal three-body physics. To completely describe the system one three-body parameter (e.g. κ_*) is needed and additionally one needs an inelasticity parameter, which describes the width of the Efimov state. From K_3

data above all resonances one should be able to extract those parameters and thus one could predict the binding energies and possible zero-energy resonances of the trimers. However, we are not able to provide a quantitive analysis, because we did not measure K_3 in that region. Nevertheless, we can make some predictions on possible loss resonances in the magnetic field region above about 950 Gauss. Our data support the statement that in the region above 950 Gauss no loss resonance occurs. This region corresponds to a mean scattering length range from about $-5500\,a_0$ to about $-2500\,a_0$ (we cannot access weaker interactions with $a_m < 0$ than $\approx -2500\,a_0$ because of the large background scattering length in this region). Hence, either above or below this interaction strength a trimer state should cross the continuum. The large loss even for moderate scattering lengths near 1400 Gauss leads us to believe that there is a trimer state relatively near below the continuum, but as the scattering length saturates at a value of about $-2000\,a_0$ this state does never reach the continuum. It rather stays at a constant binding energy for fields above 1100 Gauss. This trimer state should in principle be significantly narrower than the states we analyzed in the low-field region. The reason for this is that above all resonances the bound dimer state closest to the three-atom continuum is extremely far away. Hence, the probability to enter this deeply bound dimer state in three-body recombination should be rather small. Consequently this would also lead to longer lifetimes of the possible Efimov trimer in that region, which could pave the way to interesting new physical phenomena due to a trimer state below the continuum and almost complete symmetric ($a_{12} \approx a_{13} \approx a_{23}$) interactions in all possible channels.

This analysis is, however, highly speculative and one should measure K_3 with a cold sample (order of 100 nK) in order to get more quantitative and definitive insights.

6.4 Theoretical Responses to Our Experiments

Soon after the publication of our work [Ott08] several theorists tried to analyze and explain our data [Bra08, Nai08, Sch08a] (all appeared within half a month). The groups used different theoretical approaches for their predictions but their results are all rather similar. All of them independently assumed that an Efimov-like trimer state reaches the three-atom continuum and this leads to the observed resonances in the three-body loss. We will now give a short overview on their methods and their results.

[Bra08] uses the Skorniakov-Ter-Martirosian equations and the optical theorem to directly obtain the three-body loss coefficient. This model takes into account all different scattering lengths and predicts a scaling of the interaction which is quite similar (up to numerical factors of the magnitude of one) to our mean scattering

length. For the region of the narrow loss resonance, they obtain that K_3 scales with $0.37\ (a\,a_{23})^4$, where $a_{12} = a_{13} = a$. For the intermediate region where all scattering lengths are large, they obtain a scaling similar to $a^4_{m,1/3}$ (as defined in equation 6.13). Only for the region of the broad resonance where $a_{12} < a_{23} < a_{13}$, there is no simple scaling law and a_m is therefore not a very good approximation. This fact could be the reason that our model does not perfectly describe the data there, even if η_* is varied as a function of the magnetic field.

Additionally, E. Braaten *et al.* also examined the high-field region. By using the data of [Huc08] (reaching up to 950 Gauss) to determine the three-body parameter and predict an additional Efimov resonance at around 1160 Gauss. This prediction could not be confirmed by our measurements in the high-field region. The reason for that could be the little amount of data available (only two data points) and changes due to temperature effects in the experimental data of [Huc08].

In [Nai08], P. Naidon *et al.* use the hyperspherical description to derive an equation for the hypersperical wavefunction, which is then solved numerically. As a result, the binding energy and width of the possible Efimov trimer could be calculated (see figure 6.15). They are also able to show that from universality and the behavior of the scattering lengths it follows that the trimer state that crosses the continuum at 127 Gauss reaches the continuum again at about 500 Gauss.

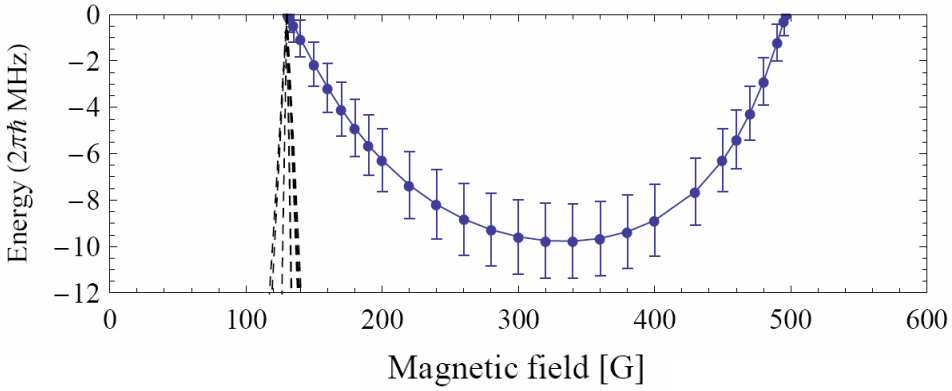

Figure 6.15: Binding energy of the Efimov trimer (solid line) as a function of the magnetic field. The vertical bars corresond to the width of the state. The dashed curves are estimates for the binding energies of trimers of other spin channels. Figure taken from [Nai08].

To calculate the three-body loss rate, [Nai08] determine the probability that three atoms are close together (hyperradius $R \approx 60\,a_0$), which is in general proportional to the recombination rate into the deeply bound dimer and free atom. Then this probability is rescaled and the imaginary part of the three-body parameter is fixed (corresponds to what we earlier called the inelasticity parameter η_* and de-

scribes the width and lifetime of the trimer state) such that the lower peak is well described by this theory. The result obtained looks similar to the result of [Bra08] and our model using a constant η_* (see figure 6.12). P. Naidon *et al.* explain the discrepancy near the broader resonance with non-universal behavior and a possible magnetic field dependence of the three-body parameter. From the binding energy and width of the Efimov trimer state they are able to infer that the lifetime of the trimer is about 50 ns at 300 Gauss. In addition, it could be calculated how non-Efimov trimers originating from other channels would scale with the magnetic field. The result is illustrated in figure 6.15 by dashed lines and shows that these states would tune monotonically with the magnetic field, which is not very probable if one looks at the behavior of the three-body loss.

The third paper dealing with our data is [Sch08a]. Here R. Schmidt *et al.* use a completely different approach to tackle the three-fermion problem. In a functional renormalization framework they use an average action that takes into account free fermiones (three types), all possible dimers (bosons), a fermionic trimer and all possible interactions between those. The three-body loss coefficient is estimated to be proportional to the square of the amplitude to form a trimer out of three fermions (with energy $\rightarrow 0$) times the trion propagator for small momenta. This enables them to fit our K_3 data using three different parameters: an overall offset, the location of one peak and the decay width, which was chosen to be a constant. The result looks again similar to what the other theories observed, the model fits well around the lower resonance but predicts a too narrow peak around 500 Gauss. Furthermore, the binding energy of the trimer can be estimated. The result looks similar to the binding energies obtained in [Nai08], both show a slower increase of the binding energy near the lower resonance and a steeper rise near 500 Gauss, a maximal binding energy of about 10 MHz and a maximal width of several MHz.

To sum up, three different groups were able to fit our data for the three-body loss coefficent, using totally different methods they all obtained similar results using a comparable set of parameters: one three-body parameter, which can be fixed through the lower sharper resonance, a constant parameter that describes the width and lifetime of the trimer state and a overall offset. E. Braaten et al. [Bra08] were able to explicitly calculate this offset and the value is of the same order of magnitude than our experimental data. The results of all groups showed deviations from the experimental data in the region of the upper resonance, which were explained with non-universal behavior and the approximation of a constant width parameter for the complete magnetic field region. Two of the groups could actually calculate the binding energy of the trimer state and their results are consistent, both show a binding energy of about 10 MHz at 300 Gauss.

Chapter 7

Conclusion and Outlook

The first realization of a balanced three-component Fermi gas, which is presented in this thesis, paves the way for studying a novel fermionic few- and many-body system. The present work describes how such a sample can be produced in the quantum degenerate regime with about 50 000 particles in each of the three Zeeman sublevels. This generic three-state system provides an excellent starting point for future experiments, which can be confirmed by the vast amount of theoretical work on the physics of such a three-component Fermi gas in the past few years.

For systems where the scattering lengths are significantly larger than the short range length scale (in our case given by the van-der-Waals length $l_{vdW} \approx 60\, a_0$), the physics should be universal. Thus the system should behave independently of the short range characteristics of the interaction potential. Hence the results obtained in such a system can be applied in principle to every fermionic system which also behaves universally, as e.g. strongly interacting neutrons, ^{3}He or partcles inside a ^{12}C nucleus. This universal behavior, together with the possible resonant interactions accessible through Feshbach resonances, makes our system especially interesting for other fields of physics. As the two-component Fermi gas can be used as a simpler system to study complex solid state phenomena, our three-component system, together with its SU(3) symmetry, could play the same role for high energy physics and help to understand how quarks group together [Wil07, Rap07].

Furthermore this thesis contains the first measurements on such a three-component Fermi gas. We were able to determine the three-body loss coefficient K_3 for different magnetic fields and hence as a function of the interaction strength (see also [Ott08]). The back then unexplainable structure of the three-body loss in the magnetic field region below 600 Gauss could be explained in this thesis with a model based on the universality of the system. The theory that was able to describe our data uses approaches developed in the 1960s and 1970s by L.D. Faddeev [Fad61] and V. N. Efimov [Efi71]. Their ideas were adapted and tailored to ultracold

bosonic systems by E. Braaten, H.W. Hammer, B. Esry, J.P. D'Incao, H. Suno, C. Greene, E. Nielsen, J. Macek and many others [Bra06, Esr96, D'I04, Nie99].

Concerning three-body loss, the three-component Fermi gas can be treated similarly to the case of identical bosons. However, in contrast to the bosonic case, the interactions between the three states are not equal. In principle, we have to deal with three different scattering lengths (a_{12}, a_{13} and a_{23}, where a_{ij} is the scattering length between state $|i\rangle$ and $|j\rangle$).

We were able to combine the three different scattering lengths to an effective interaction parameter. With this effective mean scattering length defined as

$$a_{m,1/3} = \left(\sum_{ijk} \frac{1}{3} a_{ij}^2 \, a_{jk}^2 \right)^{1/4}, \tag{7.1}$$

we could show that the formulas derived for the bosonic case could be applied with only minor changes. This significantly simplified the analysis of the three-body loss processes occuring in a three-component Fermi gas.

Consequently, we were able to explain the experimentally determined three-body loss coefficient with the function:

$$K_3 = C(a_{m,1/3}) \, \frac{\hbar \, a_{m,1/3}^4}{m}. \tag{7.2}$$

$C(a_{m.1/3})$ is a factor that depends on the scattering length and shows resonant enhancement for interactions where an Efimov-like three-body bound state [Efi71] crosses the continuum. This is commonly referred to as an Efimov resonance [Bra06]. Those resonances can in principle be thought of as the three-body analogy of a Feshbach resonance [Nai08].

The trimer states leading to the zero energy resonances are sometimes also referred to as "Borromean" states [Zhu93], named after the Italian aristocratic Borromeo family. Their coat of arms shows the three "Borromean rings" (see figure 7.1) which are linked in such way that if one removes one of the rings, the other two also disengage. In our case this means that the three states form a three-body bound state in a regime where the interatomic potential is too weak to form a two-body bound state. Hence if one removes one of the particles the other two will not remain bound in a dimer.

In our experiments, the observed three-body loss occurs due to three-body recombination. In this process, two of the three interacting particles form a bound state and the third particle carries away the excess momentum. The binding energy released in such a process is converted into kinetic energy of the dimer and the atom. If the dimer is deeply bound, the energy is more than sufficient to leave the relatively shallow dipole traps in our experiments. Accordingly this process leads to loss of atoms from the trap. At an Efimov resonance, the three-body

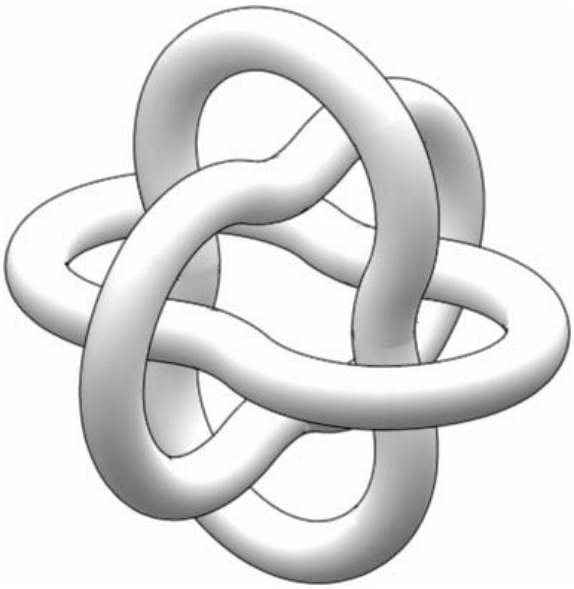

Figure 7.1: Borromean rings (figure from [Can06]).

bound state at the continuum opens an additional channel for three-body recombination, hence enhancing the loss resonantly. To fully describe this system one needs, in addition to the scattering lengths, a three-body parameter that fixes the position of such resonances. Normally, one uses the so-called Efimov parameter κ_*, which determines the binding energy of the trimer states for $a \to \pm\infty$. In the case of recombination into deep dimers one needs an additional inelasticity parameter (in [Bra06] called η_*, sometimes also referred to as the imaginary part of the three-body parameter [Nai08]), which effectively describes the loss into all possible deeply bound dimers and an additional atom. This loss mechanism gives a certain width to the zero-energy resonance and is connected to the lifetime of the trimer state.

In the magnetic field region below 600 Gauss we were able to observe two loss resonances and reference measurements with all possible two-component mixtures showed that those resonances are truly a three-state effect. The behavior of the scattering lengths in that region strongly suggests that the resonances are due to the same trimer state which crosses the continuum at about 127 Gauss and around 500 Gauss and has a binding energy of about 10 MHz at 300 Gauss (binding energy from [Nai08, Sch08a]). A schematic view the trimer binding energy can be seen in figure 7.2.

The width of the observed resonances differ significantly, this effect was so far not considered in previous theoretical work. Seeking a satisfactory explanation for this, we introduced a magnetic field dependence of the inelasticity parameter

η_*. This was motivated by the fact that in the region we were examining, the final states of the three-body recombination process (deeply bound dimers) change their binding energy by almost one order of magnitude. It is then comprehensible that the lifetime and therefore also the width of the corresponding trimer state should also undergo significant change. We proposed a scaling of $\eta_* \propto 1/(E_B)^n$, where E_B is the binding energy of the deeply bound dimer states. The resulting three-body loss coefficient obtained for $n = 1$ showed a surprisingly good accordance to the experimental data (see figure 6.14).

So far, these Efimov resonances have only been observed in ultracold bosonic ^{133}Cs [Kra06b] and predicted for three ^{4}He atoms [Gri00, Lee07]. Our system differs strongly from these systems and from the one Efimov initially thought of since it consists of fermionic atoms in three distinguishable states. Accordingly, these results provide conclusive evidence of the impressive impact of universality in systems with large scattering lengths.

After the publication of our preprint [Ott08], the behavior in the low-field region could be remeasured at Penn State University (group of K. O'Hara), at the University of Tokyo (group of M. Ueda) and at MIT (group of M. Zwierlein). Several months later, the group of K. O'Hara also published a preprint on this subject. It deals especially with the region of the two-body Feshbach resonances [Huc08].

The theoretical efforts made to explain our observed results [Bra08, Nai08, Sch08a] helped to elucidate the phenomena occuring in the low-field region ($\lesssim 600$ Gauss) and showed the great interest in this system.

In the high-field region ($\gtrsim 600$ Gauss), the case is, however, still not totally solved. Above all Feshbach resonances ("BCS" side of all resonances, with $a < 0$ for all possible channels) the data presented in this thesis could not verify the prediction by [Bra08] of another Efimov resonance near 1160 Gauss. The strong but smoothly varying three-body loss observed in this region suggests the existence of a trimer state right below the continuum. Owing to the large negative background scattering length of ^{6}Li, which is about $-2100\,a_0$, the trimer state could then never reach the continuum but rather tunes parallel to the zero-energy threshold. Additionally, in the region of the resonances in the $|1\rangle - |2\rangle$ and $|2\rangle - |3\rangle$ channel at about 830 Gauss, another trimer state could exist and that could then be an excited Efimov state. However, the occurence of such a state strongly depends on the three-body parameter in this region. The possible scenario for those states, together with the already observed resonances and the two-body scattering lengths, can be found in figure 7.2.

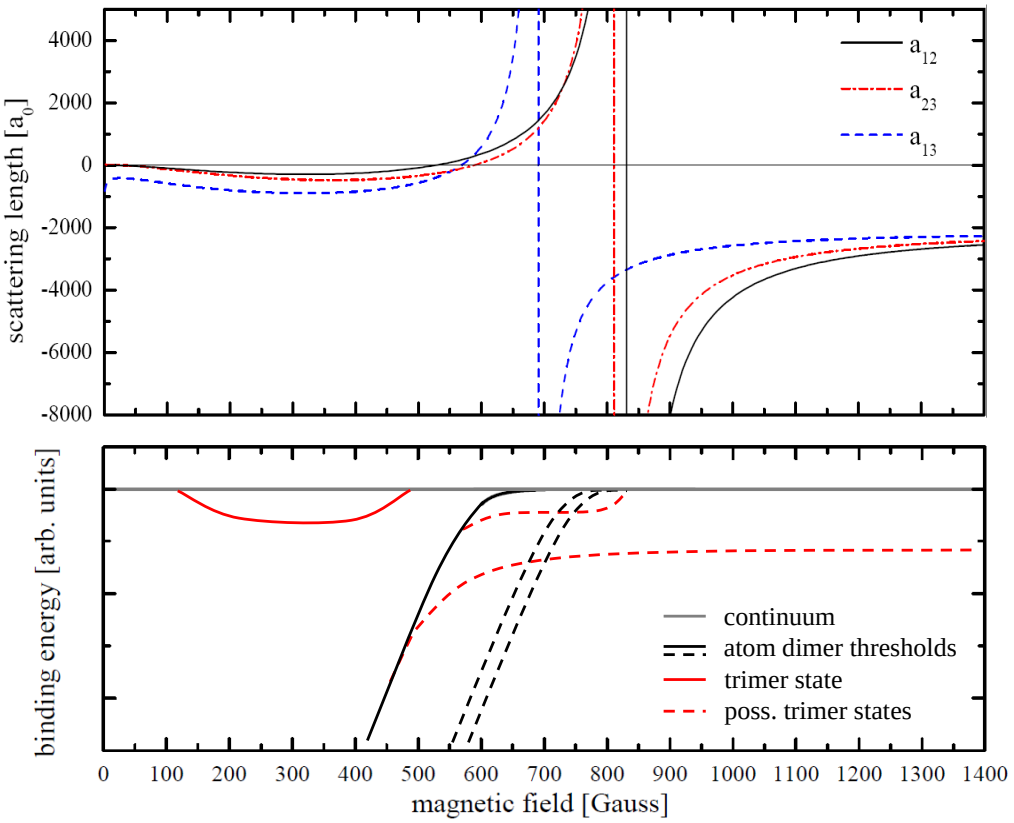

Figure 7.2: The possible scenario of trimer states for three-component ^{6}Li Fermi gases together with the scattering lengths. The black lines (dashed and solid) show the dimer plus free atom thresholds, the grey line shows the three free atom continuum. The solid red line is the trimer state, of which we most likely observed the zero-energy resonances. The red dashed lines show possible trimer states for the high-field region. It is by no means clear, what happens at the different atom-dimer thresholds.

7.1 Outlook

Three-component Fermi gases offer the possibility to study completely new physical phenomena and they enable to access a novel field of many-body physics. Additionally, there are still many open questions concerning the few-body physics and possible bound states of such a system. For example one could spectroscopically investigate the possible trimer states (in the low- and high-field region). Therefore, we have already experimented extensively with radio frequency (rf) and microwave (mw) spectrocopy. We applied multiple schemes seeking to associate trimer states with rf and mw photons, combinations of both and multiphoton

processes. We have not been able to resolve the trimer state so far. Possible explanations for this could be the relatively large width of the trimer state (several MHz around 300 Gauss) or unfavorable transition amplitudes. Another task on our short term agenda will be the measurement of the three-body loss coefficient in the region above all resonances (> 850 Gauss), from which the three-body parameters in that region could be deduced. Based on this information, one could calculate the binding energy of the trimers in that region. Additionally, the region between the Feshbach resonances also offers interesting physics. Since Efimov's original work deals with identical bosons, which have only one scattering length, there are no predictions for this region until today.

Other plans involve the study of the system's collective behavior and dynamics. The short lifetimes at strong interactions could be sufficient to examine how the third component affects the collective excitations in a strongly interacting gas and to study how unitary interactions influence the stability of such three-component Fermi gases. There are predictions that the three-component sample should collapse above a certain interaction strength, analog to a Bose-Einstein condensate with large attractive interactions [Blu08]. A recent theoretical work also discusses how a large inelasticity parameter η_* could enhance the lifetime of Efimov trimers [Wer08]. As η_* varies between the two peaks by a factor of about 2, it could be interesting what happens if η_* is further increased, e.g. by coupling the trimer state to a deeply bound molecular state. Particularly cold samples could allow to observe phase separation and shell structures, like for instance observed in the case of imbalanced two-component samples [Par06, Shi06]. Since the last experimental upgrade, we have an imaging apparatus capable of resolving such structures (see section 4.4.2). For this, however, one would need sufficiently low temperatures that fermionic superfluidity is established ($T/T_F \lesssim 0.2$). It remains questionable if this is achievable in three-component samples and if the lifetimes of such strongly interaction samples is sufficiently long to allow such a state to form.

To enhance the stability of this interesting system and to access rich, so far unexplored phase diagrams it would also be interesting to load the three-component sample into an optical lattice. One could then study phenomena related to a SU(3) Hubbard model. Additionally there are interesting predictions on exotic phases, like "color superfluids" [Rap07, Rap08] or strange BCS like systems [Aza08]. With an additional superlattice, there are schemes for the preparation of an extremely cold three-component sample, which could also assist the production of "color superfluid" phases [Dal08].

Appendix A

Fundamental constants

Symbol	Value	Meaning
$\hbar$	$1.054571628\times10^{-34}\,\mathrm{Js}$	Planck's constant over 2π
h	$6.62606896\times10^{-34}\,\mathrm{Js}$	Planck's constant
c	$2.99792458\times10^{8}\,\mathrm{m/s}$	Speed of light in vacuum
k_B	$1.3806504\times10^{-23}\,\mathrm{JK^{-1}}$	Boltzmann's constant
a_0	$0.52917720859\times10^{-10}\,\mathrm{m}$	Bohr's radius
ϵ_0	$8.854187817\times10^{-12}\,\mathrm{Fm^{-1}}$	Electric constant
μ_B	$927.400915\times10^{-26}\,\mathrm{J/T}$	Bohr's magneton
m_e	$9.10938215\times10^{-31}\,\mathrm{kg}$	Mass of a electron
m_{Li}	$9.98834146\times10^{-27}\,\mathrm{kg}$	Mass of a $^6\mathrm{Li}$ atom
Γ_{Li}	$36.898\times10^{6}\,\mathrm{s^{-1}}$	Natural linewidth of the D_2 line of $^6\mathrm{Li}$
λ_{Li}	$670.977338\times10^{-9}\,\mathrm{m}$	Wavelength of the D_2 line of $^6\mathrm{Li}$ in vacuum

Table 1: Constants used in this thesis. The fundamental constants are taken from [NIS], the properties of $^6\mathrm{Li}$ can be found in [Geh].

Bibliography

[And95] M. H. Anderson, J. R. Ensher, M. R. Matthews, C. E. Wieman, E. A. Cornell, *Observation of Bose-Einstein condensation in a Dilute Atomic Vapor*, Science **269**, 198–201 (Jul 1995).

[Aza08] P. Azaria, S. Capponi, P. Lecheminant, *Three-Component Fermi Gas in a one-dimensional Optical Lattice*, arXiv:cond-mat/arXiv:0811.0555 (2008).

[Bar57] J. Bardeen, L. N. Cooper, J. R. Schrieffer, *Microscopic Theory of Superconductivity*, Phys. Rev. **106**(1), 162–164 (Apr 1957).

[Bar04] M. Bartenstein, A. Altmeyer, S. Riedl, S. Jochim, C. Chin, J. H. Denschlag, R. Grimm, *Crossover from a molecular Bose-Einstein condensate to a Degenerate Fermi Gas*, Phys. Rev. Lett. **92**(12), 120401 (Mar 2004).

[Bar05] M. Bartenstein, A. Altmeyer, S. Riedl, R. Geursen, S. Jochim, C. Chin, J. H. Denschlag, R. Grimm, A. Simoni, E. Tiesinga, C. J. Williams, P. S. Julienne, *Precise Determination of ^{6}Li Cold Collision Parameters by Radio-Frequency Spectroscopy on Weakly Bound Molecules*, Phys. Rev. Lett. **94**(10), 103201 (2005).

[Bed06] P. F. Bedaque, J. P. D'Incao, *Superfluid phases of the three-species fermion gas*, arXiv:cond-mat/arXiv:0602525 (2006).

[Blu08] D. Blume, S. T. Rittenhouse, J. von Stecher, C. H. Greene, *Stability of inhomogeneous multicomponent Fermi gases*, Phys. Rev. A **77**(3), 033627 (2008).

[Bou04] T. Bourdel, L. Khaykovich, J. Cubizolles, J. Zhang, F. Chevy, M. Teichmann, L. Tarruell, S. J. J. M. F. Kokkelmans, C. Salomon, *Experimental Study of the BEC-BCS Crossover Region in Lithium 6*, Phys. Rev. Lett. **93**(5), 050401 (2004).

[Bra] E. Braaten, *Private Communications.*

[Bra01] E. Braaten, H.-W. Hammer, *Three-Body Recombination into Deep Bound States in a Bose Gas with Large Scattering Length*, Phys. Rev. Lett. **87**(16), 160407 (Oct 2001).

[Bra04] E. Braaten, H.-W. Hammer, *Enhanced dimer relaxation in an atomic and molecular Bose-Einstein condensate*, Phys. Rev. A **70**(4), 042706 (Oct 2004).

[Bra06] E. Braaten, H. W. Hammer, *Universality in Few-body Systems with Large Scattering Length*, Physics Reports **428**, 259 (2006).

[Bra08] E. Braaten, H.-W. Hammer, D. Kang, L. Platter, *Three-body Recombination of Fermionic Atoms with Large Scattering Lengths*, arXiv:cond-mat/arXiv:0811.3578v1 (2008).

[Bri04] F. Bringas, M. T. Yamashita, T. Frederico, *Triatomic continuum resonances for large negative scattering lengths*, Phys. Rev. A **69**(4), 040702 (2004).

[Bur97] E. A. Burt, R. W. Ghrist, C. J. Myatt, M. J. Holland, E. A. Cornell, C. E. Wieman, *Coherence, Correlations, and Collisions: What One Learns about Bose-Einstein Condensates from Their Decay*, Phys. Rev. Lett. **79**(3), 337–340 (Jul 1997).

[But97] D. A. Butts, D. S. Rokhsar, *Trapped Fermi gases*, Phys. Rev. A **55**(6), 4346–4350 (Jun 1997).

[Can06] J. Cantarella, J. H. G. Fu, R. Kusner, J. M. Sullivan, N. C. Wrinkle, *Criticality for the Gehring link problem*, Geometry & Topology **10**, 2055–2116 (2006).

[Car03] J. Carlson, S.-Y. Chang, V. R. Pandharipande, K. E. Schmidt, *Superfluid Fermi Gases with Large Scattering Length*, Phys. Rev. Lett. **91**(5), 050401 (Jul 2003).

[Che05] Q. Chen, J. Stajic, S. Tan, K. Levin, *BCS-BEC crossover: From high temperature superconductors to ultracold fluids*, Physics Reports **412**(1), 1–88 (Apr 2005).

[Che07] R. W. Cherng, G. Refael, E. Demler, *Superfluidity and Magnetism in Multicomponent Ultracold Fermions*, Phys. Rev. Lett. **99**(13), 130406 (2007).

[Chi04a] C. Chin, M. Bartenstein, A. Altmeyer, S. Riedl, S. Jochim, J. H. Denschlag, R. Grimm, *Observation of the Pairing Gap in a Strongly Interacting Fermi Gas*, Science **305**(5687), 1128–1130 (2004).

[Chi04b] C. Chin, R. Grimm, *Thermal equilibrium and efficient evaporation of an ultracold atom-molecule mixture*, Phys. Rev. A **69**(3), 033612 (Mar 2004).

[Dal85] J. Dalibard, C. Cohen-Tannoudji, *Dressed-atom approach to atomic motion in laser light: the dipole force revisited*, Journal of the Optical Society of America B **2**(11), 1707 (1985).

[Dal08] A. J. Daley, J. M. Taylor, S. Diehl, M. Baranov, P. Zoller, *Atomic three-body loss as a dynamical three-body interaction*, arXiv:cond-mat/arXiv:0810.5153v1 (2008).

[Dav95] K. B. Davis, M. O. Mewes, M. R. Andrews, N. J. van Druten, D. S. Durfee, D. M. Kurn, W. Ketterle, *Bose-Einstein condensation in a gas of sodium atoms*, Phys. Rev. Lett. **75**(22), 3969–3973 (Nov 1995).

[Del60] L. M. Delves, *Tertiary and general-order collisions (II)*, Nuclear Physics **20**, 275 – 308 (1960).

[D'I04] J. P. D'Incao, H. Suno, B. D. Esry, *Limits on Universality in Ultracold Three-Boson Recombination*, Phys. Rev. Lett. **93**(12), 123201 (Sep 2004).

[Efi70] V. Efimov, *Energy levels arising from resonant two-body forces in a three-body system*, Physics Letters B **33**(8), 563 – 564 (1970).

[Efi71] V. Efimov, *Weakly-bound states of three resonantly-interacting particles*, Sov. J. Nucl. Phys. **12**, 589–595 (1971), originally: Yad. Fiz. **12**, 1080-1091 (1970).

[Efi79] V. Efimov, *Low-energy properties of three resonantly interacting*, Sov. J. Nucl. Phys. **29**, 546–553 (1979), originally: Yad. Fiz. **29**, 1058-1069 (1979).

[Ein25] A. Einstein, *Quantentheorie des einatomigen idealen Gases. Zweite Abhandlung*, Sitzungsberichte der preussischen Akademie der Wissenschaften **1** (1925).

[Esr96] B. D. Esry, C. H. Greene, Y. Zhou, C. D. Lin, *Role of the scattering length in three-boson dynamics and Bose - Einstein condensation*, Journal of Physics B: Atomic, Molecular and Optical Physics **29**(2), L51–L57 (1996).

[Esr99] B. D. Esry, C. H. Greene, J. P. Burke, *Recombination of Three Atoms in the Ultracold Limit*, Phys. Rev. Lett. **83**(9), 1751–1754 (Aug 1999).

[Fad61] L. Faddeev, *Scattering Theory for a three-particle system*, Sov. Phys. JETP **12**(5), 1014 (May 1961).

[Fed96] P. O. Fedichev, M. W. Reynolds, G. V. Shlyapnikov, *Three-Body Recombination of Ultracold Atoms to a Weakly Bound s Level*, Phys. Rev. Lett. **77**(14), 2921–2924 (Sep 1996).

[Fes58] H. Feshbach, *A Unified Theory of Nuclear Reactions*, Ann. Phys. **5**(337) (1958).

[Flo08] S. Floerchinger, R. Schmidt, S. Moroz, C. Wetterich, *Functional renormalization for trion formation in ultracold fermion gases*, arXiv:cond-mat/arXiv:0809.1675 (2008).

[Geh] M. E. Gehm, *Properties of* ^{6}Lithium, *2003: http://www.phy.duke.edu/research/photon/qoptics/techdocs/pdf/PropertiesOfLi.pdf*.

[Gio08] S. Giorgini, L. P. Pitaevskii, S. Stringari, *Theory of ultracold atomic Fermi gases*, Reviews of Modern Physics **80**(4), 1215 (2008).

[Gnu] Gnu Special Library, *special functions: Fermi-Dirac Function. More information available at:*, http://www.gnu.org/software/gsl .

[Goa93] M. Goano, *Series expansion of the Fermi-Dirac integral over the entire domain of real j and x*, Solid-State Electronics **36**(2), 217 – 221 (1993).

[Goa95] M. Goano, *Algorithm 745: Computation of the Complete and Incomplete Fermi-Dirac Integral*, ACM Trans. Math. Softw. **21**(3), 221–232 (1995).

[Gra02] S. R. Granade, M. E. Gehm, K. M. O'Hara, J. E. Thomas, *All-Optical Production of a Degenerate Fermi Gas*, Phys. Rev. Lett. **88**(12), 120405 (Mar 2002).

[Gre03] M. Greiner, C. A. Regal, D. S. Jin, *Emergence of a molecular Bose-Einstein condensate from a Fermi gas*, Nature **426**, 537–540 (2003).

[Gri00] R. E. Grisenti, W. Schöllkopf, J. P. Toennies, G. C. Hegerfeldt, T. Köhler, M. Stoll, *Determination of the Bond Length and Binding Energy of the Helium Dimer by Diffraction from a Transmission Grating*, Phys. Rev. Lett. **85**(11), 2284–2287 (Sep 2000).

[Gri07] R. Grimm, *Ultracold Fermi gases in the BEC-BCS crossover: a review from the Innsbruck perspective* (2007).

[Gup03] S. Gupta, Z. Hadzibabic, M. W. Zwierlein, C. A. Stan, K. Dieckmann, C. H. Schunck, E. G. M. van Kempen, B. J. Verhaar, W. Ketterle, *Radio-Frequency Spectroscopy of Ultracold Fermions*, Science **300**(5626), 1723–1726 (2003).

[Hei01] H. Heiselberg, *Fermi systems with long scattering lengths*, Phys. Rev. A **63**(4), 043606 (Mar 2001).

[Hes86] H. F. Hess, *Evaporative cooling of magnetically trapped and compressed spin-polarized hydrogen*, Phys. Rev. B **34**(5), 3476–3479 (Sep 1986).

[Ho04] T.-L. Ho, *Universal Thermodynamics of Degenerate Quantum Gases in the Unitarity Limit*, Phys. Rev. Lett. **92**(9), 090402 (Mar 2004).

[Hon04] C. Honerkamp, W. Hofstetter, *BCS pairing in Fermi systems with N different hyperfine states*, Phys. Rev. B **70**(9), 094521 (Sep 2004).

[Huc08] J. H. Huckans, J. R. Williams, E. L. Hazlett, R. W. Stites, K. M. O'Hara, *Effect of resonant interactions on the stability of a three-state Fermi gas*, arXiv:physics/arXiv:0810.3288 (2008).

[Jen04] A. S. Jensen, K. Riisager, D. V. Fedorov, E. Garrido, *Structure and reactions of quantum halos*, Rev. Mod. Phys. **76**(1), 215–261 (Feb 2004).

[Joc03a] S. Jochim, M. Bartenstein, A. Altmeyer, G. Hendl, C. Chin, J. H. Denschlag, R. Grimm, *Pure Gas of Optically Trapped Molecules Created from Fermionic Atoms*, Phys. Rev. Lett. **91**(24), 240402 (Dec 2003).

[Joc03b] S. Jochim, M. Bartenstein, A. Altmeyer, G. Hendl, S. Riedl, C. Chin, J. Hecker Denschlag, R. Grimm, *Bose-Einstein condensation of molecules*, Science **302**(5653), 2101–2103 (2003).

[Joc04] S. Jochim, *Bose-Einstein Condensation of Molecules*, Dissertation, Universität Innsbruck (2004).

[Joc09] S. Jochim, *Ultracold Fermi gases: Properties and Techniques*, to be published (2009), in: M. Weidemueller, C. Zimmermann (Eds.), Cold Atoms and Molecules, WILEY-VCH.

[Jul] P. Julienne, *Private Communications, Calculations done according to [Bar05].*

[Jul92] P. Julienne, A. Smith, K. Burnett, *Theory of Collisions between Laser Cooled Atoms*, Vol. 30 of *Advances In Atomic, Molecular, and Optical Physics*, 141 – 198 (Academic Press, 1992).

[Ket08] W. Ketterle, M. W. Zwierlein, *Making, probing and understanding ultracold Fermi gases*, in: M. Inguscio, W.Ketterle, and C. Salomon (Eds.); Ultracold Fermi Gases, Proceedings of the International School of Physics - Enrico Fermi **Course CLXIV**, IOS Press (2008).

[Kno08] S. Knoop, F. Ferlaino, M. Mark, M. Berninger, H. Schoebel, H.-C. Naegerl, R. Grimm, *Observation of an Efimov-like resonance in ultracold atom-dimer scattering*, arXiv:cond-mat/arXiv:0807.3306 (2008).

[Koh08] M. Kohnen, *Ultracold Fermi Mixtures in an Optical Dipole Trap*, Diploma thesis (2008).

[Kra06a] T. Kraemer, *Few-Body Interactions in an Ultracold Gas of Cesium Atoms*, Dissertation, Universität Innsbruck (2006).

[Kra06b] T. Kraemer, M. Mark, P. Waldburger, J. G. Danzl, B. Chin, C.and Engeser, A. D. Lange, K. Pilch, A. Jaakkola, H.-C. Naegerl, R. Grimm, *Evidence for Efimov quantum states in an ultracold gas of caesium atoms*, Nature **440**, 315–318 (2006).

[Lan32] L. Landau, *Zur Theorie der Energieubertragung. II*, Phys. Z. Sowjetunion **2**, 46 (1932).

[Lan81] L. D. Landau, L. M. Lifshitz, *Quantum Mechanics* (Butterworth Heinemann, 1981), 3rd Edn.

[Lee07] M. D. Lee, T. Köhler, P. S. Julienne, *Excited Thomas-Efimov levels in ultracold gases*, Phys. Rev. A **76**(1), 012720 (2007).

[Lom08] T. Lompe, *An appartus for the production of molecular Bose-Einstein condensates*, Diploma thesis (2008).

[Luu07] T. Luu, A. Schwenk, *Three-Fermion Problems in Optical Lattices*, Phys. Rev. Lett. **98**(10), 103202 (2007).

[Mac05] J. H. Macek, S. Ovchinnikov, G. Gasaneo, *Solution for boson-diboson elastic scattering at zero energy in the shape-independent model*, Phys. Rev. A **72**(3), 032709 (Sep 2005).

[Met99] H. J. Metcalf, P. van der Straten, *Laser Cooling and Trapping* (Springer-Verlag, New York, 1999).

[Moe95] A. J. Moerdijk, B. J. Verhaar, A. Axelsson, *Resonances in ultracold collisions of $Li6$, $Li7$, and $Na23$*, Phys. Rev. A **51**(6), 4852–4861 (Jun 1995).

[Nai08] P. Naidon, M. Ueda, *A possible Efimov trimer state in 3-component lithium 6*, arXiv:physics/arXiv:0811.4086v1 (2008).

[NEG] NEG (non evaporable getter coating), *Information available at:*, http://est-div-sm.web.cern.ch/est-div-sm/Project-Getter-home.htm .

[Nie99] E. Nielsen, J. H. Macek, *Low-Energy Recombination of Identical Bosons by Three-Body Collisions*, Phys. Rev. Lett. **83**(8), 1566–1569 (Aug 1999).

[Nie01] E. Nielsen, D. V. Fedorov, A. S. Jensen, E. Garrido, *The three-body problem with short-range interactions*, Physics Reports **347**(5), 373 – 459 (2001).

[NIS] NIST, *http://physics.nist.gov/cuu/Constants/*.

[O'H99] K. M. O'Hara, S. R. Granade, M. E. Gehm, T. A. Savard, S. Bali, C. Freed, J. E. Thomas, *Ultrastable CO_2 Laser Trapping of Lithium Fermions*, Phys. Rev. Lett. **82**(21), 4204–4207 (May 1999).

[Ott08] T. B. Ottenstein, T. Lompe, M. Kohnen, A. N. Wenz, S. Jochim, *Collisional Stability of a Three-Component Degenerate Fermi Gas*, Phys. Rev. Lett. **101**(20), 203202 (2008).

[Paa06] T. Paananen, J.-P. Martikainen, P. Törmä, *Pairing in a three-component Fermi gas*, Phys. Rev. A **73**(5), 053606 (2006).

[Paa07] T. Paananen, P. Törmä, J.-P. Martikainen, *Coexistence and shell structures of several superfluids in trapped three-component Fermi mixtures*, Phys. Rev. A **75**(2), 023622 (2007).

[Par06] G. B. Partridge, W. Li, Y. A. Liao, R. G. Hulet, M. Haque, H. T. C. Stoof, *Deformation of a Trapped Fermi Gas with Unequal Spin Populations*, Phys. Rev. Lett. **97**(19), 190407 (2006).

[Pet02] C. J. Pethick, H. Smith, *Bose-Einstein-Condensation in Dilute Gases* (Cambridge University Press, 2002).

[Pet04] D. S. Petrov, C. Salomon, G. V. Shlyapnikov, *Weakly Bound Dimers of Fermionic Atoms*, Phys. Rev. Lett. **93**(9), 090404 (Aug 2004).

[Pet05] D. S. Petrov, C. Salomon, G. V. Shlyapnikov, *Scattering properties of weakly bound dimers of fermionic atoms*, Phys. Rev. A **71**(1), 012708 (2005).

[Pit03] L. Pitaevskii, S. Stringari, *Bose-Einstein Condensation* (Oxford Science Publications, 2003).

[Rap07] Ákos Rapp, G. Zaránd, C. Honerkamp, W. Hofstetter, *Color Superfluidity and "Baryon" Formation in Ultracold Fermions*, Phys. Rev. Lett. **98**(16), 160405 (2007).

[Rap08] A. Rapp, W. Hofstetter, G. Zaránd, *Trionic phase of ultracold fermions in an optical lattice: A variational study*, Phys. Rev. B **77**(14), 144520 (2008).

[Reg04] C. A. Regal, M. Greiner, D. S. Jin, *Observation of Resonance Condensation of Fermionic Atom Pairs*, Phys. Rev. Lett. **92**(4), 040403 (Jan 2004).

[Reg05] C. A. Regal, *Experimental realization of BCS-BEC crossover physics with a Fermi gas of atoms*, Ph.D. thesis, University of Colorado, Boulder (2005).

[rfs] rfsim99; program to impedance match RF circuits, *Available for example at:*, http://www.101science.com/RFSim99.exe .

[Rho50] P. Rhodes, *Fermi-Dirac functions of integral order*, Proc. R. Soc. **204**, 396–405 (1950).

[Sch94] W. Schollkopf, J. P. Toennies, *Nondestructive Mass Selection of Small van der Waals Clusters*, Science **266**(5189), 1345–1348 (1994).

[Sch99] U. Schunemann, H. Engler, R. Grimm, M. Weidemuller, M. Zielonkowski, *Simple scheme for tunable frequency offset locking of two lasers*, Review of Scientific Instruments **70**(1), 242–243 (1999).

[Sch05] C. H. Schunck, M. W. Zwierlein, C. A. Stan, S. M. F. Raupach, W. Ketterle, A. Simoni, E. Tiesinga, C. J. Williams, P. S. Julienne, *Feshbach resonances in fermionic ^6Li*, Phys. Rev. A **71**(4), 045601 (2005).

[Sch08a] R. Schmidt, S. Floerchinger, C. Wetterich, *Three-body loss in lithium from functional renormalization*, arXiv:cond-mat/arXiv:0812.1191v1 (2008).

[Sch08b] C. H. Schunck, Y.-i. Shin, A. Schirotzek, W. Ketterle, *Determination of the fermion pair size in a resonantly interacting superfluid*, Nature **454**, 739–743 (2008).

[Ser07] F. Serwane, *The setup of a Magneto Optical Trap for the preparation of a mesoscopic degenerate Fermi gas*, Diploma thesis (2007).

[Shi06] Y. Shin, M. W. Zwierlein, C. H. Schunck, A. Schirotzek, W. Ketterle, *Observation of Phase Separation in a Strongly Interacting Imbalanced Fermi Gas*, Phys. Rev. Lett. **97**(3), 030401 (2006).

[Ste99] J. Stenger, S. Inouye, M. R. Andrews, H.-J. Miesner, D. M. Stamper-Kurn, W. Ketterle, *Strongly Enhanced Inelastic Collisions in a Bose-Einstein condensate near Feshbach Resonances*, Phys. Rev. Lett. **82**(12), 2422–2425 (Mar 1999).

[Sun03] H. Suno, B. D. Esry, C. H. Greene, *Recombination of Three Ultracold Fermionic Atoms*, Phys. Rev. Lett. **90**(5), 053202 (Feb 2003).

[Tho35] L. H. Thomas, *The Interaction Between a Neutron and a Proton and the Structure of $H3$*, Phys. Rev. **47**(12), 903–909 (Jun 1935).

[Web03a] T. Weber, *Bose-Einstein Condensation of Optically Trapped Cesium*, Dissertation, Universität Innsbruck (2003).

[Web03b] T. Weber, J. Herbig, M. Mark, H.-C. Nägerl, R. Grimm, *Three-Body Recombination at Large Scattering Lengths in an Ultracold Atomic Gas*, Phys. Rev. Lett. **91**(12), 123201 (Sep 2003).

[Wer08] F. Werner, *Slowly decaying states of three particles with resonant interactions*, arXiv:0811.3290 (2008).

[Wil07] F. Wilczek, *Quantum chromodynamics: Lifestyles of the small and simple*, Nature Physics **3**, 375–376 (2007).

[Zen32] C. Zener, *Non-adiabatic Crossing of Energy Levels*, Proc. Roy. Soc. London, Series A **137**, 692–702 (1932).

[Zha07] H. Zhai, *Superfluidity in three-species mixtures of Fermi gases across Feshbach resonances*, Phys. Rev. A **75**(3), 031603 (2007).

[Zhu93] M. V. Zhukov, B. V. Danilin, D. V. Fedorov, J. M. Bang, I. J. Thompson, J. S. Vaagen, *Bound state properties of Borromean halo nuclei: 6He and 11Li*, Physics Reports **231**(4), 151 – 199 (1993).

[Zue09] G. Zuern, *Realization of an optical microtrap for the production of a finite Fermi gas*, Diploma thesis (to appear 2009).

[Zwi03a] M. W. Zwierlein, Z. Hadzibabic, S. Gupta, W. Ketterle, *Spectroscopic Insensitivity to Cold Collisions in a Two-State Mixture of Fermions*, Phys. Rev. Lett. **91**(25), 250404 (Dec 2003).

[Zwi03b] M. W. Zwierlein, C. A. Stan, C. H. Schunck, S. M. F. Raupach, S. Gupta, Z. Hadzibabic, W. Ketterle, *Observation of Bose-Einstein Condensation of Molecules*, Phys. Rev. Lett. **91**(25), 250401 (Dec 2003).

[Zwi05] M. W. Zwierlein, J. R. Abo-Shaeer, A. Schirotze, C. H. Schunck, W. Ketterle, *Vortices and superfluidity in a strongly interacting Fermi gas*, Nature **435**, 1047–1051 (2005).

Danksagung

Ich möchte mich bei allen bedanken die diese Arbeit ermöglicht haben. Zu aller erst danke ich meinem Betreuer Juniorprofessor Selim Jochim. Seine fabelhaft Betreuung gemeinsam mit seinem Enthusiasmus und seiner unerschöpflichen Geduld machten die Zeit dieser Diplomarbeit spannend und aufregend. Gemeinsam mit dem Rest der Gruppe machte er das letzte Jahr unvergesslich und hatte immer ein offenes Ohr für meine Probleme und Fragen.
Außerdem möchte ich allen Mitgliedern der "ultrakalten" Gruppe am MPIK: Timo, Thomas, Gerhard, Matthias, Friedhelm und Selim danken für: die vielen gemeinsamen Arbeitsstunden, Motivation und Enthusiasmus, Diskussionen, Geduld und Nachsicht mit mir, Korrekturlesen, Eisessen wenn was besonderes geklappt hat, Eisessen auch wenn mal nichts geklappt hat, Tischfussballspielen, Pizza um 23 Uhr, Ritterspiele im Labor, Cocktails beim Selim auf dem Balkon, Grillen, borromäische Ringe aus Knicklichtern ...

Ebenfalls danke ich allen am Max-Planck Institut für Kernphysik, im Besonderen Prof. J. Ullrich und seiner Gruppe für die warme und inspirierende Atmosphäre. Außerdem danke ich R. Schmidt, S. Moroz und S. Flörchinger für die vielen ergiebigen Diskussionen und Gespräche.

Zusätzlich danke ich: Andi, Philipp, Falk und Stevo. Ohne euch hätte das Studium nicht halb so viel Spass gemacht. Der See vor 308 wartet auf uns.

Mein besonderer Dank gilt meiner Freundin Nele. Ohne deine Unterstützung, Hilfe und sprachliche Kenntnisse hätte ich das alles nie geschafft.

Zuletzt möchte ich meinen Eltern und meiner Schwester danken.
Ihr habt mir alles ermöglicht.